LIVE CELL IMAGING OF INORGANIC PHOSPHATE DISTRIBUTION IN MULTICELLULAR ORGANISMS USING A FRET BASED BIOSENSOR

A Dissertation

by

SWAYOMA BANERJEE

Submitted to the Office of Graduate and Professional Studies of
Texas A&M University
in partial fulfillment of the requirements for the degree of

DOCTOR OF PHILOSOPHY

Chair of Committee,	Wayne K. Versaw
Co-Chair of Committee,	L. Rene Garcia
Committee Members,	Thomas D. McKnight
	Dorothy Shippen
Head of Department,	Thomas D. McKnight

August 2017

Major Subject: Biology

ABSTRACT

Inorganic phosphate (Pi) has central roles in metabolism, cell signaling, and energy conversions that rely on the distribution of appropriate amounts of Pi to each cell and subcellular compartment. An analytical method for monitoring Pi dynamics with high spatial and temporal resolution is therefore required to gain a comprehensive understanding of the transport and metabolic recycling mechanisms that govern Pi homeostasis. In this work I optimized a genetically encoded Forster Resonance Energy Transfer (FRET)-based Pi biosensor to assess cellular and subcellular Pi concentrations. Using a model animal, *Caenorhabditis elegans*, I demonstrated that the Pi biosensor could resolve cell-specific and developmental stage-specific differences in cytosolic Pi accumulation. This study also established that cellular Pi concentration is a sensitive indicator of metabolic status. I further refined the methods of FRET-based Pi measurements for different subcellular compartments in the model plant *Arabidopsis thaliana.* Additionally, I used microinjection to develop an *in vivo* calibration for Pi-dependent FRET responses that enabled direct quantification of Pi within the cytosol. Using this method, I identified an unexpected developmental zone-specific Pi concentration pattern in the root, with highest accumulation in the transition zone. This study revealed that the Pi distribution pattern is robust, independent of external Pi, and is modulated by intracellular activities. Finally, I used FRET-based Pi measurements to establish that the chloroplast Pi transporter PHT2;1 imports Pi into the chloroplast and thereby modulates stromal Pi concentrations.

DEDICATION

To Aniket and to all the plants in this world.

ACKNOWLEDGEMENTS

I would like to thank my advisor Dr. Wayne Versaw for giving me the opportunity to work in his laboratory. I thank him for mentoring and supporting me throughout my graduate career. I would also like to thank my co-advisor Dr. Rene Garcia for his support, guidance and invaluable contribution to my dissertation. Both Dr. Versaw and Dr. Garcia have immense contribution towards my development as a researcher. Additionally, I thank my committee members Dr. Thomas McKnight and Dr. Dorothy Shippen for their insight, guidance and encouragement.

I would like to thank the members of Dr. Versaw's lab; Dr. Sonia Irigoyen and Dr. Pallavi Mukherjee for training me in laboratory techniques. I am thankful to Sonia for being a friend, confidante and guide. Thanks to my colleagues Dr. Jing Shi and Ms. Abira Sahu for their help. I thank Dr. Xin Chen, Dr. Paola Correa and Dr. Brigitte LeBoeuf from Dr. Garcia's lab for teaching me techniques related to confocal microscopy and *C. elegans* imaging. Thanks to all members of Dr. McKnight's lab, Dr. Alan Pepper's lab and Dr. Terry Thomas's lab for their assistance.

I would like to extend my gratitude to our Graduate advisor Dr. Arne Lekven for being the caring individual that he is. I am thankful to him for his guidance and encouragement during difficult times. I am also thankful to Ms. Jennifer Bradford for all her help and for making graduate life a little easier.

Finally, thanks to my mom and dad for encouraging me to pursue my goals.

CONTRIBUTORS AND FUNDING SOURCES

Contributors

This work was supervised by a dissertation committee consisting of Dr. Wayne K. Versaw [advisor], Dr. L. Rene Garcia [co-advisor] and Dr. Thomas D. McKnight of the Department of Biology, and Dr. Dorothy Shippen of the Department of Biochemistry and Biophysics.

Dr. L. Rene Garcia performed the experiments for figures 1, 2, 3B, 4 and 5A described in Chapter 1.

All other work conducted for the dissertation was completed by the student independently.

Funding Sources

This work was supported by the Department of Energy (grant no. DE-SC0014037), and the Howard Hughes Medical Institute. Its contents are solely the responsibility of the authors and do not necessarily represent the official views of the Department of Energy and Howard Hughes Medical Institute.

TABLE OF CONTENTS

Page

LIST OF FIGURES

Page

LIST OF TABLES

Page

CHAPTER I

INTRODUCTION AND LITERATURE REVIEW

1.1 Phosphate (Pi) is essential for all living organisms

Inorganic phosphate (Pi) is a macronutrient present in all cells and cellular compartments. It is a constituent of key macromolecules such phospholipids and nucleic acids. Also, cellular energetics relies on Pi as a component of high-energy nucleoside triphosphates, *e.g*., ATP, GTP. Additionally, Pi plays a significant role in signal transduction processes that involve phosphorylation and dephosphorylation of participating proteins. Furthermore, Pi acts as a regulator of many enzymatic reactions and metabolic processes. Aside from its fundamental importance in cellular biochemistry, Pi serves specific roles in animal and plant metabolism.

The main motivation behind studying Pi metabolism in animals is revealing how to ameliorate Pi toxicity. In animal systems, the major role of Pi is in the development and maintenance of skeletal tissues. Animals maintain appropriate physiological concentrations of Pi by excreting excess amounts of dietary Pi. Ineffective excretion of Pi may result in Pi-toxicity [1,2]. For example, decreased kidney function leads to hyperphosphatemia, which triggers cardiovascular complications, vascular calcifications, chronic kidney diseases, and decalcification of bones [3-5]. Understanding mechanisms of Pi regulation in animal systems is therefore necessary for the development of therapeutics to counteract Pi-toxicity.

Unlike animal systems, studying Pi metabolism in plants is necessary to understand how plants acclimate to low Pi levels. In plants, a significant role of Pi is in modulating photosynthesis and carbon metabolism. Pi serves as the substrate for photophosphorylation during the light reaction of photosynthesis, and the resulting ATP fuels the Calvin cycle to generate photo-assimilated sugars. Furthermore, Pi acts as an effector molecule for regulating carbon partitioning [6] to meet the demands of source and sink tissues. Contrary to animal systems, where the main challenge is the prevention of Pi toxicity, plants struggle to maintain sufficient cellular and subcellular Pi concentrations to sustain proper growth and development. To make matters worse, bioavailable Pi is scarce in the soil and is poorly diffusible [7]. Therefore, understanding the mechanisms plants use to acquire and regulate this essential nutrient is crucial for engineering plants with greater Pi use efficiency.

1.2 Pi homeostasis in plants

1.2.1 Bioavailable Pi in the soil is scarce

Plants acquire phosphorus as inorganic orthophosphate from the soil and it constitutes about 0.2% of their total dry weight [7]. Although phosphorus is the 11th most abundant mineral in the lithosphere, bioavailable Pi in the soil exists in extremely low concentrations (1-10 μM) [8]. Pi interacts with soil particles to form complexes and precipitates that cannot be absorbed by plants. Up to 80% of phosphorus in the soil is fixed in organic forms (*e.g.* phytic acid) and insoluble inorganic compounds [9].

Additionally, Pi has an extremely low rate of diffusion (10^{-12} to 10^{-15} m^2s^{-1}) [7] through soil, resulting in heterogeneous Pi concentrations, and ultimately resulting in a zone of depletion around the roots [10]. Although the use of Pi-rich fertilizer remediates the low availability of Pi, this practice has limitations and detrimental effects. The cost of fertilizers can constitute up to 25% of total production cost. Moreover, with increasing global population the rock reserves of Pi are estimated to be exhausted in the next 50 to 100 years [11]. Pi-rich fertilizers can also lead to water pollution when excess Pi leaches into the aquatic ecosystems. Therefore, the motivation to improve crop yields while preserving our environment necessitates a thorough understanding of phosphate usage in plants.

1.2.2 Pi acquisition and utilization by plants

Plants have evolved mechanisms to acquire and utilize Pi efficiently. These mechanisms include Pi uptake by high-affinity Pi transporters, mobilization and compartmentalization of Pi within the plant, and multiple adaptations to counteract Pi deficiency (*e.g.* changes in root architecture, modifications of cellular metabolic pathways, and transcriptional regulation).

1.2.2.1 Pi uptake from soil by high affinity Pi transporters

A fundamental step in Pi acquisition is its transport across the plasma membrane. Pi concentration in plant tissue has been estimated to be around 5-20 mM [12], which is 1000 times greater than the bioavailable concentration in soil (2-10 μM). Therefore, Pi

anions ($H_2PO_4^-$ and HPO_4^{2-}) are transported across the plasma membrane against their concentration gradient. The driving force for Pi transport is the proton electrochemical gradient across the plasma membrane, which is generated by the P-type ATPase pump at the expense of ATP. Pi is transported with a proton (co-transport or also referred to as symport) by high-affinity transporters of the PHT1 family, which are expressed predominantly in root epidermal cells [13].

The PHT1 family consists of nine members (PHT1;1 to PHT1;9) in *Arabidopsis thaliana.* PHT1;1 and PHT1;4 were the first members of this family discovered and characterized [14-16]. Homologues of PHT1 genes have since been discovered in many other plant species, including potato, tomato, *Medicago sp*., wheat, maize, and barley. These transporters contain around 550 amino acids (~58 kDa), have 12 membrane-spanning domains, [12,17], and have Km values ranging from 2.5 to 100 μM [18,19]. *In situ* hybridization studies, along with GFP reporter analyses, revealed that PHT1 proteins are expressed primarily in roots and localize to the plasma membrane. Most of these transporters are concentrated in the epidermal cells, especially in the primary meristem, root cap, and root hairs. Some PHT1 proteins are also expressed in aerial tissues such as leaves and flowers [20,21]. Plants can upregulate PHT1 expression both transcriptionally and post-translationally in response to low Pi availability. Post translational regulation of PHT1 proteins by PHF1 (PHOSPHATE TRANSPORTER TRAFFIC FACILITATOR1) involves enhanced intracellular trafficking of PHT1 proteins to the plasma membrane [22]. Positive regulation of PHT1 transporters is one of the key Pi stress responses that facilitate Pi acquisition.

1.2.2.2 Pi mobilization between subcellular compartments by Pi transporters

After entering the cell, Pi is mobilized to subcellular compartments such as, plastids, mitochondria, and the vacuole, often in exchange for specific counter ions [23]. Since Pi is required for physiological and biochemical processes carried out in these organelles, it is critical to tightly regulate Pi concentrations within each of these cell compartments. Specific Pi transporters are responsible for transporting Pi across the organellar membranes. Biochemical and molecular studies have revealed multiple families of Pi transporters involved in Pi transport across cellular membranes, including the plasma membrane (PHT1), mitochondrial inner membrane (PHT3), plastid inner membrane and thylakoid membrane (PHT2, PHT4, pPT), and vacuolar membrane (PHT5) [24-27].

Mitochondria and chloroplasts are the major sites of energy transduction processes carried out within a plant cell. Mitochondria require Pi as the substrate for ATP synthesis *via* oxidative phosphorylation, and Pi is acquired from the cytosol by PHT3 transporters. The Arabidopsis PHT3 family consists of three transporters, PHT3;1, PHT3;2 and PHT3;3, each consisting of ~350 amino acids [24]. PHT3 genes share homology with the first characterized mitochondrial Pi transporter cloned from Birch, Mpt1 [28]. Mitochondrial Pi transporters have been characterized in several other plant species and they are predicted to facilitate Pi/H^+ symport or Pi/OH^- antiport across the mitochondrial membrane.

Chloroplasts require Pi to synthesize ATP *via* photophosphorylation during the light dependent reaction of photosynthesis. During Pi deprivation, stromal Pi levels can

become limiting for photosynthesis [29]. Therefore, Pi homeostasis is strictly controlled in the chloroplast to maintain a balance between photosynthesis and carbon partitioning. The chloroplast inner envelope membrane, which is the permeability barrier between the cytosol and stroma, contains multiple Pi transporters (*e.g.* TPT, PPT, XPT, PHT2;1 and PHT4;4) [30,31]. Detailed discussion of these transporters will be provided in later sections.

In mature plant tissues, vacuoles serve as the major reservoir of the 'non-metabolic pool' of cellular Pi storing about 85% to 95% of total Pi within the plant [8]. During Pi deprivation, vacuoles release the stored Pi to fuel biochemical processes in other parts of the cell [23]. Liu *et al*. [27] recently described the PHT5 family in Arabidopsis, PHT5;1, PHT5;2 and PHT5;3, which mediate Pi transport across the vacuolar membrane. PHT5;1 and PHT5;3 are ubiquitously expressed throughout the plant, and PHT5;2 is expressed mostly in guard cells, vascular tissue, and pollen [27]. GFP reporter studies confirmed the localization of these proteins to the vacuolar membrane (tonoplast). Additionally, ^{31}P-magnetic resonance spectroscopy revealed that loss of PHT5;1 function results in decreased vacuole:cytoplasmic Pi ratio, as well as decreased overall Pi accumulation in plants. Although the significance of Pi transporters in vacuolar Pi loading is apparent, the biochemical mechanism of Pi transport across the tonoplast is unknown.

1.2.2.3 Plant adaptations to cope with Pi deficiency

Plants have evolved a numerous mechanisms to sustain growth and development despite limited Pi availability. These include metabolic, transcriptional, post translational, and morphological adaptations. The following section describes some of the major adaptations for the acquisition and judicious use of Pi.

1.2.2.3.1 Cellular Pi recycling

In order to maintain cytosolic Pi levels, plants mobilize Pi from vacuolar reserves and recycle Pi from organophosphates. The vacuole is the principle Pi reserve within the cell. ^{31}P NMR studies have confirmed that under Pi starvation, vacuolar Pi is released to maintain cytosolic Pi levels [23,32]. However, after exhaustion of vacuolar reserves, cytosolic Pi levels decrease. Another mechanism that plants have evolved to counteract low cytosolic Pi is enzyme-mediated release of Pi from intracellular and extracellular organophosphates. Intracellular acid phosphatases and ribonucleases liberate Pi from sugar phosphates and nucleosides, and synthesis of these enzymes increase during Pi starvation [33-35]. Similarly, plants secrete acid phosphatases and phytase to hydrolyze extracellular organophosphate compounds. Plants also secrete organic acids (malate, citrate) to solubilize Pi from inorganic complexes, *e.g.,* aluminum phosphate, present in the soil [36-38]. Pi liberation from vacuoles and organic compounds is one of the earliest responses to Pi stress.

1.2.2.3.2 Metabolic changes

Plants alter several of their metabolic pathways when Pi is limiting to increase the efficiency of Pi utilization. For example, glycolytic enzymes that require Pi or ATP (hexose kinase, phosphofructokinase, glyceraldehyde 3-phosphate dehydrogenase, and phosphoglycerate kinase) are repressed, whereas bypass enzymes that recycle Pi (phosphoenolpyruvate phosphatase) are induced. [39,40]. Also, when Pi is limiting for ATP synthesis, the mitochondrial electron transport chain follows two non-phosphorylating pathways involving alternative oxidases [41]. Furthermore, Pi deprivation is associated with the decrease of cellular phospholipids such as phosphatidylcholine and phosphatidylglycerol, and a corresponding increase in sulfolipids and galactolipids [42,43]. Additionally, Pi starvation leads to increased starch synthesis, which liberates Pi that ultimately can be used in photosynthesis [41]. Besides mechanisms that regulate Pi usage at the cellular level, Pi stress also induces transcriptional responses that enhance systemic Pi redistribution.

1.2.2.3.3 Transcriptional regulation

Plants undergo transcriptional regulation as a Pi stress response to enhance Pi uptake and systemic Pi remobilization to source and sink tissues. Some of the key regulatory transcription factors and regulators are described below.

One of the key transcription factors induced by Pi stress is PHOSPHATE STARVATION RESPONSE 1 (PHR1), a Myb transcription factor. PHR1 binds to the DNA motif GNATATNC and enhances the expression of Pi stress response genes such

as *PHT1*, *PHO1*, and *miRNA399* [44]. miRNA399 plays a critical role in long distance Pi signaling by negatively regulating PHO2, which is a E2 ubiquitin conjugating protein. Under normal conditions, PHO2 is responsible for the degradation of PHO1, which aides Pi distribution from the root to aerial tissues via xylem. Under Pi stress, degradation of *PHO2* mRNA by *miRNA399* positively regulates *PHO1,* and hence enhances Pi mobilization from roots to source tissues [45,46]. Other Pi stress induced transcription factors include ZAT6 and WKRY75, which promote root architecture modifications to augment Pi acquisition [47].

Pi deficiency induces the expression of several proteins that regulate Pi uptake and distribution. *LOW PHOSPHATE ROOT* (*LPR*) encodes a copper oxidase enzyme and *PHOSPHATE DEFICIENCY RESPONSE 2* (*PDR2*) encodes a P5-type ATPase in the ER [48,49]. Both *LPR* and *PDR2* are expressed in the root meristematic zone and are involved in local Pi sensing around the roots, which ultimately modifies root architecture to augment Pi acquisition [50]. SPX domain-binding proteins, such as AtSPX1-AtSPX3 in Arabidopsis, control downstream Phosphate Starvation-Inducible (PSI) genes that in turn positively regulate *PHT1*, *PHO1* and *PHR1* genes [51,52].

1.2.2.3.4 Morphological changes in the root system

Low Pi stress leads to changes in root morphology and the association of roots with mycorrhizal fungi, which enhance Pi uptake. When a plant experiences Pi deficiency, it increases its root/shoot ratio along with decreased primary root growth and increased density of lateral roots and root hairs to generate shallower and bushier roots.

These morphological changes allow plants to explore a greater volume of soil. Similarly, the formation of symbiotic association with mycorrhizal fungi allows plant roots to access and acquire Pi beyond the normal zone of depletion [53]. In plants such as *Medicago*, rice, tomato, and potato, arbuscular mycorrhizal (AM) fungi colonize the cortical layer of the root and have hyphae that act as extensions of the plant's root system. Besides extending the limits of the root, AM fungi also modulate the composition and concentrations of certain growth hormones such as auxin, cytokinin, ethylene, and strigolactones, which in turn alter the root architecture and facilitate further fungal colonization. Furthermore, AM fungi induce the expression of high-affinity Pi transporters located in the periarbuscular membrane of colonized roots, which import Pi from the periarbuscular space [54-56]. The following section reviews the mechanisms involved in Pi stress-induced root structure architecture (RSA) modifications aimed at facilitating Pi acquisition from the soil.

1.3 Root development and the influence of Pi availability

The root is the first organ to acquire nutrients from the surrounding environment and distributes it to the rest of the aerial tissues. Root development and rooting depth are crucial for accessing mineral nutrients with poor diffusion such as Pi. Low external Pi acts as a signal that alters root development to generate maximum surface area contact at the root-soil interface. Studies have revealed that high affinity Pi transporters on the plasma membrane mediate Pi uptake into the root; however, the internal distribution of acquired Pi has not yet been clearly defined. One of the objectives of this dissertation is

to understand internal Pi compartmentalization within the root and its significance in overall root growth. In the following section, I review the stages of root development, and the effect of external Pi availability on root structure and growth.

1.3.1 Root developmental zones

Root development consists of four distinct stages, which consequently divides the root anatomy into four zones of growth. Starting from the root tip the four developmental zones are the meristematic zone (MZ), the transition zone (TZ), the elongation zone (EZ) and the differentiation zone (DZ). The DZ ultimately transforms into the mature root (MR). Each of the zones have unique cellular properties and they are maintained by diverse signaling processes [57,58]. The following section discusses the major cellular characteristics of the developmental zones of the root apex that are crucial for root growth.

The MZ consists of rapidly dividing cells of the apical meristem. Studies conducted with cell cycle markers, such as cyclins (CYCB1), revealed that the MZ extends 150 to 200 μm from the root cap junction (RCJ), and it is the only zone that contains mitotically active cells [59,60]. MZ cells are undifferentiated and are maintained in this state by non-autonomous signals from the stem cell niche (SCN) around the quiescent center (QC) [61]. The rate of cell division in the MZ and the rate of rapid cell elongation in the EZ are the two major factors that influence root growth. However, the MZ cells are not accurately equipped to undergo rapid elongation.

Therefore, post-mitotic cells from the apical meristem enter the TZ where they are transformed for rapid elongation in the EZ [62,63].

TZ cells show high similarity to mitotic cells at the interphase stage, and they go through DNA endoreplication without cytokinesis. TZ cells expand at an extremely slow rate in both axial and transverse directions thus developing an isodiametric shape [64,65]. The TZ cells have been described in literature as ‘plastic cells’, which have the capacity to turn into both rapidly dividing cells (distal part of the TZ) and rapidly elongating cells (proximal part of the TZ) depending on environmental challenges and necessity. Nevertheless, under the normal course of development TZ cells enter the rapid elongation phase. Therefore, the major cellular activities such as changes in vacuolar structure, reorganization of cytoskeleton, and loosening of cell wall, that occur in these cells are directed towards making the cells competent for elongation. The proximal cells of the TZ are marked by redistribution of cortical microtubules to transverse arrays, which is a prerequisite for polar cell expansion [66,67]. These cells also undergo processes that lead to the expansion of vacuoles, i.e., sucrose unloading in the cytosol from protophloem and expression of the tonoplast aquaporin γTIP [68,69]. Additionally, the cellulose-xyloglucan network of the cell wall of proximal TZ cells are modified by expansins and xyloglucan endotransglucosylase/hydrolase (XTH) enzymes. These activities increase the distance between cellulose microfibrils and promote turgor pressure driven expansion of cells [70,71]. Proximal TZ cells also display an elevated concentration and activity of the glycosylphosphatidylinositol (GPI) anchored protein

COBRA, which presumably interacts with cell wall molecules, establishes cell polarity, and aides in the transition of cells to rapid elongation [72].

The EZ extends from around 300-900 μm from the RCJ. Cells in this region increase in cell length 300% within three hours. The fucosylated arabinogalactan proteins constituting the walls of EZ cells play a crucial role in rapid elongation [73,74]. These cells manifest transverse arrays of cellulose fibrils that mirror the orientation of the microtubules occurring within rapidly elongating cells [75]. The limit of the rapid elongation zone is marked by the disruption of transverse arrays of cortical microtubules and the first appearance of root hairs in trichoblast cells. The cells at the end of the EZ also show myosin VIII accumulation and callose deposition in the cross walls, which leads to symplastic isolation of the EZ epidermal cells from the DZ [76,77].

Cells in the DZ and MR are completely differentiated and are mainly involved in nutrient acquisition *via* the epidermal cells, and in distribution through the vascular tissues. Additionally, DZ and MR cells are comparatively less sensitive to environmental stresses such as Pi deficiency.

1.3.2 Root architecture modifications during Pi deficiency

Low Pi stress influences root system architectural modifications, including rooting depth and the density of lateral roots and root hairs [78-81]. In Arabidopsis, these modifications lead to the development of a shallow root system with decreased primary root length and high density of lateral roots and root hairs [82,83]. The cellular

mechanisms involved in the root developmental zones that lead to RSA modifications are discussed as follows.

Under low Pi availability, the primary root length decreases mainly due to reduced cell division and cellular differentiation in the primary meristem and due to decreased cell expansion in the elongation zone. Kinetic studies with genetic markers of the QC and cell cycle revealed that Pi stress induces alterations in QC activity, which decreases the number of mitotic cells in the primary meristem [84,85]. Additionally, the elongation zone suffers a massive decrease in the number and length of cells [49,84]. Thus, Pi deficiency leads to shallower rooting in Arabidopsis plants enabling them to explore the top soil for maximum Pi acquisition; however, these plants are more susceptible to drought since the top soil dries out sooner [86].

Under low Pi stress, the primary root develops significantly more lateral roots to increase maximum surface areal contact with the soil [87]. Pi deficiency shifts the site of mitotic activity from the MZ of the primary root to the site of lateral root initiation, thus increasing the number of lateral roots. [88]. However, the rate of growth of the lateral roots is stunted under Pi deficiency in a manner similar to that of the primary roots. The length of lateral roots significantly shortens under low Pi conditions due to a dramatic decrease in cell differentiation in the meristem and expansion of cells in the EZ [85,89]. Nevertheless, each lateral root develops more lateral roots repeatedly thus giving rise to a complex bushy network of roots with large surface area.

Enhanced root hair production is another key mechanism that increases the area of the root soil interface. Root hairs develop from asymmetric division of epidermal cells

(trichoblasts) and follow three distinct phases of cell specification, initiation, and elongation [90,91]. Low Pi stress initiates an increase in the length and number of the trichoblast cells thus increasing the total number of root hairs [92,93]. Studies have also shown that Pi deficiency increases length of root hairs to enhance the overall effective radius of the root system, which is one of the earliest morphological responses to low Pi stress [94-96]. Moreover, root hairs have a high density of high affinity Pi transporters; therefore, increased surface area of root hair augments Pi acquisition from the soil.

1.3.3 Role of growth regulators in root development and in Pi stress responses

Growth regulators such as gibberellin, auxin, ethylene, and cytokinin control the key processes occurring in the root apex that lead to root growth, *i.e.* cell division, differentiation, and elongation. In addition, growth regulators play important roles in modulating root system architecture during Pi deficiency. Chapter IV of my work demonstrates the correlation amongst growth regulators, internal Pi distribution, and root growth. In this section, I summarize the roles of the major growth regulators in overall root development and in Pi stress adaptations.

1.3.3.1 Gibberellin

GA signaling promotes cell division and cell elongation in the root. Positive GA signaling by the degradation of nuclear DELLA proteins promotes cell proliferation in the MZ. DELLAs are transcriptional repressors of GA signaling that induce the expression of cyclin dependent kinase (CDK) inhibitors (KRP2, SIAMESE) [97].

Additionally, GAs synthesized in the primary meristem translocate to the EZ and promote cell elongation [98,99]

Pi starvation leads to negative GA signaling, triggering stunted root growth. Pi stress causes accumulation of DELLA proteins that decrease bioavailable GA and ultimately inhibit root growth. External application of GA circumvents root growth inhibition under Pi stress, which is also observed in DELLA mutants [100-102].

1.3.3.2. Auxin

Similar to GA, auxin induces cell division in the MZ. Cyclin and CDK genes expressed in MZ cells have auxin response elements (AREs) in their promoter region. Therefore, polar auxin transport to the MZ results in positive auxin signaling leading to meristematic cell division. Furthermore, auxin maintains the stem cell niche by CDK-mediated phosphorylation and negative regulation of RETINOBLASTOMA-RELATED protein (RBR) that inhibits G1 to S transition and leads to loss of stem cells in the MZ [103-105].

In low Pi conditions, auxin transporter mutants display reduced primary root growth and increased density of lateral roots, similar to wild-type plants [106]. However, external auxin application to Pi-deprived roots increases root hair length and density, which aides higher Pi acquisition [82].

1.3.3.3. Cytokinin

Cytokinins (CKs) induce cell proliferation in shoots and calli by cyclin D3 induction; nonetheless, they severely reduce the number of dividing cells in the MZ. However, instead of directly affecting the cell cycle, CKs promote early differentiation of the MZ cells to TZ and result in the overall reduction of dividing cells in the primary meristem [65,107,108]. Moreover, CKs induce the transition of MZ cells to endoreplication by the activation of anaphase promoting complex/cyclosome (APC/C) *via* an E3 ubiquitin ligase (CCS52A1) that degrades mitotic cyclins [109,110]. Auxin signaling, on the other hand, represses endoreplication. However, CKs produced in the MZ translocate to the TZ *via* the phloem [111] and induce SHY2 (inhibitor of auxin response) mediated antagonism of auxin signaling in the TZ [112], which promotes cell differentiation.

CKs are known to inhibit primary and lateral root growth, and to inhibit expression of Pi starvation inducible genes [113,114]. Nevertheless, low Pi levels in plants lead to reduced CK concentration and repression of the CK receptor CRE1 [115-117]. Therefore, the negative regulation of CK signaling induced by Pi stress ameliorates root growth inhibition.

1.3.3.4. Ethylene

Ethylene promotes mitotic division of QC cells during post embryonic development; yet, it has no dramatic effect on division and differentiation of primary meristem cells [104,118]. However, ethylene metabolism can influence root growth by

modulating cell expansion in the EZ-DZ. Ethylene promotes polar auxin transport from the root tip to the EZ-DZ; therefore, cell elongation is reduced as a consequence of high auxin concentration in the EZ-DZ. Additionally, ethylene prevents GA-induced cell growth in the EZ-DZ possibly by blocking GA translocation from MZ to EZ-DZ [99,119]

During Pi deficiency, ethylene inhibits primary root growth by affecting cell division at the QC [118]. Lopez-Bucio *et al*. have shown that ethylene mutants grown in Pi limiting conditions have significantly shorter primary roots [106]. Additionally, Pi deficiency leads to elevated ethylene production and increased ethylene sensitivity [120], which may ultimately result in reduced cell elongation in the EZ-DZ. Furthermore, ethylene increases root hair density in Pi deprived plants by decreasing the length of trichoblast cells [92], which is a classic Pi stress adaptation.

Although a plethora of research data corroborate the downstream effects of hormone signaling on root development under Pi deficiency, specific cellular mechanisms leading to phenotypic modifications remain elusive due to complex and synergistic cross talk. Understanding specific mechanisms of hormone signaling and regulation will enable plant breeders to achieve higher crop productivity without the secondary detrimental effects of continued hormone and fertilizer application.

1.4 Chloroplast phosphate homeostasis

Pi homeostasis in chloroplasts is critical for photosynthesis and carbon metabolism, and is therefore crucial for maximizing plant biomass. One of the objectives

of this dissertation is to understand how Pi balance is maintained in the chloroplast. In this section, I review the major biochemical activities occurring in the chloroplast and their correlation to Pi.

1.4.1 The categories of plastids

Plastids are unique organelles found only in plant cells. These double membrane bound organelles are the site of synthesis of key biomolecules such as carbohydrates, fatty acids, and amino acids, and are the storage sites for pigments, oils, and starch. Plastids can be broadly divided into two classes, photosynthetic and non-photosynthetic. Photosynthetic plastids are chloroplasts, which contain primary and secondary photosynthetic pigments [30,121]. Examples of non-photosynthetic plastids include chromoplasts (synthesis and storage of pigments), amyloplasts (starch storage) and elaioplasts (oil storage).

1.4.2 Chloroplast biochemistry and the interrelation to Pi

Chloroplasts are present in all green plant tissues and they are the only plastids that can perform photosynthesis. They are composed of membranous thylakoid stacks called grana and a fluid matrix called stroma. The thylakoid harbors the light harvesting complexes of photosynthesis. During the light reaction of photosynthesis, electron transfer through the antenna complex in the thylakoid membrane leads to the production of ATP (by oxidative phosphorylation) and reduced cofactor NADPH. ATP and NADPH are ultimately utilized in the Calvin-Benson cycle within the stroma to

assimilate carbon dioxide into carbohydrates. Pi is required to convert ADP to ATP during photophosphorylation. Pi concentration in the stroma is critically important for photosynthesis and can be limiting by Pi deprivation [122].

Transporters located in the chloroplast inner membrane have a critical role in maintaining Pi homeostasis within the stroma. Members of the plastidic Phosphate Translocator (pPT) family of transporters facilitate the passage of Pi across the chloroplast membrane in exchange for phosphorylated compounds; often these transporters have overlapping specificities for phosphorylated substrates [123]. Pi translocators include phosphoenol pyruvate/Pi translocator (PPT), glucose 6-phosphate/Pi translocator (GPT) (expressed in non-photosynthetic plastids), xylulose 5-phosphate/Pi translocator (XPT), and triose phosphate translocator (TPT) [30,124-126]. TPT, the first member of the pPT family to be characterized, is responsible for the majority of Pi import in chloroplasts. Pi import by TPT plays an important role in balancing photosynthesis and carbon partitioning across the chloroplast membrane. TPT imports cytosolic Pi into the chloroplast in exchange for triose phosphates produced by the Calvin-Benson cycle. The triose phosphates are assimilated into sucrose in the cytosol. Consequently, Pi is released during sucrose synthesis, and is then transported into the chloroplast *via* TPT, whereas the synthesized sucrose is distributed to sink tissues for further utilization [127,128]. This cycle continues until the demand for sucrose in the sink tissues drops and sucrose synthesis in the cytosol declines. As sucrose synthesis slows, cytosolic Pi concentrations decrease, which ultimately leads to reduced stromal Pi levels. The triose phosphates that can no longer be transported to the

cytosol for sucrose synthesis are partitioned towards transitory starch synthesis within the stroma. Low Pi concentration in the stroma relieves the allosteric inhibition of Pi on ADP glucose pyrophosphorylase (ADG), which catalyzes the first committed step of starch synthesis [129-131]. Interestingly, *tpt* mutants compensate for the carbon allocation defect by increased starch synthesis and turnover [128,132]. A *tpt/adg* double mutant shows growth defects, which substantiates the need for increased starch synthesis in the *tpt* mutant background [133]. However, the absence of obvious growth deficiency of the *tpt* mutant implicates the presence of other Pi transporters on the chloroplast membrane that compensate for the defect in Pi transport.

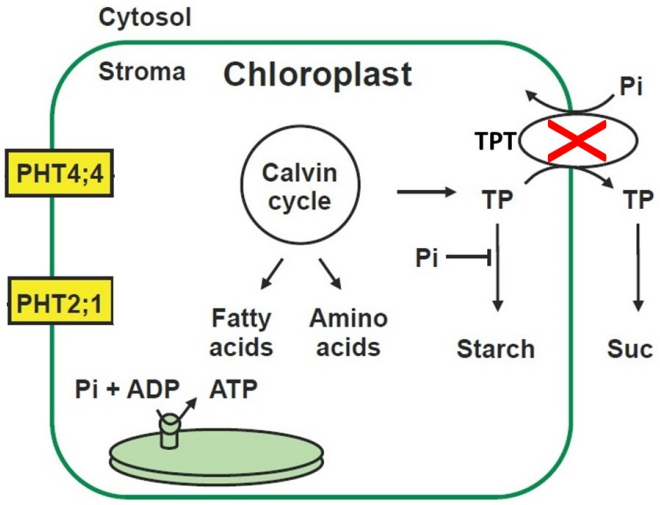

Figure 1. Schematic representation of a typical chloroplast with Pi transporters located in the inner membrane of the envelope. TPT, triose phosphate translocator; TP, triose phosphates. Plants are viable in the absence of TPT, which suggests compensatory Pi transport, which may be catalyzed by PHT2;1 and PHT4;4.

Sequence-based studies revealed two distinct families of plastidic Pi transporters, PHT2 and PHT4, which are unrelated to each other and to pPT transporters. PHT2 and PHT4 have sequence similarity with mammalian type III Na^+/Pi and type I Na^+/Pi transporters, respectively. Arabidopsis encodes a single PHT2 protein, PHT2;1, and six PHT4 proteins (PHT4;1 to PHT4;6). Functional studies performed in yeast revealed that PHT2;1 and all members of the PHT4 family transport phosphate. PHT4;1 is located in the thylakoid membrane, PHT4;2 is restricted to root plastids, PHT4;3 and PHT4;5 are located in plastids in the leaf phloem cells, PHT4;6 localizes to the Golgi apparatus, and both PHT2;1 and PHT4;4 are present in the chloroplast inner envelope membrane [134-138]. PHT2;1 and PHT4;4 are discussed in detail in Chapter 5 of this dissertation, along with their functional role in Arabidopsis. One of my objectives is to determine the role of PHT2;1 and PHT4;4 in fine tuning Pi concentrations in the chloroplast stroma.

1.5 *In vivo* measurement of Pi

In order to understand mechanisms underlying how plants use Pi, it is necessary to measure Pi concentrations in live plants with high spatial and temporal resolution. Diverse rates of Pi assimilation and recycling within different subcellular compartments can lead to high variability of cellular and subcellular Pi concentrations. However, available methods of Pi measurement lack the resolving capacity required to monitor intracellular Pi dynamics in real time.

Current methods used to measure *in vivo* Pi concentrations include ^{31}P nuclear magnetic resonance (NMR) spectrometry and ^{32}Pi radioisotope imaging. NMR has

limited spatial resolution. It can distinguish Pi in cell compartments with low pH (vacuole) from that in all other compartments combined (cytoplasm), but cannot distinguish differences between individual cells. Furthermore, NMR cannot monitor dynamic changes in Pi levels in intact plants because the assay setup requires cells or excised tissues [139,140]. Spectrometric techniques, e.g., energy dispersive X-ray microanalysis, synchotron X-ray fluorescence, can attain high-resolution quantitation of phosphorus; however, they require fixed samples, thus making it impossible to monitor live plants over time. Additionally, these techniques are unable to distinguish between inorganic phosphate and phosphorus. The inability to distinguish between P and Pi is also a major limitation of the ^{31}P radioisotope imaging system [141-143]. The above-mentioned constraints of current Pi measurement methods led to the development of novel techniques of live Pi monitoring in plants with high resolution.

Genetically encoded FRET based biosensors are highly effective tools for live Pi monitoring. These biosensors are non-destructive and they can be targeted to desired subcellular compartments. Many of these sensors are composed of two different variants of the green fluorescent protein (GFP) that are translationally fused on either side of a binding protein derived from a bacterial periplasmic binding protein (PBP). PBPs are components of the bacterial ABC transporter system. The GFP variants on either side of the PBP constitute the donor and acceptor of a Forster Resonance Energy Transfer (FRET) pair. FRET involves non-radiative energy transfer from an excited donor molecule to an acceptor molecule. Binding of ligand to the binding protein changes its conformation, which can be quantified as a change in FRET efficiency [144,145].

Exploiting this basic principle, scientists have developed biosensors for a number of analytes, including calcium, glucose, and maltose [146-149]. Gu *et al.* [150] developed a series of Pi biosensors termed Fluorescent indicator protein of Pi (FLIPPi), which are capable or reporting relative changes in cellular Pi concentrations. FLIPPi sensors have GFP variants cyan fluorescent protein (eCFP) and yellow fluorescent protein (eYFP) as the FRET donor and acceptor translationally fused to the N and C terimini of a *Synechococcus sp.* Pi binding protein (PiBP). Gu *et al*.'s study demonstrated the functionality of the FLIPPi sensors in cultured animal cells and showed that Pi binding to the FLIPPi sensor caused a concentration-dependent decrease in FRET **(Fig. 2**). However, the FLIPPi sensors were not ideally suited for reporting Pi changes in plant cells.

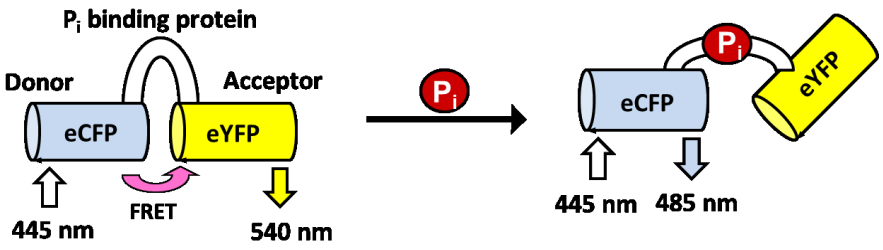

Figure 2. Schematic representation of the FLIPPi sensor. Pi binding leads to a conformational change in the protein, resulting in the loss of FRET.

Recently, Mukherjee *et al.* [151] developed a series of second generation FLIPPi sensors named cpFLIPPi, which were modified for reporting Pi concentrations in plants. The replacement of eYFP with a circularly permutated version of Venus increased the dynamic range of the sensor. Furthermore, targeted mutagenesis of the Pi binding protein yielded sensors with varied binding affinities (ranging from 0.08 mM to 11 mM in an in vitro assay), which made the sensors suitable for monitoring physiological Pi levels in most cell compartments. Their study demonstrated the functionality of the cpFLIPPi sensor in reporting changes in cytosolic Pi concentrations in root cells under Pi deprivation and resupply. The Pi sensor also resolved Pi accumulation defects in root plastids of *pht4;2* mutants which are defective in Pi export from root plastids. So far, ratiometric FRET sensors have been able to report relative changes in Pi levels resulting from environmental factors or genetic mutations. However, absolute quantification of Pi concentrations remains challenging due to the inability to mimic the intracellular chemical environment in *in vitro* assays. In Chapter IV of this dissertation I describe the development of an *in vivo* calibration of the Pi sensor to quantify cytosolic Pi concentrations in live plants. I also optimized ratiometric FRET-based analysis methods to study Pi dynamics in the Arabidopsis root and chloroplast.

CHAPTER II

IMAGING CELLULAR INORGANIC PHOSPHATE IN CAENORHABDITIS ELEGANS USING A GENETICALLY ENCODED FRET-BASED BIOSENSOR †

2.1 Introduction

Inorganic phosphate (Pi) is a component of nucleic acids and phospholipids, plays key roles in signal transduction cascades, and is a substrate for the generation of ATP via glycolysis and oxidative phosphorylation. The concentrations of Pi in different cells and both intra- and extra-cellular compartments must therefore, be maintained within certain limits, despite fluctuations in dietary supply and metabolic demand. Multiple Pi transporters, as well as metabolic recycling and excretory activities have been identified in animals [152,153]. However, a comprehensive understanding of their mechanisms and how these are integrated to achieve Pi homeostasis is limited by the inability to monitor Pi concentrations with spatial and temporal resolution. ^{31}P-NMR has been used to estimate Pi concentrations in acidic cellular compartments, such as vacuoles, but cannot readily distinguish concentrations in the pH-neutral compartments that comprise the cytoplasm [140]. This method also lacks the cellular and temporal resolution needed to accurately measure changes in Pi levels within single cells. Novel technologies, such as biosensors, are therefore needed to study Pi dynamics in live animals.

† This section is reprinted with permission from "Imaging cellular inorganic phosphate in *Caenorhabditis elegans* using a genetically encoded FRET-based biosensor" by Banerjee.S., Versaw.W.K., Garcia.L.R. *PLOS ONE 2015, 10(10).* Copyright 2015 by PLOS ONE.

Genetically encoded sensors, or biosensors, have proven to be effective tools for monitoring changes in the concentrations of small molecules and ions in live cells [146,154]. Such sensor proteins typically consist of a ligand-binding domain fused to one or two spectral variants of green fluorescent protein (GFP). Ligand binding to the sensor elicits concentration-dependent changes in protein conformation that are detected by changes in fluorescence intensity, fluorescence resonance energy transfer (FRET) or fluorescence lifetime imaging microscopy (FLIM) [155-158]. Sensors can be expressed in specific cells, targeted to specific cellular locations, and because their detection is non-destructive, organisms can be monitored over time.

Previously, Gu *et al*, [150] constructed a series of genetically encoded FRET-based Pi sensors named fluorescent indicator protein for inorganic phosphate (FLIPPi). FLIPPi sensors consist of a Pi binding protein (PiBP) derived from cyanobacteria *Synechococcus sp.,* translationally fused between enhanced cyan fluorescent protein (eCFP) and enhanced yellow fluorescent protein (eYFP). One FLIPPi variant with an *in vitro* dissociation constant (K_d) for Pi of 30 mM, FLIPPi-30m, was expressed in cultured animal cells to monitor cytosolic Pi. Changes in FRET indicative of altered cytosolic Pi concentrations were detected in Pi-starved CHO cells when treated with exogenous Pi, and also in COS-7 cells that co-expressed the human Na^+/Pi co-transporter, Pit2 [150].

Recently, Mukherjee *et al*, [151] modified a FLIPPi sensor to generate second-generation Pi sensors with greater dynamic range and binding affinities optimized for *in vivo* studies. Substitution of the eYFP portion of a FLIPPi sensor with a circularly permuted Venus, a pH- and chloride-insensitive version of YFP [159,160], enhanced the

dynamic range of the Pi-dependent FRET response. The resulting circularly permuted sensor was named cpFLIPPi. Mutagenesis of the PiBP component of cpFLIPPi yielded sensors with *in vitro* K_d values ranging from 80 μM to 11 mM. Cytosol- and plastid-targeted forms of the cpFLIPPi-5.3m sensor (K_d of 6.4 mM) were expressed in *Arabidopsis thaliana.* Live imaging with these transgenic plants revealed reversible changes in cytosolic Pi concentrations in response to Pi starvation and differences in the accumulation of Pi in plastids caused by Pi transporter mutations [151].

This study demonstrates the utility of live Pi imaging in a model animal, *Caenorhabditis elegans*. Ratiometric FRET analyses revealed changes in the concentrations of Pi in the cytosol of different cells and tissues during development and in response to environmental and metabolic cues, including nutrient starvation and exposure to a metabolic inhibitor. These results suggest that cytosolic Pi is a sensitive indicator of cellular metabolic status and that live imaging can be an effective approach to identify novel effectors of Pi homeostasis.

2.2 Results

2.2.1 Expression and ratiometric imaging of a Pi sensor in *C. elegans*

To assess the efficacy of live Pi imaging in *C. elegans*, it was necessary to determine whether consistently uniform expression of the Pi sensor could be detected. In this work, I used a cytosolic membrane-targeted cpFLIPPi-5.3m (**inset Fig. 3A**). The membrane localization aided in the imaging analysis, since it restricted the sensor to

specific cell regions, and thereby reduced its diffusion in photobleaching and microinjection experiments described later in this report. The use of a membrane-targeted sensor may lead to intermolecular FRET, but this would contribute to baseline FRET and therefore have minimal effect on measurements of changes in Pi dependent FRET. Initially the cpFLIPPi-5.3m was expressed in the intestinal cells, because this is where Pi and other nutrients are first assimilated. Moreover, previous studies showed that intestinal Pi metabolism is critical for growth and development of *C. elegans* [161-163]. I predicted that cytosolic Pi, and thus the corresponding FRET signals, would be similar across the intestine because the cells are interconnected by gap junctions [164]. As shown in **Fig. 3A**, eCFP donor emission and FRET emission from the Pi sensor were both roughly uniform throughout the intestine.

Several imaging-based methods have been described for quantitative analysis of FRET, including ratiometric approaches, e.g., FRET/donor and FRET/acceptor emission intensity ratios [165,166], and measurement of donor fluorescence lifetime [167]. FRET/donor ratiometric analysis represents the bulk of my studies (**Fig. 3B**). This approach provides high sensitivity because FRET (numerator) and donor eCFP emission (denominator) both change in response to ligand concentration and the changes are in opposite direction. In this analysis, a decrease in the FRET/donor ratio indicates an increase in cytosolic Pi concentration, whereas an increase in the ratio reports the opposite.

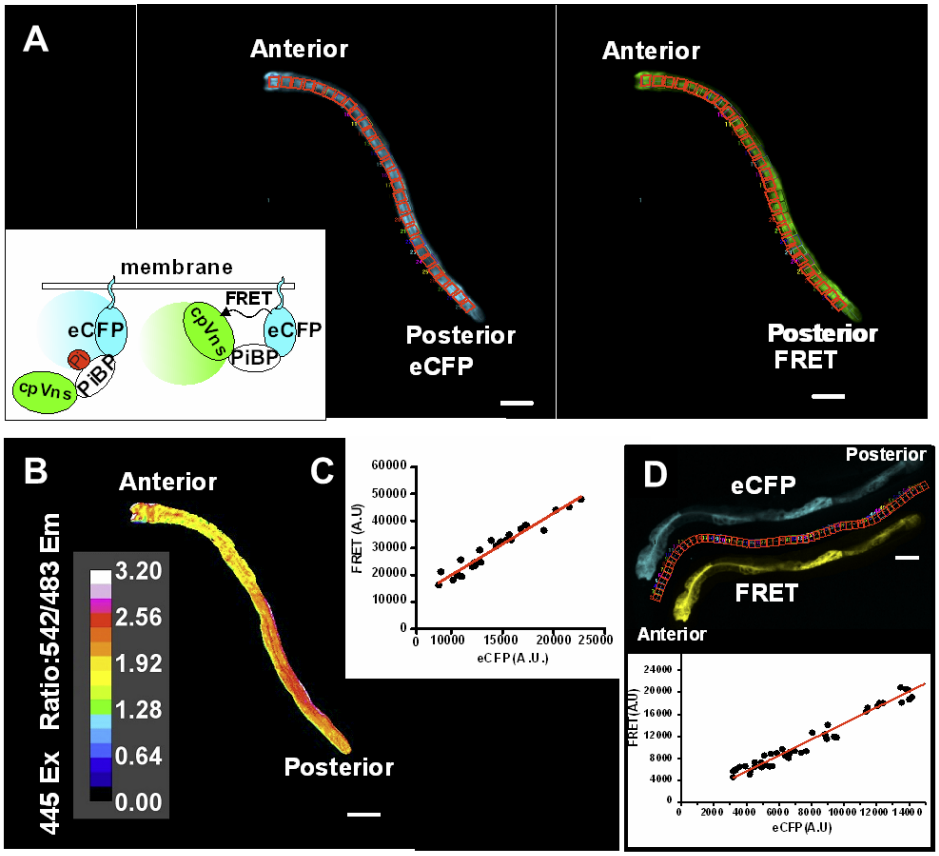

Figure 3. The FRET and eCFP ratio of cpFLIPPi-5.3m between intestinal cells of *C. elegans* is similar.

(A) eCFP and FRET emission channels, respectively showing donor and non-corrected FRET emission after the donor is excited with the 445nm laser. Inset shows schematic representation of cpFLIPPi-5.3m tethered to the cytosolic face of the cell membrane. Scale bar is 100 microns. (B) Pseudo-colored FRET ratio image was created by dividing FRET pixel intensity values by eCFP pixel intensity values. Color bar shows the range of FRET ratios in the intestine. (C) Plot of non-corrected FRET and eCFP mean intensity values obtained from arbitrary user defines ROIs. The red slope line was calculated as a linear regression (least-squares method) of the data points. Slope of the graph represents mean FRET/eCFP ratio of the intestine of a single animal. (D) The upper panel shows eCFP (top) and FRET (bottom) emission images of a 24 hr adult hermaphrodite with differential intestinal cpFLIPPi-5.3m expression. Scale bar is 100 microns. The red boxes between the images show the regions of interest (ROI) used to quantify the eCFP and uncorrected FRET emission intensities. The lower panel shows the eCFP intensities (in arbitrary units) plotted against the uncorrected FRET emission intensities for the animal in the upper panel. The red slope line was calculated as a linear regression (least-squares method) of the data points

Although expression of cpFLIPPi-5.3m appeared similar in the intestine, it was possible that differences in protein expression levels could affect FRET and/or eCFP signals. To test this possibility, mean FRET and eCFP emission intensities were measured within defined regions of interest (ROIs) that encompassed the entire intestine. Intensity values for both FRET and eCFP emission varied more than 2.5-fold at different positions in the intestine, but these were proportional over the entire range, as indicated by the plot of FRET versus eCFP in **Fig. 3C**. It was also found that within exceptional individuals, expression of the sensor can differ up to 4-fold in their intestinal cells (**Fig. 3D**), but still exhibit a proportional relationship between eCFP and FRET emission intensities. The slope of this line represents the composite FRET/eCFP ratio for the intestine, which reflects cytosolic Pi concentration. These results indicate that *in vivo* FRET/eCFP ratio is largely insensitive to protein expression levels. However, because it remained possible that FRET/eCFP may be inconsistent at very low or very high sensor protein concentrations, I restricted the analyses to worms that exhibited fluorescence intensities that can be captured within our camera's linear range. Also, the same laser and camera settings were used for all experiments, as specified in the materials and methods.

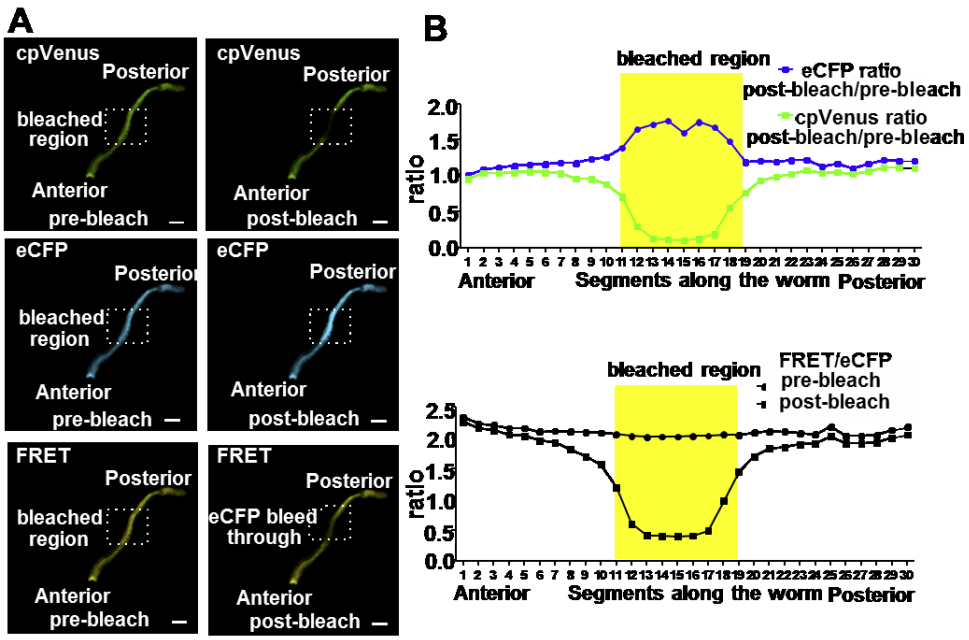

Figure 4. Fluorescence in the 445 nm excitation/540 nm emission channel includes approximately 30% eCFP cross emission. Percentage cross emission is calculated by photobleaching the acceptor. (A) A decrease in acceptor emission is accompanied by an increase in donor emission and a decrease in FRET emission in the acceptor-photobleached region of the intestine. (B) Graphs represent plots of eCFP emission (post bleach/pre-bleach), cpVenus emission (post bleach/pre-bleach), and FRET emission **Figure 4 continued:** (post bleach/pre-bleach) comparatively in the bleached and non-bleached regions of the intestine. FRET Excitation-445 nm: Emission- 542/27 nm, eCFP Excitation- 445 nm: Emission 483/32 nm. Scale bar is 100 microns

The eCFP emission spectrum partially overlaps with that of the FRET acceptor cpVenus. Consequently, some of the fluorescence attributed to FRET is due to spectral bleedthrough from eCFP [168]. To quantify the fraction of FRET emission due to eCFP spectral bleedthrough, an acceptor photobleaching approach was used [169]. The cpVenus component of the membrane-targeted cpFLIPPi-5.3m was photobleached in a portion of the intestine and this resulted in the expected increase in eCFP emission due

to dequenching of the FRET donor (**Fig. 2A**). The same treatment was applied to eight independent worms, and pre- and post-photobleach values for eCFP and cpVenus emission and for FRET/eCFP ratios across the entire intestine were analyzed (**Fig. 4B**). Photobleaching had no effect on fluorescent signals outside the targeted region, whereas FRET/eCFP of the bleached region was reduced to 32 ± 0.08% (n=8) of the pre-bleached value. This remaining signal represents the fraction of FRET due to eCFP bleedthrough. The bleedthrough fraction was therefore removed from raw FRET signals in all subsequent experiments.

2.2.2 Monitoring Pi-dependent FRET responses in live worms

I wanted to test how well the cpFLIPPi-5.3m sensor could report changes in the concentration of Pi in the cytosol of intestinal cells. However, it was first necessary to determine whether the microscope-imaging set-up can measure a dose-dependent Pi response of the sensor and its dynamic range. To estimate the Pi-dependent FRET response pattern of cpFLIPPi-5.3m under the same image acquisition settings as used for *in vivo* measurements, I prepared an *in vitro* calibration using purified cpFLIPPi-5.3m in protein dilution buffer containing different concentrations of Pi. Each solution was placed in a well of a silicone isolator adhered to a glass coverslip (**Fig. 5A inset**), and then imaged under the same camera settings and optics used for *in vivo* measurements. I measured a Pi-dependent FRET response indicative of single-site Pi binding (**Fig. 5A**). This result indicates that the optics of the microscope can report subtle changes in Pi concentration, similar to what we previously reported using a plate reader assay [151].

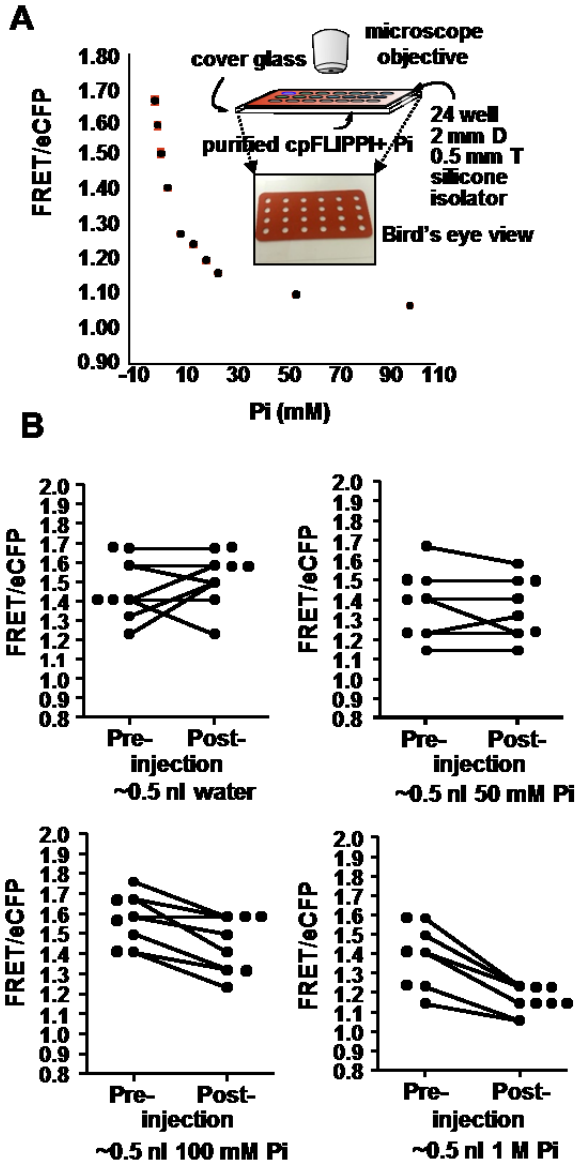

Figure 5. Direct Pi-induced changes in FRET response of cpFLIPPi-5.3m are demonstrated *in vitro* and *in vivo*. (A) *in vitro* Pi binding curves of cpFLIPPi-5.3m generated by mixing purified sensor protein with different Pi concentrations. Mean and standard deviation values were calculated from three individual wells. Inset shows a cartoon and bird's eye view of the silicone isolator apparatus for imaging solutions of Pi and the sensor. (B) *In vivo* Pi dependent FRET responses were measured by microinjecting Pi buffer at different concentrations into the intestinal cells. Plots show the effect of Pi injection on individual intestinal FRET ratios of the worms, before and 30 sec after Pi injection. FRET Excitation-445 nm: Emission- 542/27 nm, eCFP Excitation- 445 nm: Emission 483/32 nm.

The buffer composition in the *in vitro* assay most likely does not precisely mimic the intracellular context, therefore it was necessary to determine whether the cpFLIPPi-5.3m could report a dose response to Pi *in vivo*. My advisor, Dr. Rene Garcia, used microinjection to directly test the functionality of the sensor *in vivo*. To determine relative changes in FRET/eCFP ratio with changing *in vivo* Pi levels, Dr. Garcia injected 0.5 nL of different concentrations of Pi buffer directly into the intestinal cells of worms. For each worm, FRET/eCFP was measured before and approximately 1 min after injection. We reasoned that to restore homeostasis, the live worm intestine should attempt to remove and/or redistribute some of the excess supplied Pi; however, the injected concentrations should still elicit a cpFLIPPi-5.3m-measurable increase or dilution in the amount of cytosolic Pi. Indeed, the injections produced a Pi-dependent change in FRET/eCFP ratios (**Fig. 5B**). Some of the worms injected with water exhibited a rise in FRET/eCFP ratio, suggesting a dilution of the internal Pi concentration. However, with injection of ~5 nL of 100 mM and 1 M Pi, the intestinal FRET/eCFP ratio decreased, consistent with an increase in Pi concentration. Interestingly, the FRET/eCFP ratio of the worms injected with 50 mM Pi did not change significantly post injection suggesting that the intracellular Pi concentration in the worms after the injection might be similar to *in vivo* pre-injection Pi levels. *In vivo* Pi concentrations were estimated after injecting 0.5 nL of 50 mM Pi buffer in the intestine of the worm by calculating the volume of the cylinder-shaped intestine and assuming that the amount of injected Pi equilibrates throughout the whole volume of the intestine. These results suggest that the sensor can directly measure *in vivo* Pi changes, and that the average

concentration of Pi in the intestinal cytosol of the injected hermaphrodites is in the range of 5.8 mM.

The 50 mM Pi injection did not show a gross change in the average intestinal FRET/eCFP ratio possibly because much of the injected Pi equilibrated within the intestine during the time between injection and image capture. To see whether the sensor could detect rapid small changes in local Pi, Dr. Garcia injected a small volume (<0.1-0.2 nL) of 50 mM Pi buffer into an intestinal cell of five different animals. The dye propidium iodide was included in the Pi buffer to aid in monitoring the flow of the buffer within the intestine (**Fig. 6A**). FRET/eCFP was monitored 50-100 microns from the injection site before injection and every 4 sec after injection, for up to 20 sec. Continuous exposure to laser excitation will bleach the fluorophores of the cpFLIPPi-5.3m sensor. Thus, the same cells were imaged at 4-second intervals to minimize photo-damage of the cpVenus. We observed that FRET/eCFP ratio decreased locally immediately after injection (**Fig. 6B**). Although the FRET/eCFP ratio slightly readjusted afterwards, it remained below the initial value for the duration of the experiment. Taken together, these results indicate that cpFLIPPi-5.3m is capable of reporting small and rapid increases in cytosolic Pi concentration.

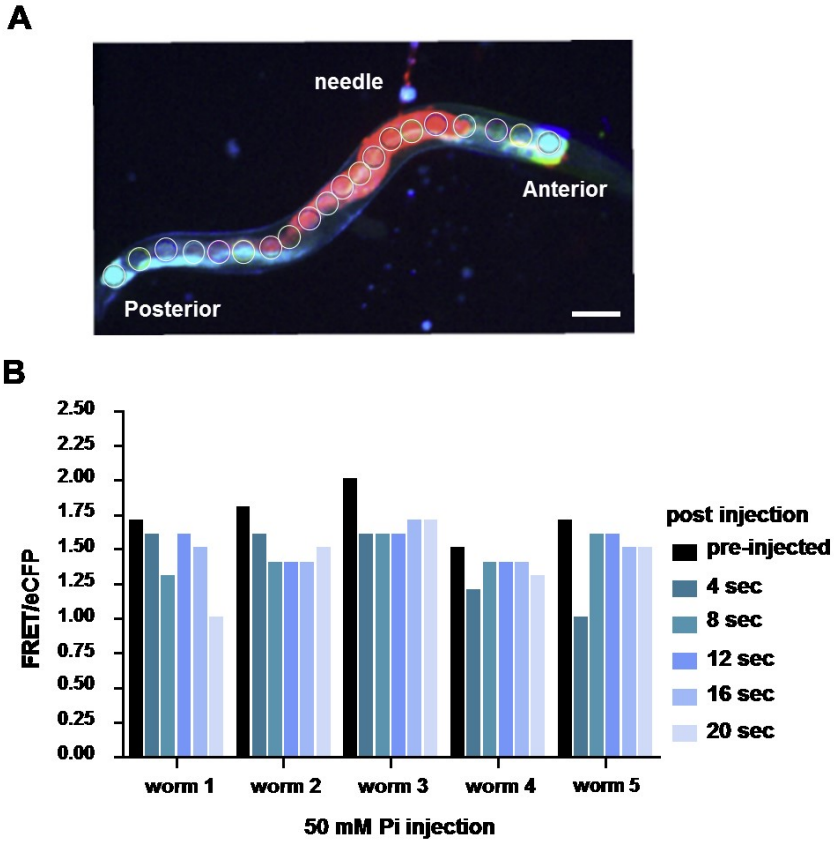

Figure 6. cpFLIPPi-5.3m can report rapid changes in Pi-induced FRET *in vivo*.(A) Image showing spread of the injected fluid along the intestine, visualized by injecting propidium iodide. (B) Rapid decrease in FRET/eCFP ratio after Pi injection into the intestinal cells. Bars represent mean FRET/eCFP ratio taken from ROIs 50-100 μm from the puncture. FRET Excitation-445 nm: Emission- 542/27 nm, eCFP Excitation- 445 nm: Emission 483/32 nm. Scale bar is 100 microns.

2.2.3 Monitoring the distribution of Pi in live worms

Studying *in vivo* Pi metabolism requires establishing Pi dynamics in the worm with respect to age and developmental stage of the animal. Previous studies have shown changes in the concentration of metabolites, including organic phospho-compounds, during larval development of the animals [170]. However, intestinal Pi concentrations in

live animals through different larval stages were unknown. Dr. Garcia imaged worms at different developmental stages, including hatched L1, L2, L3, L4, 10 hr adult hermaphrodite, 15 h adult male and 4 d adult hermaphrodites to measure relative FRET/eCFP of the intestine (**Fig. 7A**). The FRET/eCFP ratios we recorded depict a large variation in intestinal Pi in all the stages, essentially creating a range of Pi concentration, which the animals maintain. The mean FRET/eCFP obtained at the different developmental stages suggest that there is an average decrease in intestinal Pi as the worm matures beyond the hatched L1 stage. A possible explanation of this could be that the hatched L1 larvae still had abundant nutrients carried over from their embryonic stage, and may not have assimilated the free Pi into other macromolecules. In contrast, the range of Pi concentrations in the intestine were at relatively similar levels during the developmental stages of L2 through 15 h adult worms. 4 d old animals had lower levels of Pi in the intestine compared to other stages. I observed similar levels of sensor protein expression in the different developmental stages of the worms as measured by arbitrary fluorescence units (A.U) of eCFP in the following populations (mean +/- SD; n=23-25 for each population); L1: 3715 +/-2677, L2: 4426 +/-841, L3: 3678 +/-844, L4: 3515 +/-1079, Adult: 5705 +/-2945, 4 day old adult: 6972+/-3344 A.U. It was already established that FRET/eCFP ratios were constant over a 4-fold variation in fluorescent intensity values of the donor (**Fig. 3D**). Thus, these data strongly suggest that the variations in FRET/eCFP ratio were due to differences in Pi levels and not a consequence of different levels of sensor protein in the intestine of these animals. These findings suggest that Pi levels in the intestine of the worm can vary at the two extreme

ends of the development series; however, during the major part of their life span the animals maintain similar Pi levels in their intestine.

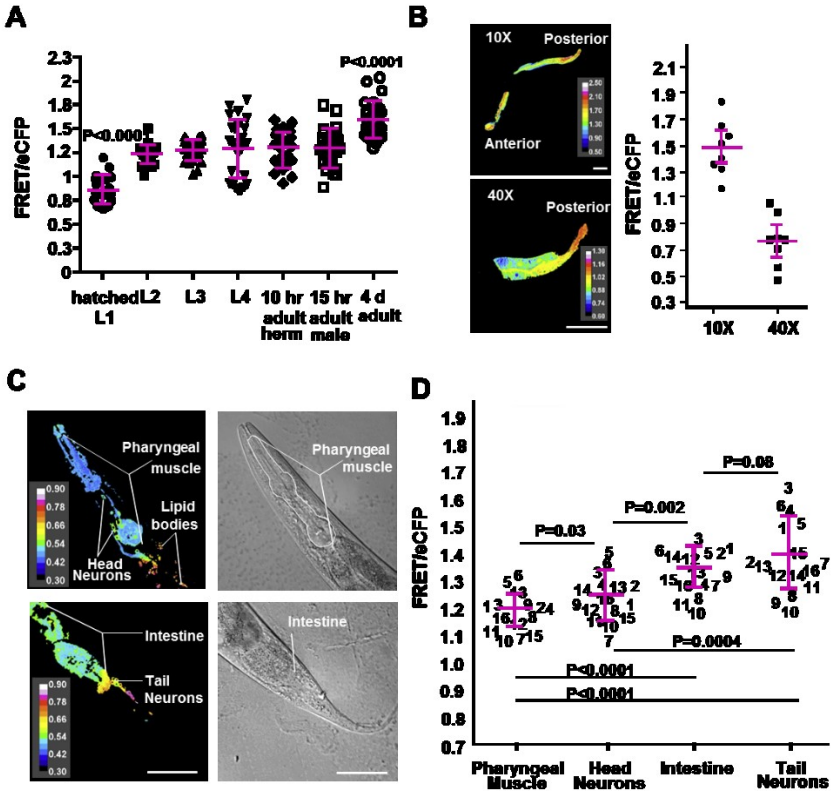

Figure 7. Pi levels differ during development and in different cell types. (A) Pi levels in the intestine of *C. elegans* at different developmental stages. Plotted data points represent mean FRET/eCFP ratios of the intestine of individual animals. (B) Intestinal FRET/eCFP ratio of a representative sample is depicted as a ratio image of FRET/eCFP. Mean FRET/eCFP values of 8 individual animals are plotted in the graph after imaging the same region of the intestine sequentially under 10x and 40x magnification. (C) Differential interference contrast micrographs and FRET/eCFP ratio images showing variation in FRET ratios in the pharyngeal muscle, head neurons, tail neurons and intestine of a representative animal. (D) Mean FRET/eCFP ratio values are plotted in the graph as separate distributions for individual cell types of 16 animals. FRET Excitation- 445 nm: Emission- 542/27 nm, eCFP Excitation- 445 nm: Emission 483/32 nm. Scale bar is 50 micron. P values were obtained from Student's T test.

After establishing the range of Pi levels in the intestine of the worms, I studied the patterns of Pi distribution in other cells and tissues of the animal. Since the intestine is the first organ for Pi entry and subsequent dissemination, I wanted to determine if the cytosolic Pi concentrations in different cells of the animal were similar to those in the intestine. To achieve this, I used the heat-inducible *hsp-16* promoter to express the cpFLIPPi-5.3m sensor throughout the body of the animal. This construct enabled measurement of FRET/eCFP ratios in different cell types, including head neurons, tail neuron, pharyngeal muscle and intestine. However, the time used for the heat shock promoter-expressed cpFLIPPi to accumulate in detectable amounts for these cells was not sufficient to provide a strong signal in other large cell types, such as the syncytial hypodermal cells. Unlike the intestinal cells, many of the other cells of *C. elegans* must be viewed with higher magnification. Unexpectedly, I found that FRET/eCFP ratios differed with 10x and 40x magnifications (**Fig. 7B**). This difference was a constant factor so an additive correction allowed comparisons of FRET/eCFP ratios at the two magnifications. Interestingly, comparisons of FRET/eCFP ratios in different cell types revealed a pattern in which Pi concentrations were highest in the pharyngeal muscles, followed by head neurons, intestine and tail neurons (**Fig. 7C** and **7D**). These cell-specific differences in Pi concentrations presumably reflect different physiological functions for each cell type. However, the mechanisms that give rise to these differences remain unknown. Nonetheless, these results established that the cpFLIPPi-5.3m sensor could distinguish Pi levels in different cell types of an animal and in different developmental stages under defined growth conditions.

2.2.4 Monitoring metabolic status of cells due to perturbations in the external environment

I finally asked if the FRET/eCFP ratio could report the metabolic status of the cells under altered environmental conditions. Under adverse external conditions such as food deprivation, there is no new external source of Pi. Thus, the supply of Pi to different cells of the animal should be limited. To maintain normal metabolic functions, the cells must carry out ATP synthesis; however, when access to Pi is limited by starvation, the cells should rely on recycling internal Pi stores. I predicted that the FRET/eCFP ratio should report the altered metabolic status of the cells under starvation as a change in the cytosolic Pi concentration. To measure FRET/eCFP in the pharyngeal muscles, head neurons, tail neurons and intestine of a food-stressed animal, I first starved 24 hour adult hermaphrodites for 6 hours on NGM plates lacking an OP50 bacterial lawn. A control group was maintained on NGM plates with OP50 bacteria for 6 hours and I imaged those worms in the same way. After 6 hours of starvation, the FRET/eCFP ratio increased in all cell types examined, indicating a decrease in Pi levels (**Fig. 8**). However, the effect of starvation on Pi concentration was not the same in all of the cell types. The relative decrease in Pi was greatest in the intestine and head neurons of the worms, followed by the tail neurons and pharyngeal muscle. Hence, I inferred that nutrient starvation causes a decrease in cytosolic Pi concentrations in different cell types of the worms by different magnitudes, suggesting their varied metabolic functions, Pi demand and utilization.

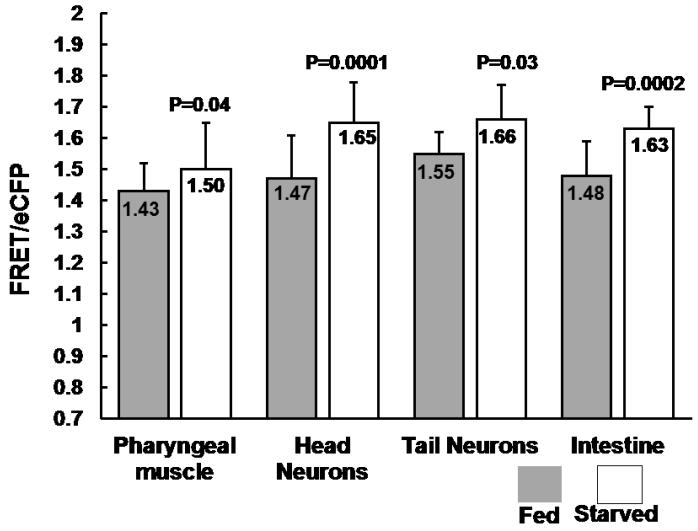

Figure 8. Nutrient starvation alters Pi levels in different cell types of *C. elegans.* 24 h adult hermaphrodites were held in NGM plates without bacteria and imaged to compare FRET ratios with the control group, maintained in NGM plates with bacteria. Plotted values are mean FRET/eCFP with standard deviation measured from 13 independent worms. FRET Excitation-445 nm: Emission- 542/27 nm, eCFP Excitation-445 nm: Emission 483/32 nm. P values were obtained from Student's T test.

Since a limitation in Pi supply resulted in decreased cytosolic Pi concentrations, I wanted to determine if inhibition of respiration could increase Pi levels. Metabolic inhibitors such as cyanide inhibit ATP synthesis during aerobic respiration [171]. Since the living cells still have to hydrolyze ATP, and thereby liberate Pi to perform cellular functions, I predicted that cyanide treatment should result in an accumulation of free Pi in the cell cytosol. I treated 24 hour old hermaphrodites with 10 mM sodium cyanide and imaged them prior to and 1.5 to 2 min after the cyanide treatment to measure the FRET/eCFP ratio (**Fig. 9A**). I optimized the imaging time based on the time it took for the worms to reduce their locomotion. Unexpectedly, the cyanide treatment affected the

in vivo fluorescent properties of the sensor, resulting in a general decrease in fluorescent intensity of cpVenus and to a lesser extent eCFP. This was not a direct effect of sodium cyanide on the sensor protein, because it had no effect on FRET/eCFP ratios when added directly to purified sensor protein in *in vitro* Pi binding assays (**Fig. 9B**). Thus, I hypothesize that the indirect effect on the fluorophores was due to alterations in the intracellular environment, aggravated by the cyanide treatment. This effect complicated the FRET/eCFP ratio analyses, since the changes in eCFP emission, due to Pi-mediated FRET energy transfer, might no longer be related to the cyanide-induced reduction of the FRET-derived cpVenus emission. To work around this issue, I instead calculated the FRET ratio by dividing FRET by the cpVenus emission. This method is not as sensitive as dividing FRET by eCFP because the magnitude of the FRET/cpVenus ratio is smaller than FRET/eCFP ratio. However, since this ratio incorporates the emission of the same fluorophore, I reasoned that the effect of cyanide should reduce the fluorescence intensity of the 445-excited FRET and the standard 515-excited emission proportionately, thus allowing the 515-excited emission to be a reference for FRET changes. Indeed, it was found that over a range of fluorescence intensities, the plot of FRET/cpVenus is linear (**Fig. 9C**) suggesting that this normalization method corrects any adverse effect of cyanide in the resultant FRET ratio. Using this method, I found cyanide decreased the FRET/cpVenus ratio in the pharyngeal muscle, head neurons and tail neurons of the worms (**Fig. 9A**). The decrease in FRET/cpVenus ratio is as predicted, since physiological ATP hydrolysis, coupled with cyanide-attenuation of ATP

synthesis should increase cytosolic Pi. However, the intestine showed the opposite response, suggesting that cyanide treatment caused a decrease in intestinal Pi content.

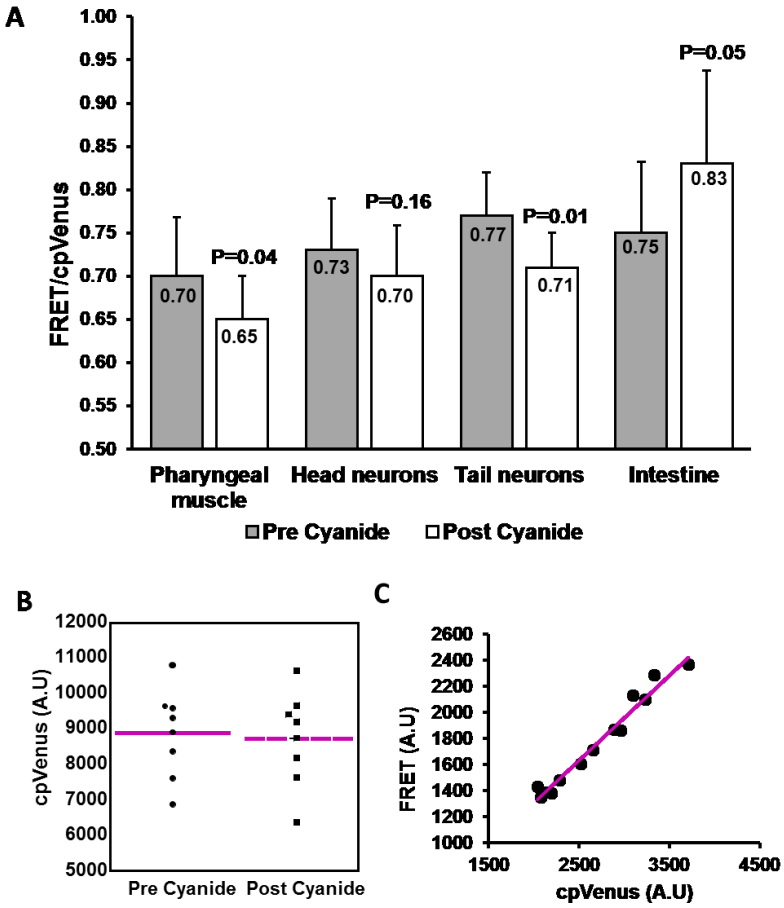

Figure 9. Cyanide treatment alters Pi levels in different cell types of *C. elegans.* (A) 24 h adult hermaphrodites were imaged prior to and after treatment with 10 mM sodium cyanide. Plotted values are mean FRET/cpVenus with standard deviation measured from 11 independent worms. (B) Graph shows the effect of cyanide on fluorescence intensity of purified sensor protein. Plotted data represent mean cpVenus intensity from 8 independent wells. (C) Plot shows the effect of cyanide on FRET/cpVenus ratios of *C. elegans* intestinal cells. The FRET/cpVenus ratio was calculated from multiple ROIs in the intestine of a worm after treating it with 10 mM sodium cyanide.

One possible reason for the lower intestinal Pi content is that cyanide induces excretion of intestinal contents, including phosphate. To test this possibility I treated 35-40 worms with 10 mM sodium cyanide solution while holding them in an external buffer solution containing 1.7 µM cpFLIPPi sensor protein. If the worm's intestinal cells excreted their excess cytosolic Pi then the FRET/eCFP ratio calculated from imaging the external sensor-buffer solution would decrease. I added the worms to a total liquid volume of 5 µl in a silicone isolator well and imaged the protein solution in the well prior to and after treating the worms with sodium cyanide. I found that after the cyanide treatment, the FRET/eCFP ratio of the well decreased, indicating increased Pi in the well (**Fig. 10**). The decrease in FRET/eCFP was maximal after 2 min of cyanide treatment and stabilized thereafter, consistent with the idea that the Pi in the well was released from the intestine of the worms, rather than from continual breakdown of the animal's cellular components. This effect was not observed in negative controls where the worms were treated with extra sensor protein solution instead of sodium cyanide. These results support the hypothesis that cyanide treatment causes increased cytosolic Pi levels due to inhibition of respiration in certain cells of the animal, while the intestine (and possibly other cell types that were not imaged) undergoes secretion of contents, which includes Pi.

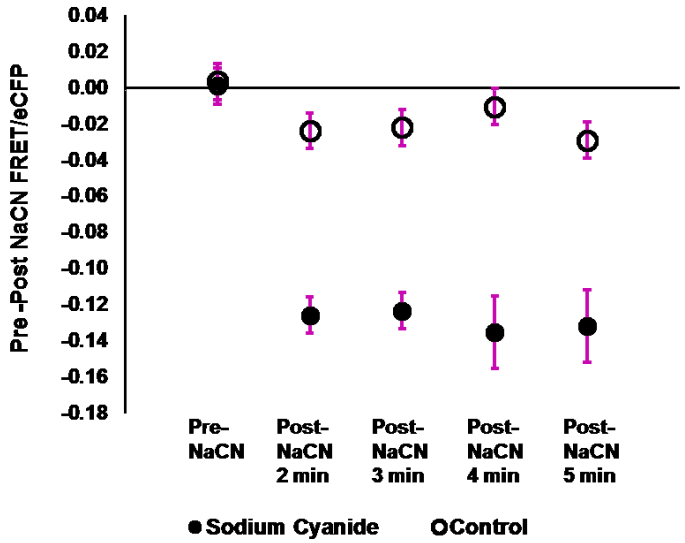

Figure 10. Cyanide causes expulsion of intestinal Pi. Temporal profile of Pi expulsion from the intestine after cyanide treatment. Protein solution in the silicone well was measured at 1 min intervals up to 5 min after treating the suspended worms with 10 mM sodium cyanide. The maximum decrease in FRET/eCFP ratio is observed after 2 min then remains stable. The control group was treated with extra sensor protein solution instead of 10 mM sodium cyanide. Data shows mean and standard error values of measurements taken from three individual wells.

2.3 Discussion

Measuring the amount of Pi present in a tissue or cell extract is straightforward with current analytical methods, but novel tools and methods are needed to track changes in Pi concentrations within individual cells of a live animal. In this study, I explored the utility of ratiometric imaging of a genetically encoded FRET-based Pi sensor, cpFLIPPi-5.3m, for monitoring cellular Pi concentrations in *C. elegans*. Demonstrating the efficacy of the sensor in the context of a live animal was a critical first test. The relatively large and interconnected cells of the intestine were ideal targets.

Indeed, changes in FRET/eCFP ratios after injection of Pi solutions or water directly into intestinal cells confirmed that the cpFLIPPi-5.3m sensor is responsive to both increased and decreased Pi concentrations within the worm's intestinal cellular environment.

Endogenous intestinal Pi concentrations varied throughout development with a consistent pattern. Specifically, Pi concentrations were greatest in freshly hatched L1 larvae, which may reflect a large maternal supply of Pi, then decreased in L2 and remained relatively constant through the young adult stages, then decreased further in older adults. This cellular pattern largely mirrors that of overall metabolic status as previously defined from studies of oxygen consumption rates and ATP accumulation [172,173]. That is, as the developing larva metabolizes its food via oxidative processes, intracellular Pi concentrations are expected to decline due to incorporation into organic molecules, including ATP. This situation must differ in older adult worms because their metabolic rates are lower than during the larval stages [170], yet they have significantly less free Pi. It is unknown, but possible, that older adult animals lose a large fraction of intestinal Pi through excretion. Although the results show that intestinal Pi concentrations decline as the population ages, there is also a large range of concentrations in each developmental stage. This biological variation suggests that intestinal Pi levels are not tightly fixed, but are instead maintained within a range, presumably to account for variation in factors such as developmental progression, behavioral activity, feeding and reproduction.

One can attempt to estimate absolute Pi concentrations corresponding to *in vivo* FRET/eCFP ratio values by directly cross-referencing the *in vitro* calibration curve (**Fig.**

5A). For example, the average intestinal FRET/eCFP ratio value for adult animals was 1.4 (**Fig. 5B**), which corresponds to ~5.0 mM Pi based on the *in vitro* calibration curve. This simple comparison, however, can be problematic because chemical environment can affect fluorescence outputs of the eCFP and cpVenus components of the sensor, and it is difficult to predict how closely the environment of the *in vitro* assay solution mimics that of the cytosol. Nevertheless, the concentration estimated from the *in vitro* calibration is in remarkably close agreement with the independent estimate of ~5.8 mM derived from Pi injection experiments, where the final Pi concentration was calculated from the volume of the intestine and the amount of Pi injected that caused no gross change in the FRET/eCFP ratio (**Fig. 5B**).

The Pi binding dissociation constant imposes an inherent limitation on the range of Pi concentrations that can be probed with the cpFLIPPi-5.3m sensor. That is, it is not possible to accurately resolve concentrations that are far below and far above the K_d. This limitation exists for all non-linear binding assays. Moreover, the *in vivo* measurements across the different developmental stages (**Fig. 7A**) revealed individuals that display FRET/eCFP ratios outside the extremes of the *in vitro* Pi calibration curve, especially in the hatched L1s (ratio: 0.7) and the 4-day-old adults (ratio: 2). The discrepancy at the tails of the calibration curve suggests that the chemical environment of the *in vitro* assay solution does not fully mimic that of the cytosol at these extremes. Therefore, these extreme *in vivo* data values were coupled with the *in vitro* calibration curve to generate a model that encompasses the full range of *in vivo* cellular Pi changes. The *in vitro* FRET/eCFP curve can be described by single-site binding equation: R-

$R_o=(R_{max}-R_o)*L)/(K_d+L)$ where R is the FRET ratio, R_o is the FRET ratio with no ligand, R_{max} is FRET ratio at saturation, L is ligand (Pi) concentration, and K_d is the dissociation constant. For the *in vitro* calibration (**Fig. 5A**), R_o is 1.7, R_{max} is 1.1 and K_d is 6.4 mM. If the minimum (ratio: 0.7) and maximum (ratio: 2) FRET/eCFP values measured from *in vivo* samples are substituted for R_o and R_{max}, respectively, then one can modify the *in vitro* curve to roughly accommodate all data points obtain from the *in vivo* data (**Fig. 11A**). If needed, this data treatment can also easily be used to generate a curve using FRET/cpVenus values (**Fig. 11B**) instead of FRET/eCFP values. However, this model assumes that the Pi binding dissociation constant is the same under both *in vitro* and *in vivo* conditions.

When the average FRET/eCFP value for adult worms (1.4) is applied to the modeled *in vitro* calibration curve (Fig. 9), it corresponds to ~5.5 mM Pi, which is nearly identical to the estimates without modeling and also from Pi injection. However, the similarities of these values may reflect the fact that the concentrations are within the resolving range of the sensor, i.e., near the K_d. Estimates of concentrations far from the K_d remain suspect. We propose a conservative approach in which estimates are limited to the concentration range spanning from 0.25x to 4x the K_d value (**Fig. 11**). These limits also correspond to 20% and 80% of maximum sensor binding. With these limits in mind, we estimate that the intestinal Pi concentration in newly hatched L1 larva is at least 25 mM, and is no more than 1.6 mM in post-reproductive 4-day-old adults. Sensors with significantly different affinities for Pi could be used to define these extreme concentrations with greater precision [151].

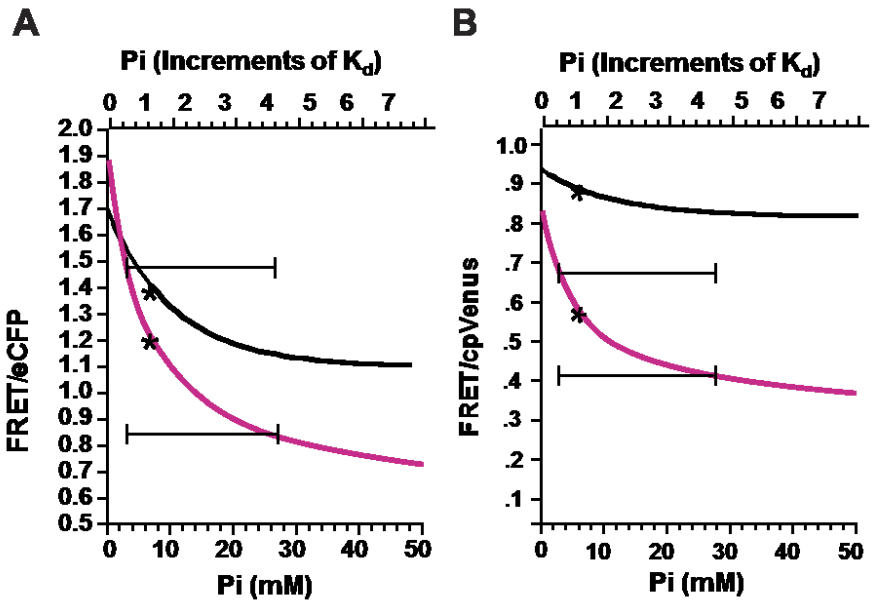

Figure 11. ***In vivo*** **Pi response models generated from the** ***in vitro*** **Pi binding curves.** The black lines represent the experimentally generated dose dependent Pi response curve of purified cpFLIPPi-5.3m protein plotting Pi concentration against either (A) FRET/eCFP or (B) FRET/cpVenus. The curves follow the binding equation: $R-R_o=(R_{max}-R_o)*L)/(K_d+L)$. R is the FRET ratio; R_o is the FRET ratio with no ligand (Pi); R_{max} is the FRET ratio at ligand saturation; L is ligand (Pi); K_d is the apparent dissociation constant. From the FRET/eCFP curve, R_o is 1.7, R_{max} is 1.1. From the FRET/cpVenus curve, R_o is 1.0, R_{max} is .88. The apparent K_d for both curves is 6.4 mM. The magenta lines represent the model of *in vivo* Pi dependent response curves generated by substituting the R_o and R_{max} for (A) FRET/eCFP or (B) FRET/cpVenus tail values measured from *in vivo* L1 larva and old adult animals. The K_d was kept the same as the *in vitro* curve. The asterisk represents the K_d. The capped lines represent the Pi range between 0.25x and 4x of the K_d.

I also observed distinct tissue- and cell-specific patterns in cytosolic Pi concentrations. Since these different sites (head neurons, tail neurons and pharyngeal muscle) must initially rely on the intestine for nutrient supply, the different Pi profiles of the cells, which also varied from the anterior to the posterior of the animal, suggest the existence of complex mechanisms that regulate the transport, assimilation and recycling

of Pi. These differences may also reflect distinct capacities to respond to changes in dietary supply. Under laboratory conditions, *C. elegans* develop on nematode growth media, which contains ~25 mM Pi. This external Pi supports the growth of the bacteria that the worm eats, but is not used by the worm directly [174]. Instead, *C. elegans* obtains its Pi from catabolizing the phospho-compounds of its bacterial food [175,176]. Consequently, Pi deprivation is coupled with overall nutrient deprivation.

Previous studies have shown that nutrient deprivation promotes physiological changes that allow the organism to cope with this adverse condition. For example, nutrient-deprived animals decrease their normal rate of transcription and translation, and initiate degradation of internal energy stores and macromolecules [177-180]. We found that starving animals for just 6 h was sufficient to reduce cytosolic Pi concentrations in all of the cells examined. However, the magnitude of the reduction differed for each cell type suggesting distinct rates of Pi recycling and/or metabolic activities.

In contrast to the reduction in cytosolic Pi levels associated with nutrient deprivation, exposure to cyanide, a mitochondrial electron transport chain inhibitor, increased Pi concentrations in head and tail neurons and in pharyngeal muscles. This increase was expected given the inability to recycle Pi into mitochondrial-produced ATP in the presence of cyanide. Similar effects on cellular Pi have been observed from NMR studies for anoxia, azide and cyanide treatments [181], but the changes in Pi concentrations reported in these studies represent bulk changes due to the lack of cellular resolution. Interestingly, cyanide treatment reduced Pi concentrations in the intestines. The results suggest that the reduction is due, at least in part, to excretion of Pi to the

external environment. These findings indicate that, in spite of internal recycling mechanisms to maintain cellular Pi levels, the intestinal cytosol is sensitive to external perturbations, and that the cpFLIPPi-5.3m sensor can, within limits, resolve subtle changes in Pi as a read-out of the cell's reaction to these perturbations.

2.4 Materials and Methods

2.4.1 Strains and culture methods

Strains were maintained at 20°C on NGM agar plates and fed with *E. coli* OP50. Alleles used in the study were: *pha-1(e2123)* LGIII [182], *him-5(e1490)* allele LGV [183] and *lite-1(ce314)* LGX [184]. Transgenic strains include: *rg*Ex682[P*gtl-1*:*FLIPPi-6.4m*]; *him-5 (e1490)*, *rg*Is13 [integrated P*gtl-1*:*FLIPPi-6.4m*]; *pha-1(lf),him-5(e1490), lite-1(lf), rg*Ex730[P*hsp-16*:*FLIPPi-6.4m*+ pBX1];*pha-1(lf),him-5(e1490), lite-1(lf), rg*Ex725[P*hsp-16*:*Pi binding protein-6.4m*::cpVenus + pBX1].

2.4.2 Plasmids

Construction of cpFLIPPi-5.3m was previously described [151]. In brief, cpFLIPPi-5.3m is a chimeric protein in which the cyanobacterial Pi binding protein [150] is sandwiched between eCFP and circular permuted Venus. The K_d for Pi binding to the purified sensor protein is 6.4 mM when assayed at pH 7.5. In this work, cpFLIPPi-5.3m was translationally fused to the first 91 amino acids of the beta integrin protein PAT-3 [185]. This region of PAT-3 targets cpFLIPPi-5.3m to the cytoplasmic side of the

cell membrane, as well as labeling intracellular perinuclear membranes. The sensor was targeted to the cell membrane to minimize the effects of different promoters on protein accumulation and to restrict the sensor to the desired cells. This targeting also facilitated imaging because small amounts of the sensor were more readily detected when localized to specific regions of the cell.

pPD122-39 (Addgene), a vector from the Fire plasmid collection [186], was used as the source for the membrane targeting sequence. The plasmid contains the PAT-3 membrane localization sequence (MLS) fused to GFP and the *unc-54* 3' UTR. The GFP sequence was removed from the plasmid using inverse PCR and the primers 5'-tagcattcgtagaattccaactgagcgccg and 5'-tttttctaccggtacctcggatctatcatgaag. A 2.6 kb *BamH*1-*Hind*III fragment containing cpFLIPPi-5.3m was cut from pRSET/cpFLIPPi-5.3m [151] and ligated to the GFP-deleted PAR-3 MLS plasmid. The gateway ATTR cassette C.1 (Invitrogen, CA) was then ligated to a *Sma*1 site to create the destination plasmid pLR318. The 1.6 kb ATTL-flanked intestinal *gtl-1* promoter, contained in the plasmid pBL63 [187] was then recombined with pLR318, using LR clonase (Invitrogen) to generate the plasmid pLR316. The *hsp-16* heat shock promoter was PCR-amplified from genomic DNA using the primers: 5'-ggggacaagtttgtacaaaaaagcaggcttaagcttgcatgcctgcagg and 5'-ggggaccactttgtacaagaaagctgggtgctagccaagggtcctcct. The 540 bp ATTB-flanked *hsp-16* heat shock promoter was then recombined with the plasmid pDG15, using BP clonase (Invitrogen) to generate the plasmid pBL172. The ATTBL-flanked *hsp-16* promoter in pBL172, was then recombined with pLR318, using LR clonase, to generate the plasmid

pLR323. To determine how much 542 nm emission from cpFLIPPi-5.3m was due to direct excitation of cpVenus by the 445 nm laser, the eCFP sequence from pLR323 was removed using inverse PCR and the phosphorylated primers: 5'-gggatcggtaccgtaggatttctaacagcgacctcggctcaagccc and 5'-gcggcccggatctttttctaccggtacctcggatctatcatgaag. The plasmid was religated to generate pLR324.

2.4.3 Transgenics

To generate the *rg*Ex682 [P*gtl-1*:cpFLIPPi-5.3m] transgenic line, a mixture of 50 ng/µl of pLR316 and 150 ng/µl of pUC18 was injected into the germline of N2 hermaphrodites [188]. Stable transmitting lines expressed cpFLIPPi-5.3m in the intestines from an extrachromosomal array. To integrate the extrachromosomal *rg*Ex682 array into the genome, transgenic hermaphrodites were treated with 30 µg/ml trimethylpsoralen for 30 minutes and exposed to 340 µW/cm^2 UV for 1 minute [189] to create the line *rg*Is13 [integrated P*gtl-1*:cpFLIPPi-5.3m]. Two factor genetic mapping placed the integrated P*gtl-1*:cpFLIPPi-5.3m on chromosome I. To generate *rg*Ex730 [P*hsp-16*:cpFLIPPi-5.3m+ pBX1] and *rg*Ex725 [P*hsp-16*:*Pi binding protein-6.4m*::cpVenus +pBX1] transgenic lines, DNA mixtures containing 50 ng/µl of pLR323 or pLR324, 50 ng/µl of pBX1 (*pha-1* plasmid) and 100 ng/µl pUC18 were injected into the germline of *pha-1(lf),him-5(e1490), lite-1(lf)* hermaphrodites. *pha-1*-rescued transformants, which can stably propagate at 20°C, were then selected.

2.4.4 Live imaging and FRET analysis of cytosolic Pi

Worms expressing the cpFLIPPi-5.3m sensor were imaged to measure Pi-dependent FRET in the intestine, head neurons, tail neurons and pharyngeal muscle. Worms were transferred to a glass slide with a thin layer of 8% noble agar, immobilized with 25 mg/ml Polybead polystyrene 0.1 μm microspheres (Polysciences, Inc., WA) [190] and covered with a glass cover slip prior to imaging. Hermaphrodites were developmentally staged based on the cell division patterns of the vulval P5.p, P6.p and P7.p cell descendants. Mounted animals were analyzed on an inverted Olympus IX81 microscope equipped with a Yokogawa CSU-X1 Spinning Disk confocal unit and an iXon897 EMCCD camera (Andor Technology, USA). Animals were viewed with 10x (0.3 n.a) or 40x (oil-immersion 1.3 n.a.) objectives. The laser wavelength used for CFP excitation was 445 nm. The emission filter for CFP was 483/32 nm and the emission filter for FRET was 542/27 nm. The laser wavelength used for direct excitation of cpVenus was 515 nm. The same laser excitation and image acquisition settings (in Metamorph software) were used for all experiments: 40% laser power for the 445 nm laser, 10% laser power for the 515 nm laser, 1000 ms exposure time, electron multiplier gain set at 13%, and pre-amplifier gain set at 5%. Image analysis was done using ImageJ software and statistics were conducted using Graphpad Prism 5 (version 4.03) software. Regions of interest were drawn across the image and mean intensity values were measured in the CFP, FRET and cpVenus emission channels. FRET intensity values were corrected for donor spectral bleedthrough, which was determined by acceptor photobleach. To photobleach cpVenus, a 100x oil-immersion (1.35 n.a.) objective was

used to focus on a section of the intestine, and a 515 nm excitation laser was then used at maximum intensity. FRET ratios were calculated as the corrected FRET emission (445 ex: 542 em) divided by the eCFP emission (445 ex: 483 em).

Comparative analysis of neurons, pharyngeal muscles and intestine was carried out by imaging the animals with a 40x (oil-immersion, 1.3 n.a.) objective. To correct for any possible alteration in the FRET/eCFP values due to changes in image acquisition between the 10x (0.3 n.a) and 40x (oil-immersion 1.3 n.a.) objectives, the intestine of the same worm was imaged sequentially using the two camera acquisition settings to calculate FRET/eCFP ratio. Mean FRET/eCFP values were calculated from the same region of the intestine imaged under 10x and 40x. The difference between the mean FRET/eCFP ratios was used as an additive correction factor for all subsequent experiments carried out using the 40x objective.

Sodium cyanide treatment differentially reduced eCFP and cpVenus fluorescence intensities of cpFLIPPi-5.3m when the sensor was expressed in worms, but not when treated *in vitro*. We attribute this effect to undefined changes in the cellular environment. Because the effect of cyanide on eCFP would influence both the numerator and denominator components of the FRET/eCFP ratio, we instead normalized corrected FRET values by emission intensity values of directly excited cpVenus (515 ex: 542 em), i.e., FRET/cpVenus. In this case, raw FRET intensities were corrected for both donor spectral bleed-through and acceptor cross-excitation. The cross-excitation correction factor was determined by imaging *rg*Ex725 [P*hsp-16*:*Pi binding protein-6.4m*::cpVenus

+ pBX1] worms, which expressed cpVenus fused to the C-terminus of the Pi binding protein.

2.4.5 In vitro Pi binding assay

The cpFLIPPi-5.3m sensor was expressed in *E. coli* BL21 (DE3) and the protein was purified from 100 ml culture lysates using immobilized metal affinity chromatography. The sensor protein was dialyzed against 20 mM Tris-HCl (pH 7.5) overnight at 4°C. Protein concentration was quantified using the Bradford colorimetric assay then diluted in protein dilution buffer, 100 mM K-gluconate, 30 mM NaCl, 25 mM MES, 25 mM HEPES, 40% sucrose, pH 7.5 [151] to yield fluorescence intensity values equivalent to those detected *in vivo*. Different concentrations of potassium phosphate buffer (pH 7.5) were added to the diluted sensor then 5 µl aliquots were transferred to individual wells of a 24-well silicone isolator (Electron Microscopy Sciences, Hatfield, PA). The wells were imaged for Pi-dependent FRET using an epifluorescence–equipped Olympus BX51 upright compound microscope (Olympus, USA) with a 10x objective. Image capture settings were the same as those used for *in vivo* analyses. FRET ratio data were fit to a single-site binding isotherm to estimate dissociation constant (K_d) values.

2.4.6 Nutrient starvation and cyanide treatment

To study the effect of environmental conditions on cellular Pi levels, worms were subjected to nutrient starvation and exposure to the respiratory inhibitor sodium cyanide. Worms were grown on Nutrient Growth Media (NGM) plates seeded with a saturated

culture of *E.coli* OP50. 24 h adult hermaphrodites containing the P*hsp16*:cpFLIPPi-5.3m sensor were heat-shocked at 32°C for 1 hour to allow induction of the heat shock promoter, then returned to room temperature (22-24ºC) for 3 hours before imaging. For the starvation experiment, fluorescent worms were selected after heat shock, transferred to NGM plates with or without *E.coli* OP50, and maintained in the respective plates for 5 hours. Fed and starved worms were imaged within 5-7 hours of starvation. For the cyanide treatment, fluorescent worms were transferred from NGM plates to a thin layer of 8% noble agar on a glass slide, immobilized with 25 mg/ml 0.1 μm polystyrene beads (Polysciences, Inc., WA) [190] then imaged. The same worms were then treated with 2 μl of a 10 mM NaCN solution for 30 sec, then quickly covered with a glass cover slip and imaged within 1.5 to 2 min after addition of cyanide. To detect expulsion of Pi from worms, 35-40 worms were suspended in 5 μl of a 1.7 μM cpFLIPPi-5.3m protein solution in a single well of a 0.5 mm silicone isolator. The protein solution was imaged before and after addition of sodium cyanide to a final concentration of 10 mM then imaged over 5 min at 1 min intervals. The control group of worms was treated with sensor protein solution instead of sodium cyanide.

2.4.7 Microinjection of inorganic phosphate

Animals were injected with phosphate buffer using a technique similar to germ line microinjections [188]. In brief, two-day old adult *rg*Is13 hermaphrodites were first immobilized with 1-2 μl of freshly made 1 M dopamine (Sigma) (dissolved in water). Even after the dopamine extensively oxidizes in air, it will still paralyze the worm in

seconds. Dopamine was used as a paralytic, rather than the more commonly used sodium azide, since we did not want a mitochondrial poison to disrupt metabolism prior to, or during imaging. The paralyzed worms were placed on the surface of a 5% noble agar pad then imaged without a coverslip using an epifluorescence–equipped Olympus BX51 upright compound microscope (Olympus, USA). The animals were imaged in the open air using a 10x objective and excited with filtered 445 nm light. The 483 nm and 542 nm emissions were recorded simultaneously, using a Dual View Simultaneous Image Splitter (Photometrics, AZ) and a Hamamatsu ImagEM Electron multiplier (EM) CCD camera. After the animals were imaged, they were immediately (~30 sec to 1 min) placed in a puddle of series 700 Halocarbon oil on a coverslip containing dried 2% agarose. The animals were placed on an inverted microscope and visualized using DIC optics and a dry 40x objective (0.75 n.a). Microinjection needles, filled with different concentrations of sterile KH_2PO_4 buffer (~pH 6.3 to 6.5), were fit onto a hydraulic micromanipulator, and the needle was then inserted through the cuticle and into one of the intestinal cells. An Eppendorf FemptoJet pump (Eppendorf, North America) was connected to the needle holder. The intestinal cells are connected to each other via cell-specific gap junctions [191], and thus we were able to observe the injected buffer move throughout the whole intestine. The total time that the worms were kept on the injection pad was no more than 20 seconds. The needle was inserted into the dorsal side of the hermaphrodite, generally between the anterior and mid-body region. The injector was set to deliver the Pi at maximum pressure. Generally, two to three seconds was required to fill the intestine. However, when the needle was removed, liquid could be seen to leak

from the intestinal puncture site. The approximate radius of the pre-injected hermaphrodite intestine was 40 microns and the approximate length was 850 microns. The amount of time required to fill the intestine was used to calculate the volume of the injected Pi buffer. Specifically, Pi buffer was injected into a puddle of halocarbon oil for the same amount of time then the diameter of the spherical aqueous droplet (~50 micrometers) was used to calculate the volume of buffer.

After the animals were injected, they were immediately (within 30 sec to 1 min) transferred to the 5% noble agar pad then reimaged in open air with the exact same microscope, camera and illumination settings used prior to the microinjection. The animals were imaged in open air because we found that putting a coverslip on the punctured animals at any time during the manipulations eventually caused them to explode. The data were analyzed using the Metamorph software (Molecular Devices, PA). The dimensions of the intestine were determined from micrographs of the injected hermaphrodites. The idealized volume of the intestine was estimated from the dimensions of the cylinder-shaped organ: $\pi r^2 h = (3.14)\,(40\text{x}10^{-4})^2(850\text{x}10^{-4})\,\text{cm}^3$. Assuming that the injected Pi fills the intestine, the maximum final concentration of Pi in the injected intestine would be 5.8 mM after the 50 mM injection, 11.7 mM after the 100 mM injection and 117 mM after the 1 M injection.

To monitor Pi injections in real time, 100 mM propidium iodide was added to the Pi buffer. The animals were immobilized on a dried 2% agar pad and covered with halocarbon oil. The animals were pierced with the needle and images for eCFP (445 ex/ 483 em), FRET (445 ex/ 542 em) and propidium iodide (561 ex/ 650 em) were captured

using the Olympus IX81 microscope, Yokogawa CSU-X1 Spinning Disk confocal unit, iXon897 EMCCD camera set-up. A 1-2 sec injection delivered an indeterminate bolus of Pi into the worm, and then images were taken every 4 sec for 30 sec. The propidium iodide was used to confirm the location of the injection and to estimate the spread of Pi buffer. ROIs used for data analysis were applied to the images approximately 50 to 100 μm from the needle puncture site. The data were analyzed using the Metamorph software.

CHAPTER III

QUANTITATIVE IMAGING OF FRET-BASED BIOSENSORS FOR CELL- AND ORGANELLE-SPECIFIC ANALYSES IN PLANTS †

3.1 Introduction

Genetically encoded FRET-based biosensors are powerful tools for monitoring changes in the concentrations of ions and metabolites in live cells. The ability to analyze such changes with high spatiotemporal resolution has revolutionized studies of myriad cellular processes including transport, compartmentalization, signaling and metabolism [146,154,192]. FRET biosensors for ions and small molecules consist of a ligand-binding domain fused to two spectral variants of GFP, usually CFP and YFP variants. Ligand binding to such biosensors induces a conformational change that alters FRET efficiency, which is detected as a change in fluorescence lifetime [157] or, more commonly, through a change in the ratio of the intensities of the two fluorescent proteins, i.e., FRET ratio. Consequently, fluorescence lifetime and FRET ratio both reflect the fraction of biosensors in each conformation. This fraction is directly proportional to ligand concentration over a range that is defined by the binding affinity and ultimately, saturation of the biosensor.

FRET-based biosensors have been used more widely in animal cell systems than in plants, but there is a growing list of biosensors that have been developed or

specifically adapted for use in plants that includes those for glucose, maltose, sucrose, glutamine, calcium, zinc, phosphate, and abscisic acid [144,146,151,154,192-194]. However, the successful application of FRET biosensors in plants has revealed a number of technical challenges. For example, RNA silencing severely limits expression and detection of some FRET biosensor transgenes [149]. This problem was resolved through the use of an alternative promoter [195], by limiting analyses to young seedlings [196,197], or by expressing the transgenes in RNA silencing mutants [149,151,196,198].

Pigments and other endogenous molecules that contribute to either autofluorescence or the quenching of biosensor fluorescence also pose a challenge for quantitative studies in plants [199]. Improvements in fluorescent proteins and in biosensor design, including the use of circularly permuted fluorescent proteins [160,195], have greatly increased both fluorescence intensities and dynamic range. Fluorescence quench, as well as variation in biosensor expression, can be partially resolved by using FRET sensitized emission, which accounts for donor spectral bleedthrough and acceptor cross excitation to determine the fraction of acceptor fluorescence that is derived from FRET [147,167,200]. These corrections may be unnecessary if analyses are restricted to single cells, but could be critical when investigating ligand concentrations in different cell types or when comparing results from multiple individuals to ascertain gene/protein functions.

Monitoring inorganic phosphate (Pi) in live plants is a particularly attractive application for FRET biosensors. The mechanisms underlying the systemic distribution of this essential nutrient are poorly understood yet cellular and subcellular

concentrations are expected to vary in response to both environmental and metabolic conditions [12,143,201-203]. Moreover, analytical methods that have been used previously to probe Pi contents of some plant cell compartments, such as nonaqueous fractionation and ^{31}P-NMR, lack cellular resolution [204-207]. Recently, a Pi biosensor was adapted that had been used previously in animal cells [150] for use in plants [151]. The second-generation Pi biosensors, cpFLIPPi, consist of a cyanobacterial Pi binding protein fused between eCFP (FRET donor) and a circularly permuted Venus (cpVenus) (FRET acceptor). Ratiometric analyses with one of these biosensors, cpFLIPPi-5.3m, revealed changes in cytosolic Pi concentrations in root epidermal cells in response to varied external supply, and also allowed detection of a mutation-induced change in Pi accumulation within plastids in root epidermal cells. In both cases, the analyses relied on comparisons of pooled FRET/donor data.

In this study, I aimed to expand and refine the previous work by defining quantitative FRET ratiometric imaging methods for different cell types and subcellular compartments, including those with pigments. Specifically, I used confocal microscopy to image the cpFLIPPi-5.3m Pi biosensor in the cytosol of root epidermal cells and in both the cytosol and chloroplast stroma of leaf mesophyll cells of *Arabidopsis thaliana.* The application of linear regression to donor, acceptor, and FRET-derived acceptor fluorescence intensities for each target location in the plant improved the precision of estimates for FRET sensitized emission correction coefficients and for FRET ratios obtained from images of multiple plants. The results also indicated that the FRET/eCFP ratio method is highly reproducible for the cytosol of both root and leaf cells, but is more

variable when applied to chloroplasts. I attributed the variation to quenching of donor eCFP fluorescence by pigments within this organelle, but regardless of mechanism, the variation was largely eliminated when the FRET/cpVenus ratio method was applied to the same samples. Consequently, FRET/cpVenus (FRET/acceptor) is the preferred ratiometric method for FRET biosensors localized to chloroplasts.

3.2 Results

3.2.1 Defined image acquisition for different cell types and subcellular compartments

An initial criterion for image capture optimization was to ensure that pixel intensities were well above background levels, yet also below saturation in each of the three images needed for ratiometric FRET analysis: eCFP (donor excitation and emission), FRET emission (donor excitation, acceptor emission), and direct cpVenus (acceptor excitation and emission). Another constraint was that for a given location in the plant, the same image capture settings were needed for eCFP and FRET emission to provide a quantitative measure of the ligand-dependent fluorescent outputs of the biosensor. The image capture variables for our confocal system included excitation laser intensity, exposure time, and camera sensitivity (EM gain and pre-amplifier gain). For convenience, I chose to use the same camera sensitivity settings for all experiments. In addition, because the EMCCD camera I used has a single detector, eCFP and FRET emission images were captured with equivalent sensitivity. However, it should be noted

that if a confocal system is used that employs two or more detectors then the spectral responses and sensitivities of each detector must be defined independently for each experimental condition [208]. I varied laser intensities and exposure times to yield mean pixel intensities that were approximately 10-fold greater than those for background fluorescence measured with the same settings. This signal-to-background ratio ensured that all measurements were within the linear range of the camera, which was necessary for quantitative measurements [209].

Images captured with optimized settings required processing before ratiometric analyses could be conducted. **Fig. 12** illustrates the image processing steps used in this study. First, background fluorescence was removed from raw images by subtracting mean pixel intensities obtained from images of the same locations in untransformed plants (**Fig. 12A**). A threshold was then manually applied to eCFP images to define the boundaries of the biosensor location (**Fig. 12B**). The eCFP images were chosen for this step because they consistently had the lowest pixel intensity value and would therefore provide the most conservative boundaries. To apply the same boundaries to the corresponding FRET emission and direct cpVenus images, the thresholded eCFP image was first converted to a masked binary image file (**Fig. 12B**). This step converted all of the fluorescence intensities above the threshold in the eCFP image to a value of one, and all intensities below the threshold to zero. The values for each pixel in the masked binary image were then multiplied to the corresponding pixel intensities in the background-subtracted eCFP, FRET emission and direct cpVenus images to yield final processed images (**Fig. 12C**). Regions of interest (ROIs) were applied to the processed images

(**Fig. 12C**), and mean pixel intensities for all pixels with intensities greater than zero within each ROI were recorded.

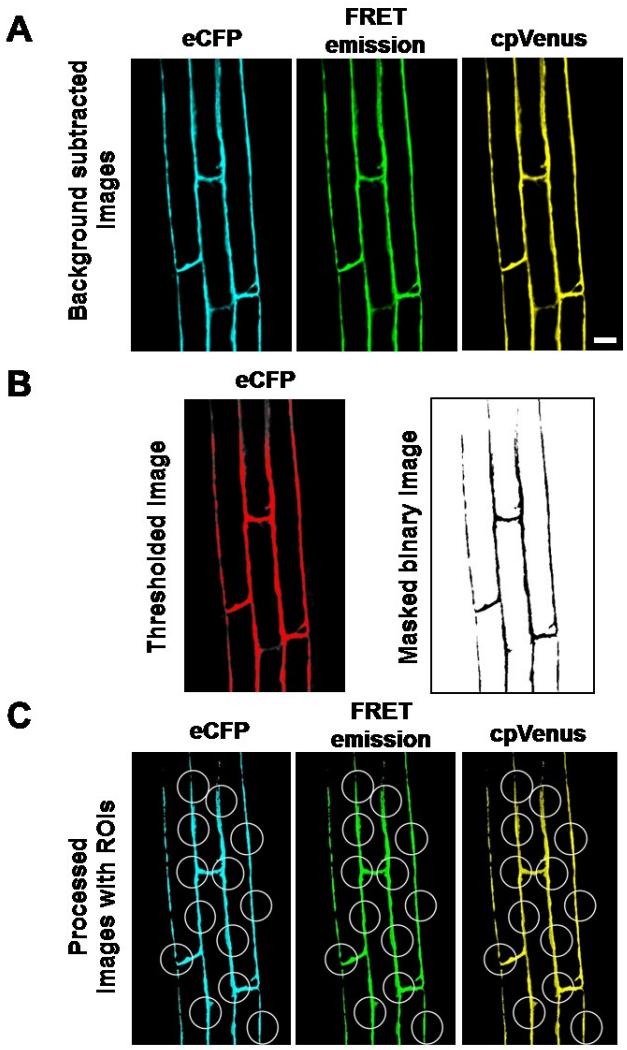

Figure 12. Stages of image processing. (A) Images for eCFP, FRET emission and direct cpVenus after background subtraction. (B) Threshold applied to an eCFP image and the masked binary image (black and white) created from the thresholded eCFP (C) Final processed eCFP, FRET emission, and cpVenus images. Regions of interest (ROIs) are drawn on the final images. Scale bar is 10 microns.

3.2.2 Location-specific spectral correction coefficients

I wanted to use FRET ratio as readout of relative Pi levels in different locations in the plant, but first needed to evaluate spectral factors that could influence ratio values. For example, donor bleedthrough (eCFP fluorescence that is detected in the cpVenus channel) and acceptor cross-excitation (direct excitation of cpVenus by the eCFP excitation laser) could vary with biosensor expression and/or cellular location [200,210]. I first assessed the extent that bleedthrough and cross-excitation varied with fluorescence intensity and then determined spectral correction coefficients that I could use to correct for their respective contributions to FRET emission in each of our target locations, i.e., to calculate FRET sensitized emission. From 6-8 independent plants expressing either eCFP (donor alone) or cpVenus (acceptor alone), I captured and processed eCFP, FRET emission, and direct cpVenus images for cytosol of root epidermal cells and for cytosol and chloroplast stroma of leaf palisade mesophyll cells. All images were captured using the same optimized settings used to image cpFLIPPi-5.3m. ROIs were applied to these images and mean pixel intensities were recorded.

Fluorescence intensity values varied up to 9-fold in some cases (**Fig. 13**). However, plots of eCFP bleedthrough versus eCFP, and of cpVenus cross-excitation versus direct cpVenus revealed that both bleedthrough (**Fig. 13A, C, E**) and cross-excitation **(Fig. 13B, D, F**) were directly proportional to fluorescence intensity over the entire range of intensities detected in each of the locations we examined. Consequently, I applied linear regression to data in each plot to yield a fitted line with a slope that represents a spectral correction coefficient. That is, slopes in **Fig. 13A, C**, and **E** are the

coefficients for correcting eCFP bleedthrough, and slopes in **Fig. 13B, D** and **F** are the coefficients for correcting acceptor cpVenus cross-excitation.

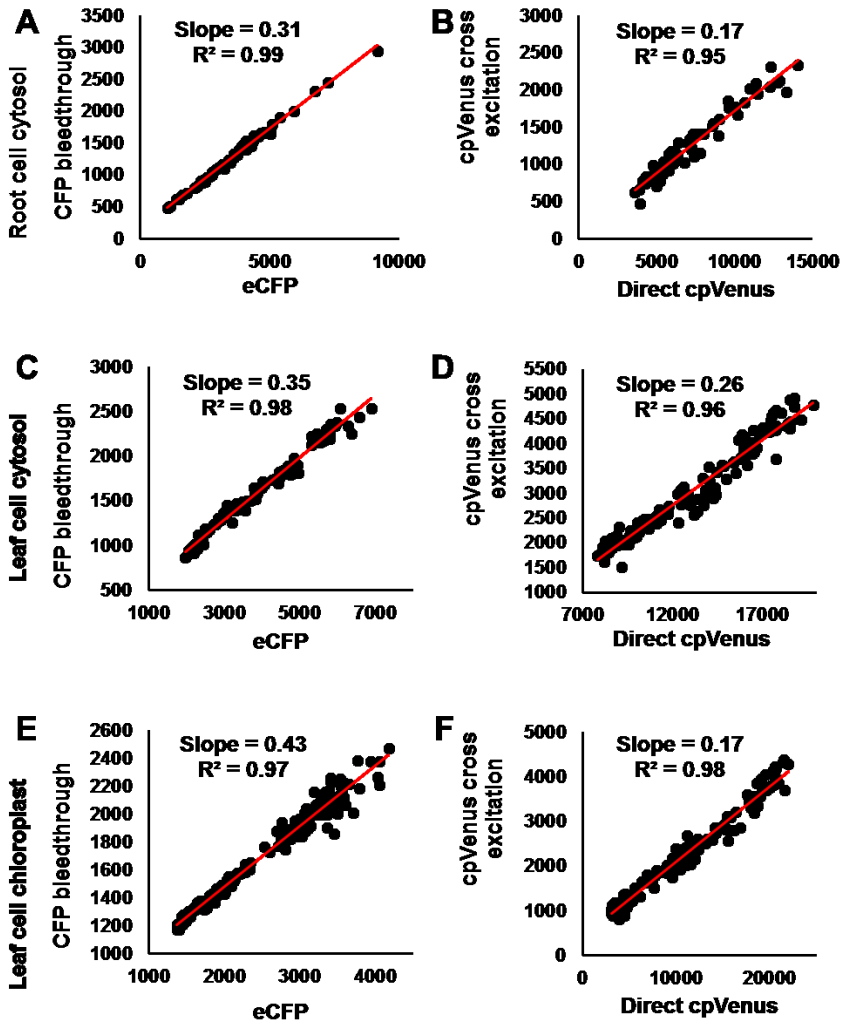

Figure 13. Determination of location-specific FRET correction coefficients. Mean intensity values obtained from 15 to 20 ROIs in FRET emission images from 6 to 8 independent plants are plotted against the corresponding intensity values from eCFP or direct cpVenus images. Slopes of the graphs represent correction coefficients for donor bleedthrough and acceptor cross-excitation that were used to calculate FRET sensitized emission.

Although donor bleedthrough and acceptor cross-excitation were uniformly proportional to fluorescence intensity within a given location in the plant, the corresponding correction coefficients differed between locations. I hypothesize that these differences reflect consistent differences in the chemical environments of each location, such as concentrations of pigments or other molecules that could influence, e.g., quench, the fluorescence of one or both of the fluorescent proteins. Regardless of the underlying mechanism, the results indicate that location-specific spectral correction coefficients must be defined to accurately assess biosensor FRET ratios in different cell compartments. Accordingly, all FRET emission data described hereafter were corrected using location-matched correction coefficients to yield FRET sensitized emission.

3.2.3 Ratiometric FRET analyses: FRET/donor versus FRET/acceptor

To systematically compare the efficacies of FRET/donor and FRET/acceptor approaches for different cellular locations I imaged plants expressing the cpFLIPPi-5.3m Pi biosensor using location-specific image capture settings and processed the images as described in **Fig. 12**. Then I used the corresponding location-specific spectral corrections coefficients (**Fig. 13**) to calculate FRET sensitized emission. I first compared the two FRET ratio analysis methods for the cytosol of root epidermal and leaf palisade mesophyll cells (**Fig. 14**). Pigments do not typically accumulate in the cytosol, but I could not know if pigments, particularly chlorophyll, present in other parts of the leaf would affect donor or acceptor fluorescence unequally. Fluorescence intensities varied by up to 5-fold in some cases, but plots of FRET emission versus eCFP (**Fig. 14A, C**)

and of FRET emission versus direct cpVenus (**Fig. 14B, D**) showed that FRET emission was directly proportional to both donor and acceptor emission in both cell types, as required for ratiometric analysis.

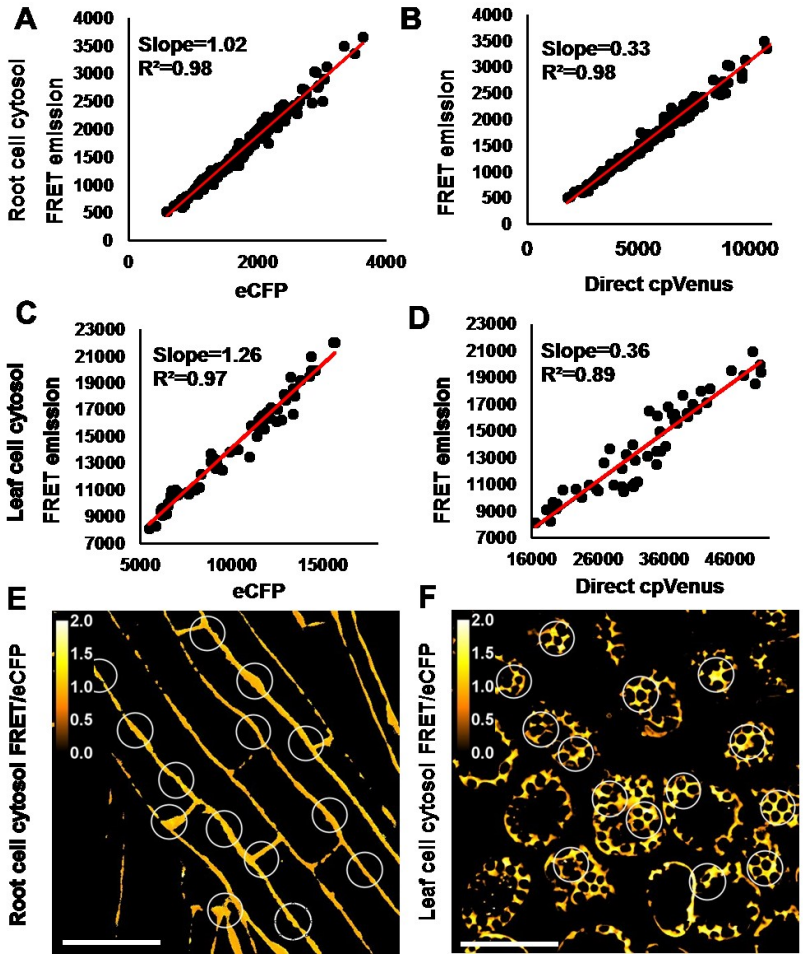

Figure 14. Ratiometric FRET analysis in cytosol. (A-D) Plots of FRET sensitized emission versus either eCFP or direct cpVenus mean intensity values. Trend lines were determined from linear regression. Each plot includes data from 6-8 independent plants.(E, F) Representative pseudo-colored FRET ratio images were generated by dividing FRET emission pixel intensity values by eCFP pixel intensity. Color bars indicate the range of FRET/eCFP ratios in the cytosol of root epidermal and leaf mesophyll cells. Scale bar is 50 microns**.**

Table 1. Comparison of FRET ratio analysis methods for different cellular and subcellular locations

Biosensor	Organ	Cell type	Subcellular location	FRET ratio method	FRET ratio from pooled ROIs (mean ± stdev, % relative error)	FRET ratio from linear regression (mean ± stdev, % relative error)
cpFLIPPi-5.3m	Root	Epidermis	Cytosol	FRET/eCFP	0.92 ± 0.06, 6.5	1.02 ± 0.02, 2.0
cpFLIPPi-5.3m	Root	Epidermis	Cytosol	FRET/cpVenus	0.29 ± 0.02, 6.9	0.32 ± 0.003, 0.9
cpFLIPPi-5.3m	Leaf	Mesophyll	Cytosol	FRET/eCFP	1.43 ± 0.09, 6.2	1.26 ± 0.03, 2.3
cpFLIPPi-5.3m	Leaf	Mesophyll	Cytosol	FRET/cpVenus	0.42 ± 0.04, 10.4	0.36 ± 0.02, 4.7
cpFLIPPi-5.3m	Leaf	Mesophyll	Chloroplast	FRET/eCFP	1.24 ± 0.24, 19.4	1.29 ± 0.09, 7.0
cpFLIPPi-5.3m	Leaf	Mesophyll	Chloroplast	FRET/cpVenus	0.61 ± 0.04, 6.6	0.60 ± 0.01, 1.7
cpFLIPPi-Null	Root	Epidermis	Cytosol	FRET/eCFP	0.65 ± 0.03, 3.8	0.72 ± 0.01, 1.6
cpFLIPPi-Null	Root	Epidermis	Cytosol	FRET/cpVenus	0.28 ± 0.01, 5.4	0.26 ± 0.007, 2.8
cpFLIPPi-Null	Leaf	Mesophyll	Cytosol	FRET/eCFP	0.87 ± 0.06, 7.3	0.90 ± 0.02, 2.4
cpFLIPPi-Null	Leaf	Mesophyll	Cytosol	FRET/cpVenus	0.49 ± 0.03, 7.0	0.50 ± 0.01, 2.4
cpFLIPPi-Null	Leaf	Mesophyll	Chloroplast	FRET/eCFP	0.85 ± 0.06, 7.3	0.91 ± 0.02, 2.4
cpFLIPPi-Null	Leaf	Mesophyll	Chloroplast	FRET/cpVenus	0.34 ± 0.03, 8.6	0.35 ± 0.01, 3.0

As with the derivation of spectral correction coefficients, FRET ratios could be calculated in two ways. One was to determine the desired FRET ratio for each ROI in a given location then calculate the pooled mean. Alternatively, linear regression could be

applied to the data in each plot, and the slope of the fitted line would represent FRET ratio for the population. I compared results from both of these calculation approaches as part of the comparison of FRET ratio methods. As shown in **Table 1**, relative errors for measurements of FRET/eCFP were consistently lower than those for FRET/cpVenus in the same cell type, and in all cases the relative errors for measurements obtained through linear regression were substantially lower than when using pooled values. I therefore conclude that FRET/eCFP (FRET/donor) is the preferred ratiometric method for the cytosol of both root and leaf cells, and that the use of linear regression provides a more precise estimate of FRET ratio for a population.

In contrast to our recommendation for the cytosol, FRET/acceptor rather than FRET/donor should be used when analyzing biosensors localized to chloroplasts. FRET emission was proportional to eCFP (**Fig. 15A**), but the data points were more widely scattered than those for cytosol (**Fig. 14**) and, as expected, the relative error was high even when linear regression was used (**Table 1**).

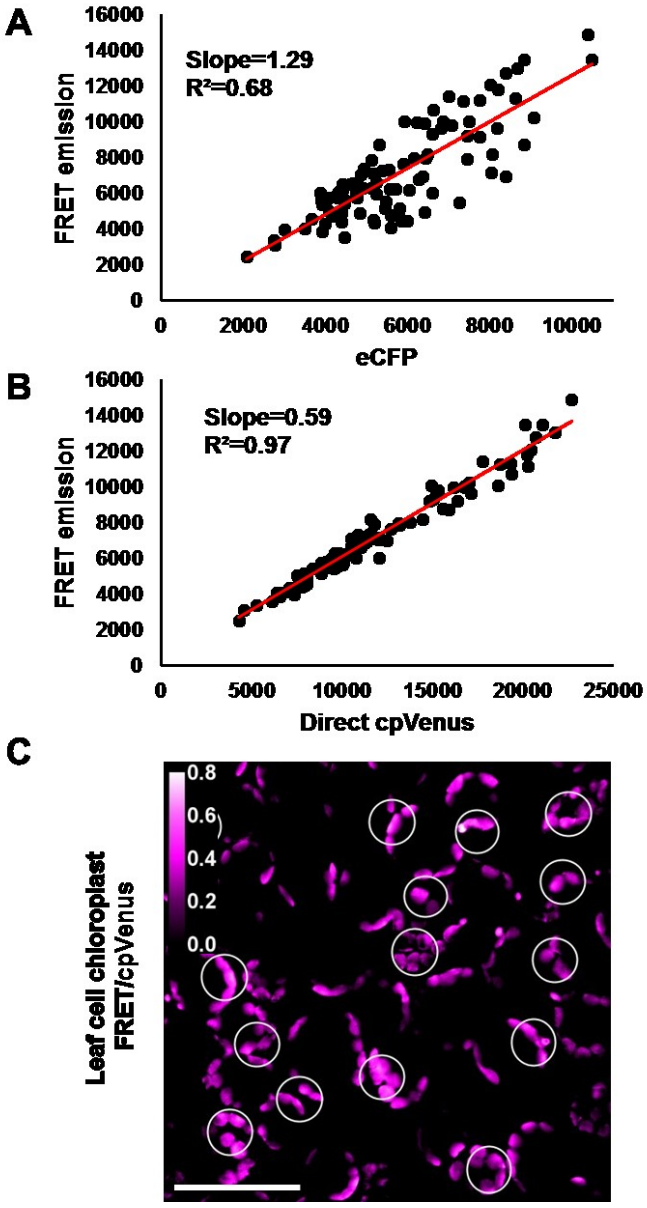

Figure 15. Ratiometric FRET analysis in chloroplasts. Plots of FRET sensitized emission versus eCFP (A) and direct cpVenus (B) mean intensity values obtained from 15 to 20 ROIs in each of 6 to 8 independent plants. Trend lines were determined from linear regression. Slopes represent fitted mean FRET ratios. (C,) Representative pseudo-colored FRET ratio images were generated by dividing FRET emission pixel intensity values by cpVenus pixel intensity values. Color bar indicates the range of FRET/cpVenus ratios in chloroplasts within leaf mesophyll cells. Scale bar is 50 microns.

It was possible that the variation in FRET/eCFP reflected heterogeneity of Pi concentrations between chloroplasts. However, this possibility was rejected because the variation was largely eliminated when we examined FRET/cpVenus (**Fig. 15B**) and the relative error was equivalent to those for measurements in the cytosol (**Table 1**). These results support my hypothesis that pigments or some other aspect of the local environment within chloroplasts affect eCFP and cpVenus unequally. Regardless of the basis for this effect it can be overcome by normalizing FRET emission values to cpVenus intensity. Although FRET/acceptor is less sensitive to changes in ligand concentration than FRET/donor because only the numerator is responsive to Pi concentration, the increase in precision (reduced relative error) is a desirable compromise that would facilitate detection of subtle changes in Pi concentrations.

3.2.4 Using a ligand-insensitive biosensor to distinguish nonspecific changes in FRET ratios

Even when FRET ratios are carefully defined a control is needed to distinguish what fraction of any observed differences are due to ligand-independent parameters, which could include pH and various ion concentrations, particularly chloride [211]. Differences in such nonspecific factors may be inherent or a consequence of experimental treatment. Previously a cpFLIPPi variant with high affinity for Pi was used as a control for nonspecific changes in FRET/eCFP ratios [151]. However, it was not certain that this biosensor variant would be saturated in all cellular contexts. I therefore isolated a Pi-insensitive variant, cpFLIPPi-Null, from a mutant library that was described

previously [151]. I confirmed that cpFLIPPi-Null was insensitive to Pi concentration using an *in vitro* binding assay in which cpFLIPPi-5.3m yielded the expected Pi-dependent decrease in FRET/eCFP ratio (**Fig. 16**).

As shown in **Fig. 16A**, cpFLIPPi-Null yielded lower FRET/eCFP ratio values than cpFLIPPi-5.3m even in the absence of Pi. This difference in absolute FRET ratio most likely reflects the relative orientations of the fluorophores [212], which is an unavoidable and largely arbitrary consequence of the small differences in protein sequences. However, normalization of FRET ratios allows direct comparisons between biosensor responses [213]. For example, the relative effects of Pi concentration on the two biosensors is shown in **Fig. 16B**. Importantly, this approach can also be applied to assess the effects of nonspecific factors on FRET ratio. For example, changes in pH and chloride concentration both affected FRET ratio, but the relative effects were equivalent for cpFLIPPi-5.3m and cpFLIPPi-Null (**Fig. 17**), indicating that cpFLIPPi-Null is a suitable control for distinguishing nonspecific changes in FRET ratio.

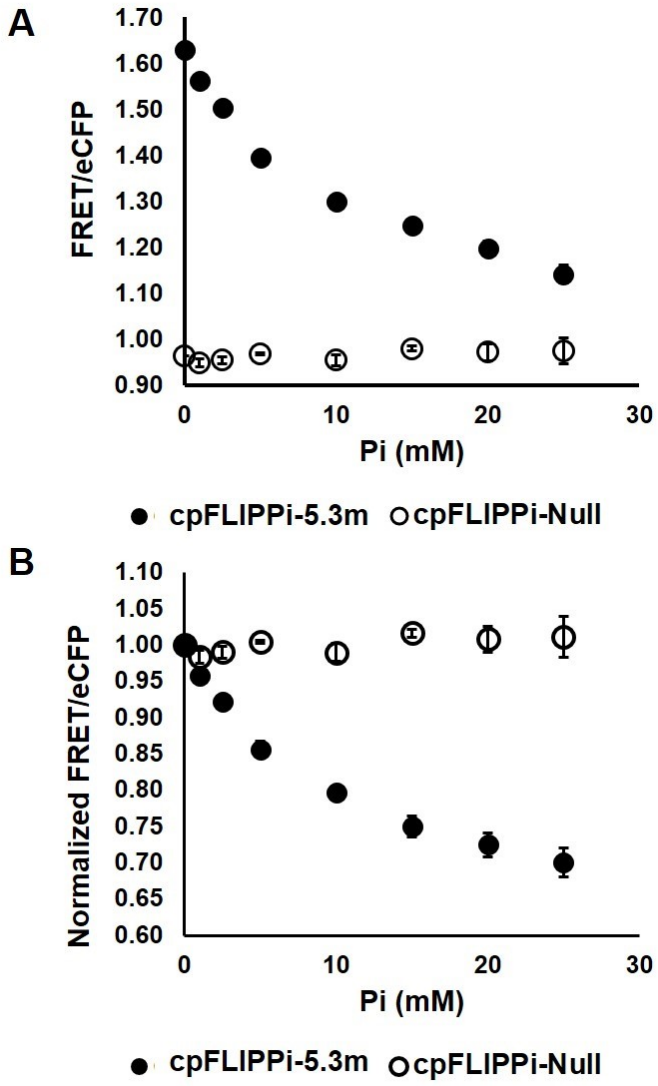

Figure 16. Comparisons of FRET/eCFP responses for cpFLIPPi-5.3m and cpFLIPPi-Null *in vitro.* (A) Effect of Pi concentration on FRET/eCFP ratios for purified cpFLIPPi-5.3m and cpFLIPPi-Null in an *in vitro* assay. Values shown are mean ± standard deviation for three replicates. (B) Effect of Pi concentration on normalized FRET/eCFP ratios from the same data shown in (A). Values were normalized to the FRET/eCFP ratio measured in the absence of Pi.

The cpFLIPPi-Null biosensor control was expressed in Arabidopsis plants and images were captured and processed for each target location exactly as described for cpFLIPPi-5.3m. FRET ratio values for each location (**Table 1**) were then used to distinguish Pi-specific from nonspecific changes in FRET ratios. For example, I wanted to know what fraction of the difference between FRET/eCFP ratio for cpFLIPPi-5.3m in the cytosol of leaf mesophyll (1.26) and root epidermis (1.02) was due to Pi concentration given that FRET/eCFP values for cpFLIPPi-Null also differed in these locations, 0.9 for mesophyll and 0.72 for root epidermis. To compare these differences I calculated relative changes for each biosensor. Specifically, FRET/eCFP ratio for cpFLIPPi-5.3m was 23.5% greater in the cytosol of leaf mesophyll than root epidermis, whereas cpFLIPPi-Null exhibited a 25% difference between the same locations suggesting that none of the difference observed with cpFLIPPi-5.3m could be attributed to Pi.

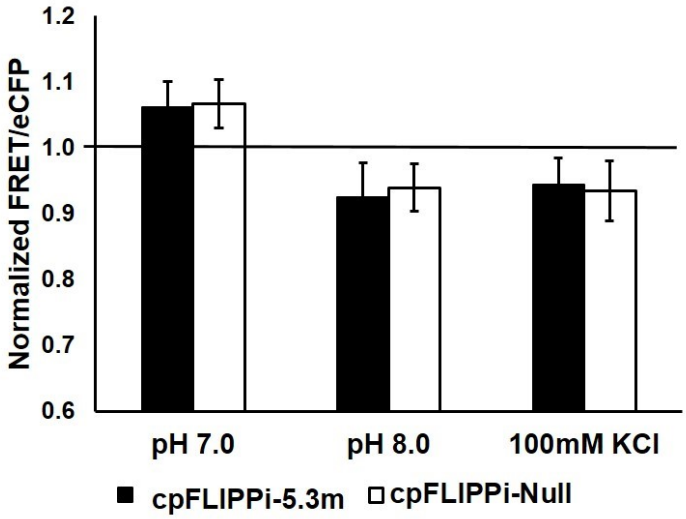

Figure 17. Effect of nonspecific factors on FRET/eCFP ratio for cpFLIPPi-5.3m and cpFLIPPi-Null. FRET/eCFP ratios were measured for purified biosensor proteins using an *in vitro* assay in which pH or KCl concentration was altered as indicated. Values were normalized to those obtained with the standard assay condition (pH 7.5, 0 mM KCl), which are indicated by the black line. Values shown are mean ± standard deviation for three replicates.

I also used cpFLIPPi-Null to evaluate changes in FRET ratio associated with experimental treatment. In this case, I examined the effect of Pi deprivation on FRET/eCFP ratio measured in the cytosol of root epidermal cells. Again, FRET ratios for both cpFLIPPi-5.3m and cpFLIPPi-Null increased (**Fig. 18**), which for cpFLIPPi-5.3m would be consistent with an expected decrease in Pi concentration. The FRET ratio for cpFLIPPi-5.3m increased 45%, whereas FRET ratio for cpFLIPPi-Null increased only 17%. Thus the 17% change observed for cpFLIPPi-Null represents nonspecific changes in the cytosol associated with the Pi deprivation treatment. Taking account of

this nonspecific effect, 28% of the change in the FRET/eCFP ratio for cpFLIPPi-5.3m can be attributed to a decrease in Pi concentration.

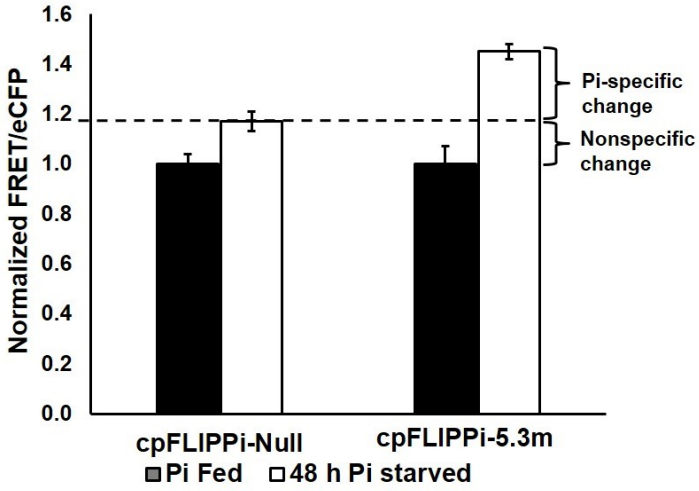

Figure 18. Effect of Pi deprivation on normalized FRET/eCFP ratios for the cytosol of root epidermal cells. Seedlings expressing cpFLIPPi-5.3m orcpFLIPPi-Null were maintained in Pi-fed growth conditions or deprived of Pi for 48 h prior to imaging. FRET/eCFP values from Pi-fed seedlings were used for normalization. Values shown are mean ±standard deviation forsix independent seedlings ($P < 0.001$, Student's *t* test).

3.3 Discussion

Pi is an essential nutrient with key structural and regulatory roles that impinge on nearly every facet of plant growth and metabolism [201,202]. However, our understanding of the mechanisms underlying Pi distribution and compartmentalization throughout the plant, as well as those required for the sensing and signaling of its availability [214,215], are limited by the inability to monitor Pi concentrations in

individual cells and subcellular compartments of live plants. Previously, Mukherjee *et al.* demonstrated that ratiometric imaging of a Pi biosensor could be used to detect changes in Pi concentrations within the cytosol and plastids of root epidermal cells [151]. In this study I expanded this approach to other cell types and subcellular compartments as a step toward holistic studies of Pi homeostasis.

Although optimal image capture settings must be determined empirically for every combination of biosensor, microscope, camera, and cellular location, I have described approaches to facilitate optimization of these parameters for quantitative analysis of genetically encoded FRET biosensors using confocal microscopy. It was not certain that the same imaging and/or analysis regimes could be applied to other cell types or organelles, particularly those that contain pigments. Indeed, fluorescence signals from the cpFLIPPi-5.3m Pi biosensor were much weaker in mature leaves than in seedling roots when the same imaging conditions were used. Therefore I optimized image capture settings for each of the target cellular and subcellular locations. Although my efforts focused on cpFLIPPi-5.3m, the overall strategy and associated considerations are broadly applicable to other FRET biosensors.

The image capture settings were carefully chosen considering the sensitivity of the detection system in order to maintain uniform fluorescent output. For example, direct cpVenus fluorescence reflects biosensor abundance rather than ligand concentration; therefore, arbitrary image capture settings could have been used provided that the pixel intensities fell within the linear range of the camera. However, I used settings that yielded mean pixel intensity values similar to those for eCFP and FRET emission

because this minimized any potential variations in detector sensitivity. This was an important consideration since direct cpVenus fluorescence was used to determine FRET sensitized emission values and, in some cases, was used to normalize FRET emission.

It was possible to calculate correction coefficients from the mean of pooled FRET ratio values (bleedthrough/eCFP and cross-excitation/direct cpVenus), but this would have been a source of error for subsequent ratiometric FRET analyses if one or both fluorescence responses had been nonlinear. In such an event, nonlinear regression would have been used to derive the coefficients. Alternatively, plugins for ImageJ are available to calculate nonlinear coefficients [216,217], but plotting intensity values from multiple individuals as described here provided a simple way to assess data variation within a population.

It should be noted that the use of linear regression to improve estimates of FRET ratio is limited to situations where a relatively wide distribution of fluorescence intensities exists, which is typical for analyses involving multiple plants. When fluorescence intensities are largely invariant, as might be expected when repeatedly imaging a single cell, then the use of linear regression would be unnecessary, and this conclusion would be supported through comparison of relative errors. For example, I found that FRET ratios within a field of view, as depicted in Figs. 3E, F and Fig. 4C, varied by less than 4%. Regardless of whether linear regression is used, plotting FRET emission versus donor or acceptor fluorescence would allow rapid evaluation of the population data set to identify individuals with attributes outside the population norm,

which may be particularly important when evaluating the effects of environmental conditions or pleiotropic mutations.

Although several ratiometric FRET analysis methods have been described [200,216], the FRET/donor ratio method is most commonly employed because it is highly sensitive to changes in ligand concentration. With this method, fluorescence intensities of the numerator and denominator components of the ratio both change in response to ligand concentration, and the changes are in opposite directions, thus yielding a large response. However, this study validates that FRET/acceptor ratio would be preferable when examining pigmented cells/cell compartments. One possible reason could be that pigments affect eCFP and cpVenus fluorescence unequally, primarily because chlorophyll absorbs light over a broad range (400-500 nm) that coincides with eCFP emission. As a result, eCFP fluorescence could be quenched. However, because FRET emission and acceptor both rely on output from cpVenus, any effects of pigments on its fluorescence would be proportional. Chlorophyll fluorescence occurs at wavelengths greater than 600 nm so would have a negligible effect on quantitation of either eCFP or cpVenus fluorescence.

Substitution of the eCFP and cpVenus components of the Pi biosensor with red-shifted fluorescent proteins that support FRET, i.e. green and red variants [218], would minimize the potential effects of chlorophyll and other pigments. However, such substitutions often require extensive optimization to attain fluorophore orientations suitable to detect ligand-dependent changes in FRET [199,212,219]. Until such

biosensors are available, the methods described here for blue-yellow FRET pairs remain broadly applicable.

It must be emphasized that the ratiometric approaches that I have described report relative changes in ligand concentration. Calibration must be established to define absolute ligand concentrations. Ideally, calibrations would involve direct manipulation of ligand concentrations in the target location, e.g., via microinjection, but this is technically challenging and may not be achievable for some subcellular compartments. Alternative approaches include in situ calibrations, which can be conducted when the ligand and/or chelators readily diffuse across cell membranes, and in vitro calibrations using purified proteins suspended in solutions that mimic the target cell compartment as closely as possible. The continued development of calibration strategies will be needed to enable broad comparisons of results with FRET biosensors.

3.4 Materials And Methods

3.4.1 Plasmids

Plasmids for expression of cpFLIPPi-5.3m in bacteria and in plants were described previously [151]. The cpFLIPPi-Null biosensor is a derivative of cpFLIPPi-5.3m in which a portion of the Pi binding domain has been altered from GAGAAF to ISGSTS. The cpFLIPPi-5.3m and cpFLIPPi-Null transgenes were cloned in pRSET for expression in *E. coli* and in the pCN-UBQ10 plasmid [151] for expression in

Arabidopsis. Plastid-targeted variants of each sensor were constructed by inserting a 237-bp fragment encoding the 79-amino acid RbcS chloroplast transit peptide [220] in frame at the 5' end of the sensor genes.

3.4.2 In vitro Pi binding assays

The pRSET cpFLIPPi clones were introduced into *E. coli* BL21 (DE3) bacteria and single colonies were cultured overnight in 100 mL of Luria Bertani medium. The cells were harvested by centrifugation and then lysed using Bug Buster protein extraction reagents (EMD Millipore). The expressed sensor proteins were purified from cell lysates using His-affinity chromatography with elution in 20 mM Tris-HCl, pH 7.5, 150 mM K-gluconate, and 400 mM imidazole. The eluent was dialyzed overnight at 4°C against 20 mM Tris-HCl, pH 7.5, then stored at 4°C. Protein concentration was quantified using the Bradford colorimetric assay and samples were diluted in protein dilution buffer: 100 mM K-gluconate, 30 mM NaCl, 25 mM MES, 25 mM HEPES, 40% (w/v) sucrose, pH 7.5. The protein solution was mixed with varied amounts of Pi, and the fluorescence was measured using a Synergy HT plate reader with excitation at 420/27 nm and emission at both 485/20 nm (eCFP) and 540/25 nm (FRET-derived cpVenus). Excitation at 500/20 nm was used for direct excitation of cpVenus.

3.4.3 Generation of transgenic Arabidopsis plants

Cytosol- or plastid-targeted biosensor clones were introduced into *Agrobacterium tumefaciens* strain GV3101, and the resulting strains were used to

transform Arabidopsis via the floral dip procedure [221]. Transgenic plants were selected on agar medium containing 10 μM phosphinothricin. At least ten independent lines for each construct were examined for fluorescence and progeny from a representative line that maintained uniform fluorescence in the T2 generation were used for all subsequent studies.

3.4.4 Live imaging of roots and leaves

For analysis of roots, Arabidopsis seeds were germinated and grown in 96-well microplates with 230 μL of 0.5x Murashige and Skoog medium [222] containing 0.25% (w/v) sucrose and 250 μM Pi in a growth chamber (60% relative humidity, 21°C, and 90 μmol m^{-2} s^{-1} light intensity for a 16 h photoperiod.). After 5 days the seedlings were transferred to fresh medium containing either 250 μM Pi (Pi replete) or 10 μM Pi (Pi deficient). The media were replaced every 24 h. After 48 h seedlings were mounted in their respective growth medium on a cover glass, they were gently covered with a small cover glass to keep the roots flat when imaged using an inverted Olympus IX81 microscope equipped with a Yokogawa CSU-X1 Spinning Disk confocal unit and an iXon3 897 EMCCD camera (Andor Technology, USA). The same camera settings for EM gain (5%) and pre-amplifier gain (2.4%) were used for all experiments. Plants were imaged using a 40x (numerical aperture 1.3) oil immersion objective. Comparable results were obtained in trial experiments using a 60x (numerical aperture 1.2) water immersion objective provided that all control images were captured with the same objective. A 445 nm laser was used to excite eCFP. A 483/32 nm filter was used to

detect eCFP emission, and a 542/27 nm filter was used to detect FRET-derived cpVenus emission (FRET emission) and emission from directly excited cpVenus. A 515 nm laser was used for direct excitation of cpVenus.

For analysis of leaves, Arabidopsis plants were grown in soil for four weeks in a growth chamber with same environmental conditions described above. The 5th rosette leaf was detached and immediately placed adaxial surface down in a custom made chamber (http:// microscopy.tamu.edu/lab-protocols/light-microscopy-protocols.html). The leaf was treated with perfluorodecalin to rapidly infiltrate intercellular air spaces and thereby improve optical qualities of the leaf [223]. This treatment had no measurable effect on biosensor fluorescence or FRET compared to water-mounted leaves. The leaf was gently covered with a small glass brick to keep the specimen flat against the cover glass. Palisade mesophyll cells were imaged using a 40x objective as described above. Untransformed plants were imaged using the same image acquisition setting to determine background fluorescence values.

3.4.5 Image processing and ratiometric FRET analysis

Images were processed and analyzed using Metamorph and ImageJ software. Background fluorescence values (mean pixel intensities) for each combination of excitation and emission were determined for each target location in plants from images of 5-10 cells in 3-5 untransformed plants. The mean background values for each emission channel were subtracted from the corresponding images of transgenic plants prior to further processing. Metamorph software was used to align the pixels for each

emission channel to ensure that they were in register. A threshold was applied to each eCFP image because in all cases it had lower pixel intensities than the corresponding FRET emission and cpVenus images and thus specified the most restrictive boundary for the target location. A masked binary file was then created from the eCFP thresholded image. This binary file was multiplied to each of the three background-subtracted images for eCFP, FRET emission and direct cpVenus, respectively. Regions of interest (ROIs) were applied to the eCFP image and mean intensity values for each ROI were recorded. The same ROIs were propagated to the FRET emission and direct cpVenus images, and mean intensities were recorded.

The FRET emission intensity values were corrected for donor spectral bleedthrough and acceptor cross excitation to yield sensitized FRET emission values. Correction coefficients for spectral bleedthrough and cross excitation were determined for each target cell compartment from images of plants expressing a single fluorescent protein (eCFP or cpVenus) using the same image acquisition settings used for biosensor imaging. Mean intensity values for ROIs applied to FRET emission images were plotted against the corresponding eCFP and direct cpVenus values. Linear regression using the LINEST function of Microsoft Excel™ v15.0 was applied to the data. The slopes of the fitted straight lines from FRET emission versus eCFP, and FRET emission versus direct cpVenus represent the donor spectral bleedthrough and acceptor cross excitation correction coefficients, respectively. Sensitized FRET was calculated for each FRET emission ROI using the following equation: Sensitized FRET= Raw FRET – (eCFP

emission * a) – (cpVenus emission* b), where a and b represent the donor spectral bleedthrough and acceptor cross excitation factors, respectively.

Sensitized FRET/eCFP and sensitized FRET/cpVenus FRET ratios were calculated for each ROI then pooled to calculate mean values. Alternatively, sensitized FRET emission intensity values for all ROIs in a given cellular location were plotted separately against all of the corresponding eCFP and direct cpVenus intensity values then linear regression using the LINEST function of Microsoft Excel™ v15.0 was applied to the data. The slopes of the lines from these plots represent the fitted FRET/eCFP and fitted FRET/cpVenus ratio, respectively.

CHAPTER IV

HIGH-RESOLUTION CYTOSOLIC PHOSPHATE DISTRIBUTION PATTERN IN THE DEVELOPMENTAL ZONES OF ARABIDOPSIS ROOT

4.1 Introduction

Inorganic phosphate (Pi) is an essential macronutrient. It is a component of major macromolecules such as phospholipids and nucleic acids, and has key roles in cellular signal transduction and energy conversion processes. Maintaining appropriate Pi concentrations within each subcellular compartment is therefore critical for plant growth and physiological processes such as photosynthesis and carbon metabolism. However, soils often contain scarce amounts of available Pi, and it is poorly diffusible in soil [7]. Plants need to maintain cellular Pi in the millimolar range, whereas available Pi in soil is in the micromolar range [8]. Although Pi scarcity can be circumvented by supplying plants with Pi fertilizers, the main source of Pi fertilizers is finite rock reserves that are being depleted rapidly [224]. Consequently, rational approaches to the breeding and engineering of plants for increased efficiency of Pi uptake and utilization are urgently needed to meet the growing demands for plant-derived food, fiber, and fuel [225].

Plants have evolved mechanisms to cope with Pi deficiency such as modifying root architecture to maximize surface area, enhancing the expression of Pi transporters, and secreting acid phosphatases to solubilize organic phosphates [12,15,82,83,93,226]. Plants have also developed methods to utilize Pi efficiently. For example, when Pi supply is low, plants can bypass Pi-dependent steps in respiratory pathways [41],

substitute membrane phospholipids with sulfo- and galacto-lipids [227,228], redistribute Pi from shoot to root [6], release Pi from vacuolar stores, and recycle Pi from organic phospho-compounds [23]. Moreover, low Pi stress induces the expression of high affinity Pi transporters to enhance Pi acquisition. High affinity H^+/Pi cotransporters on the plasma membrane that constitute the Phosphate Transporter 1 (PHT1) family facilitate Pi uptake from the soil. In Arabidopsis there are nine PHT1 transporters (PHT1;1 to PHT1;9), and these are expressed mainly in epidermal and cortical cells of the root. Loss of function mutations of PHT1 genes (*pht1;1*, *pht1;4*) leads to slower and reduced root growth, which ultimately affects the overall growth and development of the plants [15,20,24,229].

Several studies have characterized the distribution pattern of Pi transporters at the root-soil interface, as well as the root architectural modifications to maximize Pi acquisition. However, little is known of the distribution and compartmentalization of Pi within the root. Specialized analytical methods are needed to measure Pi concentrations in live plants with high spatial and temporal resolution. Previous studies demonstrated that a genetically encoded Pi sensor, cpFLIPPi, could resolve relative differences in Pi levels within cytosol and plastids [150,151,230]. Mukherjee *et al.* used a cpFLIPPi sensor to detect responses of mature root cells to Pi deprivation and to subsequent replenishment. In this work, I have used the cpFLIPPi sensor to measure cytosolic Pi distribution in the five developmental zones of the root.

The root is the first organ to receive Pi from the surrounding environment and it mediates distribution of Pi to the source and sink tissues. Anatomically, the root can be

divided into distinct developmental zones starting from the root tip, namely the meristematic zone (MZ), transition zone (TZ), elongation zone (EZ), differentiation zone (DZ), and mature root zone (MR) based on cell size and activity [62,231]. In this work, I quantified cytosolic Pi concentrations in the root developmental zones. I also described the correlation between cytosolic Pi concentration and zone-specific cellular activities such as cell proliferation and cell expansion.

4.2 Results:

4.2.1 In vivo calibration of Pi-FRET sensor

In order to determine the cytosolic Pi concentration of the root cells I first needed to convert FRET ratios to millimolar Pi by referencing an *in vivo* Pi-response calibration of the sensor. Previous studies described *in vitro* calibration of FRET-based sensors using buffers designed to mimic the chemical composition of the cytosol [150,151]. However, a cell's chemical environment can influence fluorescence of the FRET donor and acceptor making it difficult to replicate the FRET ratios in an *in vitro* system. Therefore, *in vivo* FRET ratios can not be directly cross referenced to an *in vitro* Pi binding curve to determine cellular Pi concentrations. To circumvent this limitation I used microinjection to introduce solutions of different Pi concentrations directly into the cytosol. The injection buffer (pH 7.3) also included mRuby2 as a marker. Because injecion often displaced much of the internal sensor protein out of the focal plane I included 1 μM purified Pi sensor in the injection buffer mix to ensure that sufficient

amounts of the sensor remained in the focal plane for imaging (**Fig. 19A**). I measured the cytosolic FRET/eCFP ratio of each injected cell (**Fig. 19B**) and prepared a Pi calibration using the average FRET/eCFP ratios from cells injected with eight different concentrations of Pi. I used a single site binding equation to estimate the binding affinity of the sensor (K_d= 7.4 mM) (**Fig. 19C**) and thereafter converted FRET/eCFP ratios for all subsequent experiments to millimolar concentrations by referencing the calibration.

FRET/eCFP ratio of an injected cell would reflect a combination of injected Pi and pre-exsiting cytosolic Pi. To minimize the effect of existing Pi concentrations on my measurements I injected 20 to 25 pL of injection solution, which is 4 to 5 times greater than the average volume of cytosol in a typical transition zone cell (5 pL), as determined from confocal micrographs. Consequently, excess Pi buffer flowed to adjacent cells through the plasmodesmata, as evident from the altered FRET/eCFP ratio of the adjacent cells (**Fig. 20**). However**,** the mRuby2 marker remained confined within the injected cell because it is too large to traverse plasmadesmata. Injecting with excess Pi buffer ensured maximal displacement of pre-existing cytosolic Pi from the injected cell to the adjacent symplastically connected cells of the TZ-EZ [77]. However, the FRET ratios of the injected cells eventually reset to the uninjected values due to redistribution of Pi. **Fig. 20** shows 75% recovery of FRET/eCFP 5 min after injection. Therefore, injected cells were imaged within 1.5 s to maximize accuracy.

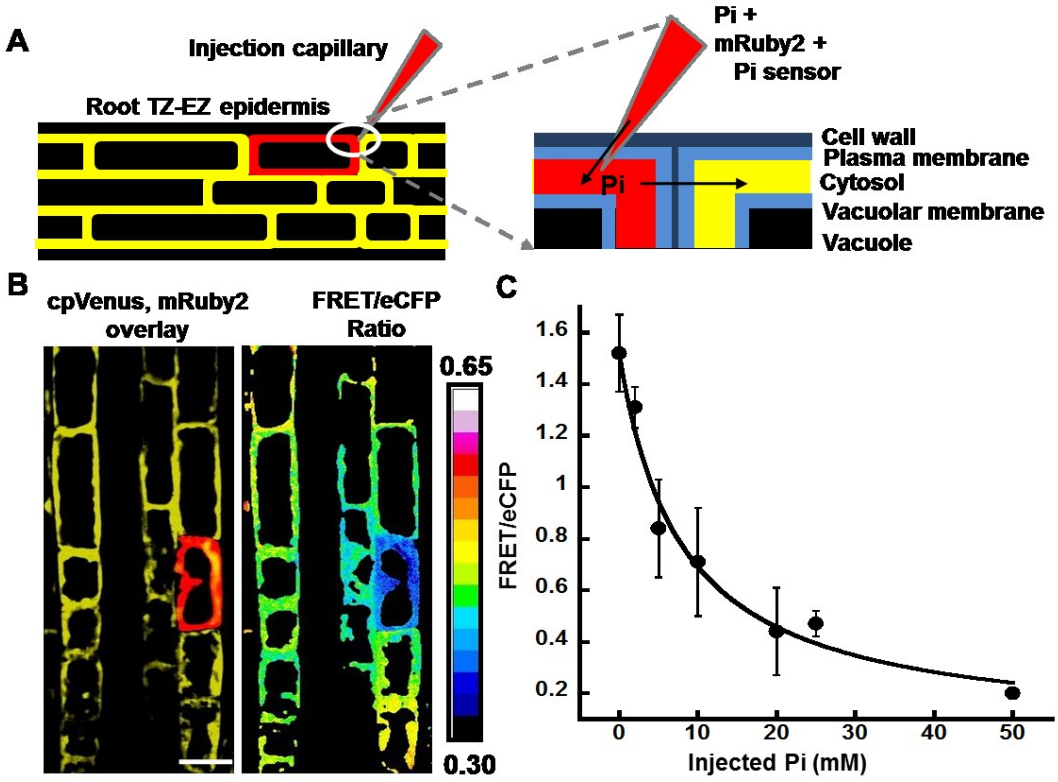

Figure 19. *In vivo* calibration of a cpFLIPPi sensor. (A) Schematic representation of microinjecting an epidermal cell of the transition-elongation zone. Red color (mRuby2) demarcates the spread of injection solution within the cell. Inset shows the capillary having penetrated the cell membrane and injecting Pi into the cytosol along with mRuby2 marker and purified Pi sensor. The mRuby2 and cpFLIPPi proteins remain Figure 19 continued: within the injected cell; however, Pi diffuses to the adjacent cell via plasmodesmata. (B) Fluorescent micrograph (cpVenus emission channel merged with mRuby2 emission channel) and FRET/eCFP ratio image of the root after Pi injection. The FRET/eCFP ratio image is created by dividing the pixel intensities of the image from FRET-cpVenus emission channel by the pixel intensities of the image from the eCFP emission channel. The color scale represents FRET/eCFP ratios. The injected cell shows mRuby2 fluorescence and altered FRET/eCFP ratio compared to adjacent cells. Scale bar is 20 micron. (C) Plot represents *in vivo* calibration of cpFLIPPi sensor derived from FRET/eCFP ratios of injected cells. Plotted values represent mean FRET/eCFP ratios with standard deviation obtained from 6-8 individual cells.

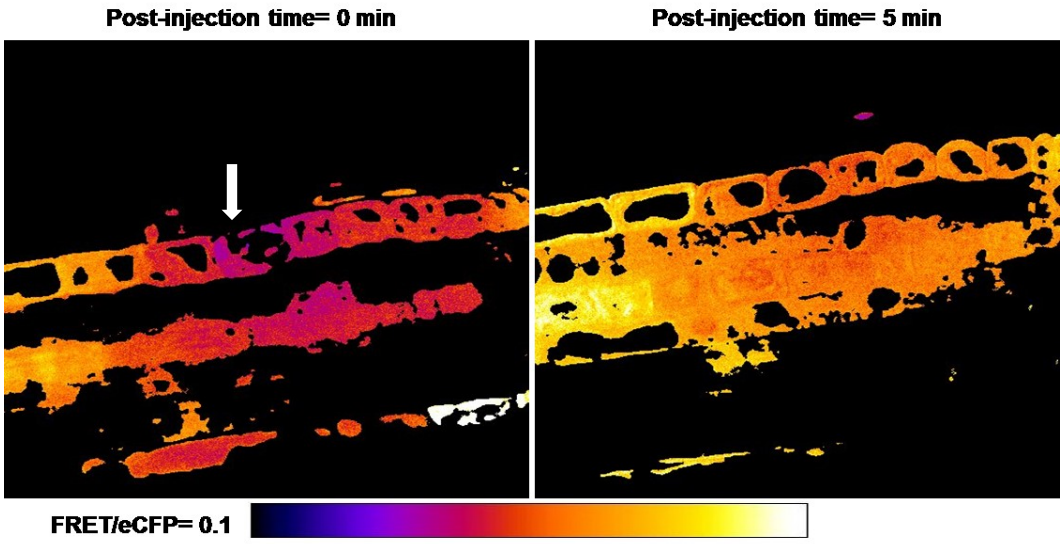

Figure 20. Change in FRET/eCFP ratio after Pi injection and after a recovery time. Micrographs show the change in FRET/eCFP ratio of injected and adjacent cells after 50 mM Pi injection. The ratio resets to 75% of pre-injected values 5 min after injection.

4.2.2 The root shows a developmental zone specific cytosolic Pi pattern

To explore the dynamics of Pi mobilization within the root, I wanted to first establish a high-resolution map of Pi concentrations in the different cells and developmental zones of the root, including the MZ, TZ, EZ, DZ and MR (**Fig. 21A-E**). Previous reports indicated that the apical zones of the root (MZ, TZ and EZ) are symplastically connected by plasmodesmata. The epidermal cells become symplastically isolated beyond the EZ, where the first trichoblast cell appears in the DZ [77]. I hypothesized that the root will have similar cytosolic Pi levels in the sympastically connected zones. To test this hypothesis I imaged cells throughout the length of the root and measured FRET/eCFP ratios (**Fig. 21F-J**).

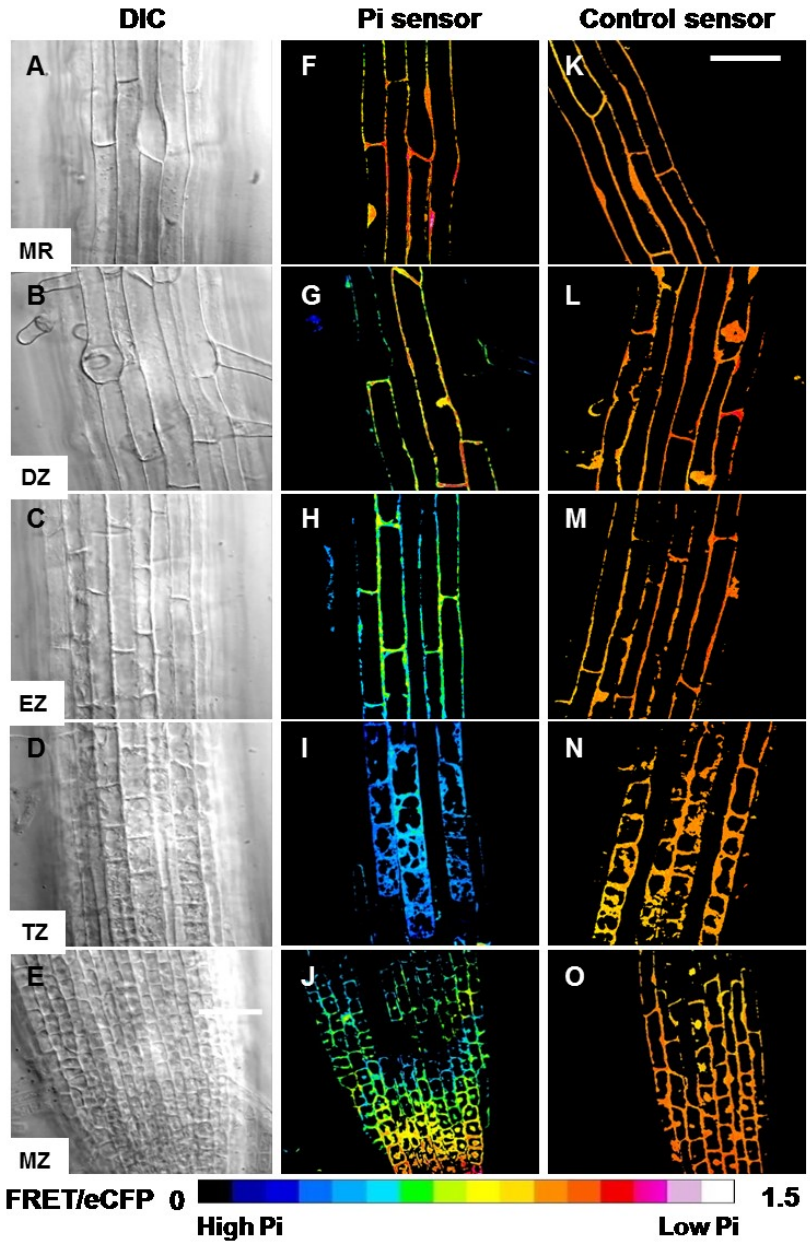

Figure 21. FRET/eCFP ratios vary in the five developmental zones of a root. DIC (A-E) and FRET/eCFP ratio micrographs (F-O) of the five developmental zones of the root; MZ: Meristematic zone, TZ: Transition zone, EZ: Elongation zone, DZ: Differentiation zone; MR: Mature root zone. Scale bar is 50 microns.

FRET/eCFP ratios varied in the root apex; the TZ had the lowest FRET/eCFP (highest Pi) and the MR had the highest ratio (lowest Pi). FRET/eCFP ratios from plants expressing the control, non-responsive sensor, cpFLIPPi-Null, did not differ significantly in the five zones. I therefore conlcude that the varied pattern of FRET/eCFP ratio in the root is Pi specific (**Fig. 21K-O**).

After conducting an initial survey through the root epidermis, I quantified cytosolic Pi concentrations in the root epidermis, cortex, and endodermis by cross referencing FRET/eCFP ratios to the *in vivo* calibration curve. The results indicated that the zone-specific Pi pattern exists in the epidermis, cortex, and at least part of the endodermis of the root (**Fig. 22A-C**). Pi concentrations through the entire endodermis could not be measured because the Pi sensor was not expressed in the apical zones' endodermis from either the UBQ10 or 35S promoters (**Fig. 23**). Nevertheless, I speculate that the endodermis possesses a similar Pi pattern as the epidermis and cortex. The existance of distinct cytosolic Pi levels in the five developmental zones despite the symplastic connections suggests that specific cellular activities maintain this Pi pattern.

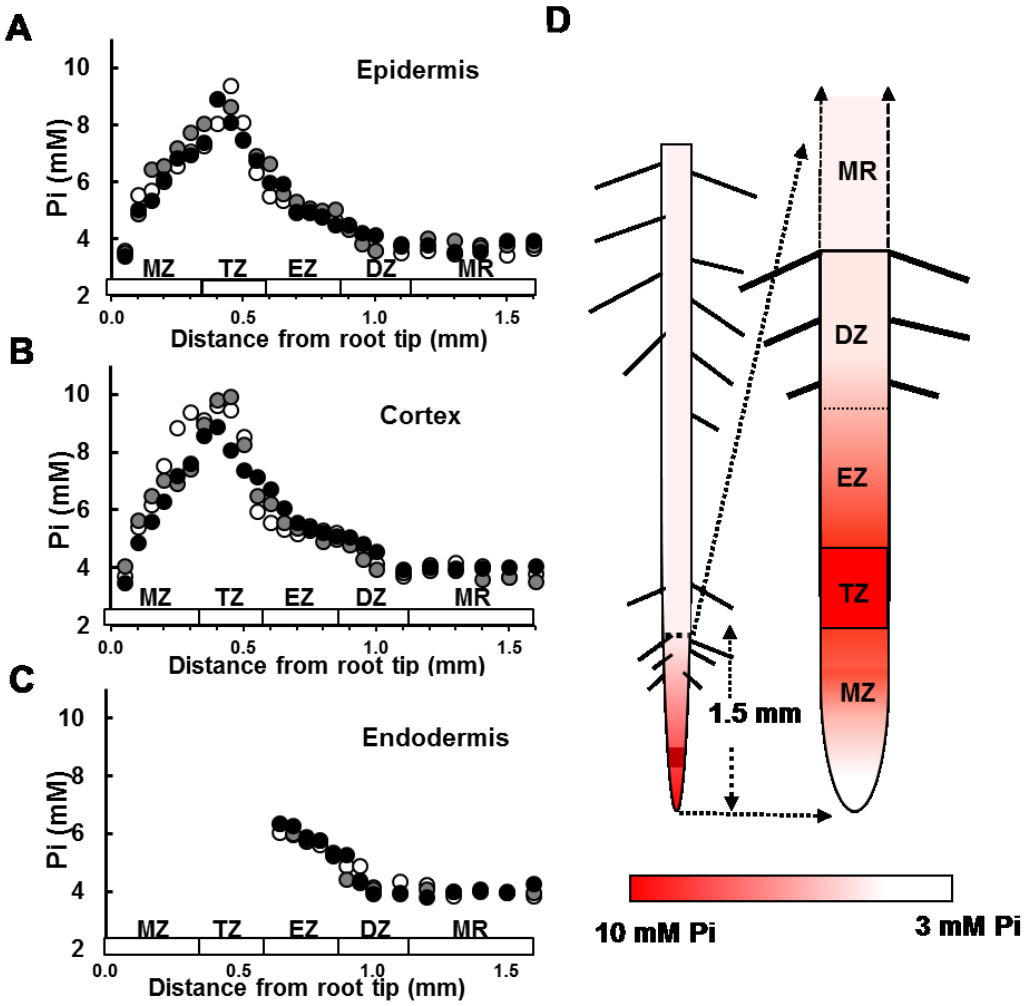

Figure 22. Cytosolic Pi of the epidermal, cortical and endodermal cells of the root are equivalent and Pi specific. Plots represent cytosolic Pi of (A) epidermal, (B) cortical and (C) endodermal cells of three individual roots. (D) Schematic representation of Pi concentrations (mM) in the root. Inset shows relative cytosolic Pi levels in the five developmental zones.

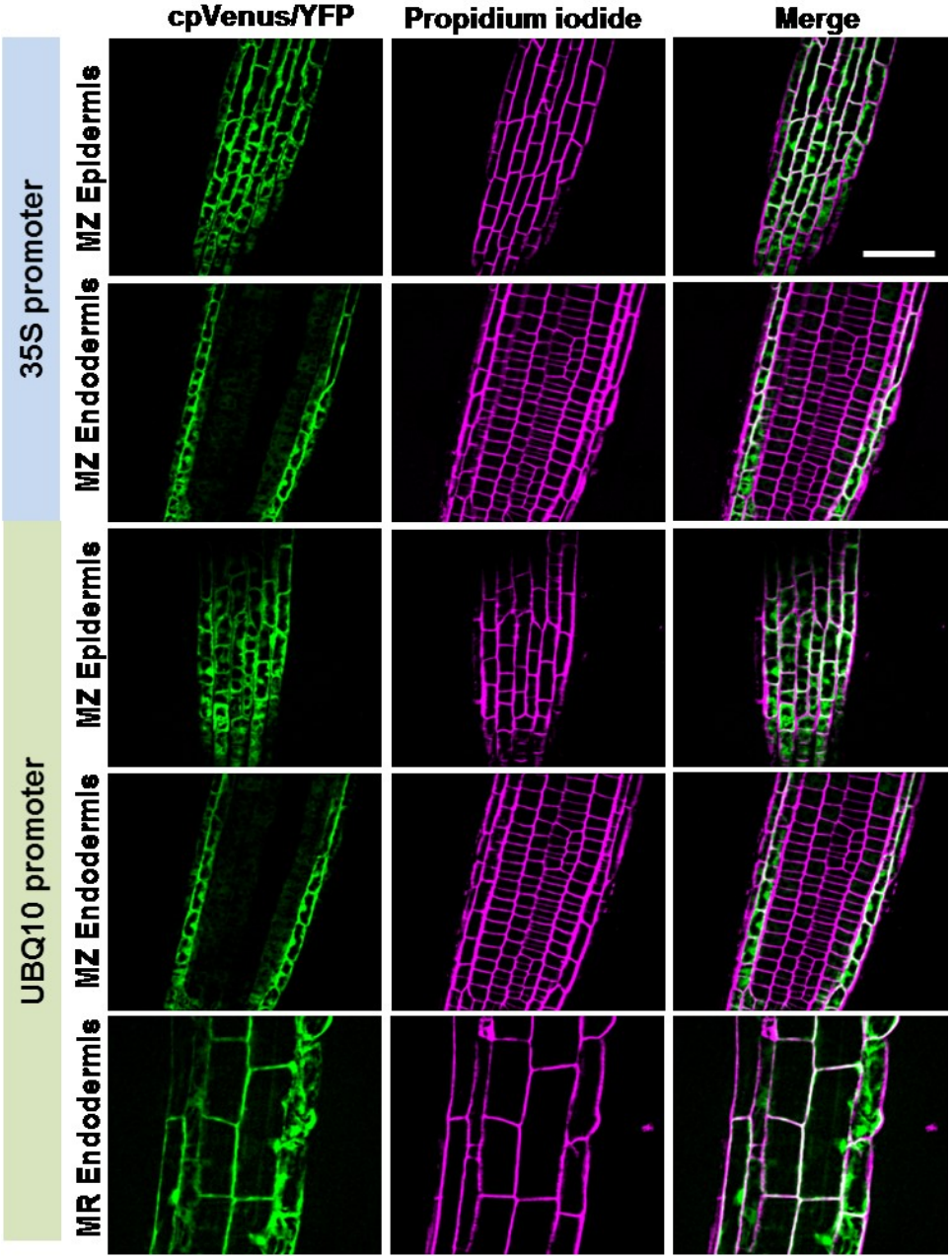

Figure 23. Expression of cpFLIPPi sensor driven by UBQ10 and 35S promoter in the root cells. Fluorescent images show the expression of cpFLIPPi sensor in the epidermis of the root meristem by both UBQ10 and 35S promoter; however no expression is seen in the endodermis of the root meristem by both promoters. Propidium iodide demarcates the cell wall.

4.2.3 The zone-specific Pi distribution is independent of external Pi

I asked whether the greater accumulation of Pi in the TZ is driven by Pi uptake from the medium. I first held 6 day old plants in medium without Pi for 48 h then measured Pi in the root zones (**Fig. 24A**). After 48 h of Pi depirvation cytosolic Pi decreased in all of the zones as expected; however, the relative distribution pattern was preserved with highest Pi levels in the TZ. I next tested whether cytosolic Pi in MZ, EZ, DZ and MR cells can be augmented to match that in the TZ by supplying excess Pi to the plants [151]. I grew plants in 0.25 mM, 0.5 mM, 1 mM, and 2 mM Pi, and then measured cytosolic Pi in the root zones (**Fig. 24B**). I found that the zone-specific Pi pattern was mainatined despite an eight-fold increase in external Pi. These results demonstrated that the root Pi distribution pattern is independent of external Pi and it is maintianed by internal mechanisms.

4.2.4 The zone-specific Pi distribution pattern is maintained throughout development

I wanted to determine whether the Pi distribution pattern is maintained as the plant develops. I used hydroponically grown 6 d old seedlings for most experiments, but in this case I examined plants grown in MS agar plates for 3 weeks. These plants had 9 to 10 true leaves and the roots were 10 cm long. Interestingly, the mature plants exhibited the same zone-specific Pi pattern in both primary and secondary roots (**Fig. 25**). These results confirmed that the zone-specific cytsolic Pi distribution pattern is maintained throughout the life cycle of the plant.

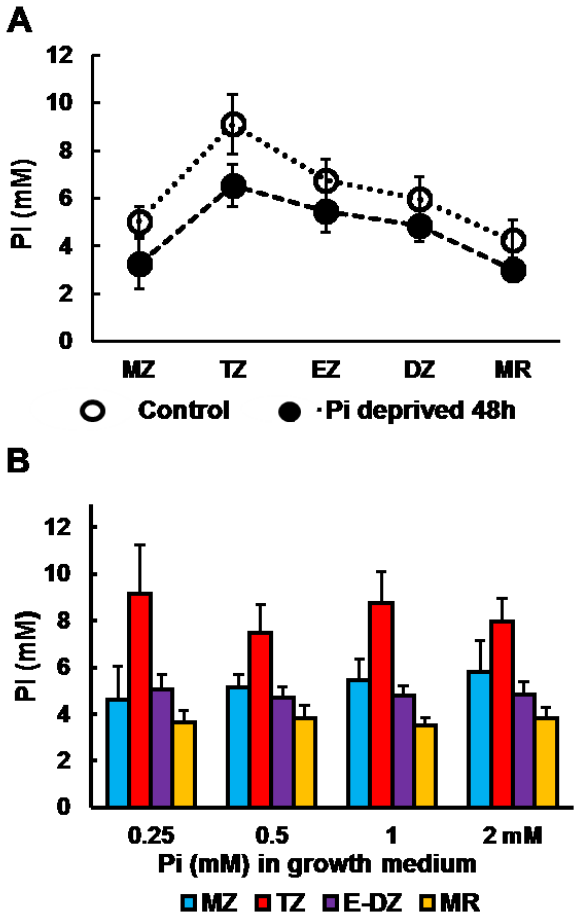

Figure 24. Relative cytosolic Pi concentrations are independent of external Pi. Relative Pi concentrations in the root zones are conserved. (A) 6 d old Arabodopsis seedlings were held in 0 mM Pi for 48 h before imaging root zones. The control group was maintained in sufficient Pi (0.25 mM). Plot represents mean Pi (mM) with standard deviation derived from 5-7 individual seedlings. (B) Arabidopsis seedlings were grown for 6 d in 0.5X MS medium with varying concentrations of Pi. Plot represents mean Pi (mM) with standard deviation from 5-7 individual seedlings.

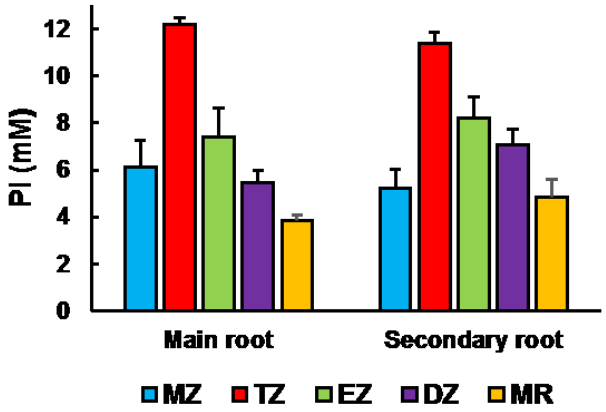

Figure 25. Root zone specific cytosolic Pi concentrations in three-week-old plants. Arabidopsis plants were grown in 0.5x MS agar plates for 3 weeks until the appearance of 9-10 adult leaves and 10-12 cm long roots. Primary and secondary roots were imaged to determine relative Pi concentrations in the five developmental zones of the root. Plotted values indicate mean Pi ± standard deviation from 3-5 individual plants.

4.2.5 The root developmental zones have varied temporal responses to Pi deprivation and Pi replenishment

To further resolve the significance of the Pi distribution pattern I measured changes in cytosolic Pi within each developmental zone during Pi deprivation followed by Pi replenishment. Previous studies established that Pi deprivation leads to loss of cytosolic Pi in the MR, and can be replenished by Pi resupply [151]. However, it was unknown if all the zones undergo cytosolic Pi loss and/or repenishment at equal rates. Since the root zones have distinct cellular activities, I hypothesized that the comparative rates of Pi deprivation and replenishment amongst the zones will differ due to different

rates of Pi utilization. To test this hypothesis, I first established the relative response of the root zones to Pi deprivation.

To determine the relative timing of decrease in cytosolic Pi I subjected 6 d old plants to 48 h Pi deprivation then measured cytosolic Pi every 12 h (**Fig. 26**). The earliest Pi decrease occurred in the MZ and MR at 12 h, and cells in these zones continued to lose Pi for up to 48 h, indicating these zones are highly sensitive to Pi deprivation. To confirm the Pi loss in the MR I measured total cellular Pi from root extracts, which is dominated (in volume) by the MR, and observed a steady decrease in total Pi from 12 to 48 h (**Fig. 27**). Cytosolic Pi in the TZ fluctuated from 24 to 48 h with the greatest decrease being at 48 h, suggesting that the TZ is less sensitive to Pi deprivation than the MZ (**Fig. 26**). The EZ and the DZ showed the greatest resistance to Pi deprivation and maintained their cytosolic Pi concentration beyond 36 h (**Fig. 26**). These results confirmed that the root developmental zones differ in their response to Pi deprivation.

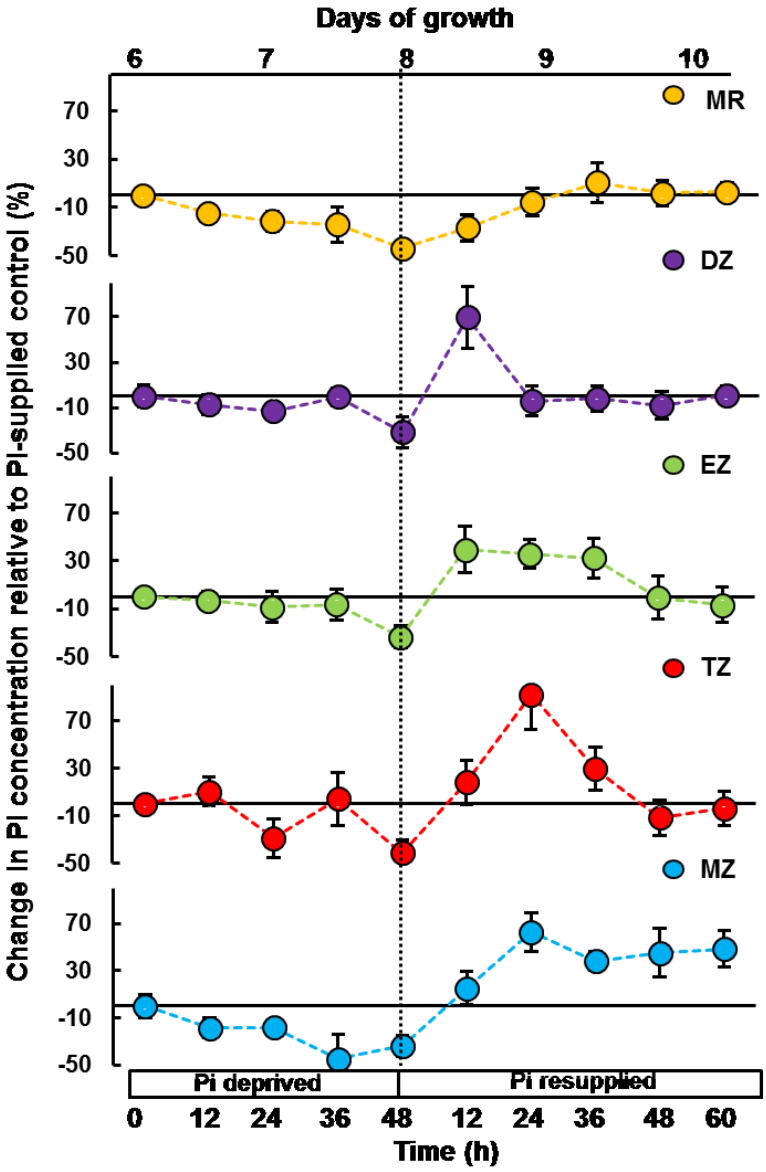

Figure 26. Relative changes in cytosolic Pi concentrations vary in root developmental zones under Pi deprivation followed by Pi replenishment. 6 d old Arabidopsis seedlings grown in 0.5x MS, 0.25 mM Pi were transferred to 0 mM Pi for 48 h and then transferred to 0.25 mM Pi for 60 h. Roots were imaged every 12 h to determine zone specific temporal changes in cytosolic Pi concentrations under Pi deprivation and resupply. Control plants were maintained in sufficient Pi (0.25 mM). The data represent percentage change in cytosolic Pi (mM) compared to control (Pi-supplied) plants. The mean and standard deviation values of the plots were calculated from 6-8 individual seedlings for each treatment and time point. The dashed line on the left demarcates the last Pi-deprivation measurement.

To compare the relative response of the zones to Pi replenishment, I resupplied 48 h Pi-deprived seedlings with 0.25 mM Pi then measured cytosolic Pi over time. Cytosolic Pi levels started increasing 12 h after replenishment. Thereafter I measured Pi every 12 h for up to 60 h (**Fig. 26**). The EZ and DZ showed the earliest increase (before 12 h) and hyperaccumulated Pi beyond pre-deprivation levels at 12 h. They were followed by the MZ and TZ which reached pre-deprivation Pi levels at 12 h and hyperaccumulated Pi at 24 h. The TZ stopped hyperaccumulation after 48 h and returned to pre-deprivation levels; however, the MZ continued to hyperaccumulate Pi for up to 60 h. The MR did not undergo any Pi hyperaccumulation and attained pre-Pi deprivation levels the latest, after 24 h. These results demonstrated that Pi is not replenished at equal rates to all the root zones.

The increase in cytosolic Pi after Pi replenishment was slower than expected. To test whether slow replenishment reflects slow Pi uptake, I replenished Pi-deprived plants with sufficient Pi along with 10 mM sodium cyanide. Cyanide blocks ATP synthesis and therefore prevents sequestration of Pi in ATP. I observed that after replenishment with Pi in the presence of cyanide, cytosolic Pi increased significantly within 10 s (**Fig. 28**). When Pi was added alone, cytosolic Pi did not increase significantly. These results indicate that Pi is taken up rapidly into the root; however, the newly acquired Pi is promptly assimilated into ATP. Therefore, a measurable increase in cytosolic Pi after replenishment is delayed and ultimately reflects the combined rates of uptake and recycling from ATP and perhaps other organic phosphates.

Interestingly, the MZ appeared to be the most sensitive to both Pi deprivation and replenishment. On the other hand, the EZ-DZ is most robust as cells in these zones lose Pi last and gain Pi first upon resupply. This varied temporal response to changes in Pi availability suggests that Pi levels are regulated by distinct cellular activities in each developmental zone. The pattern of cytosolic Pi concentrations may be a combination of Pi assimilation and recycling from organic phosphates, as well as Pi mobilization between zones.

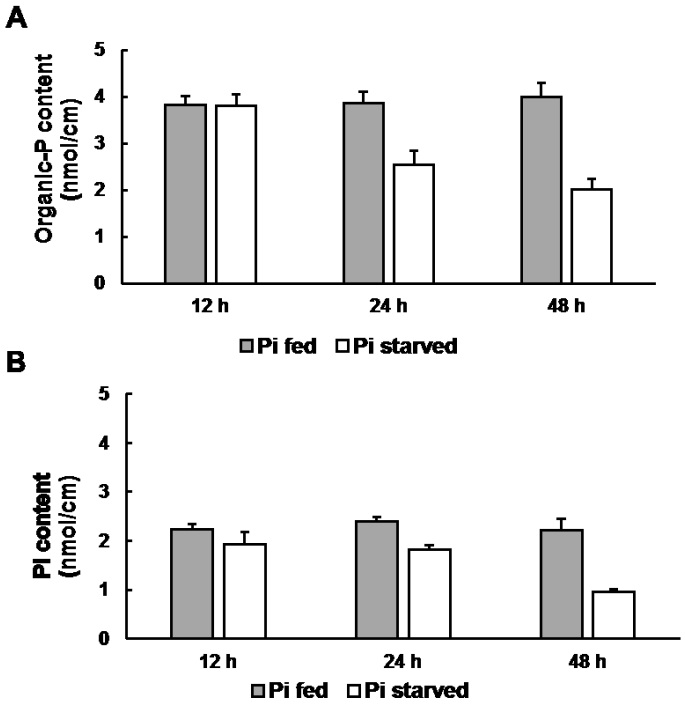

Figure 27. Total organic-P and Pi in roots after Pi deprivation. 6 d old Arabidopsis seedlings grown in 0.5x MS, 0.25 mM Pi were transferred to 0 mM Pi for 48 h. Control plants were maintained in 0.25 mM Pi. Total organic-P and Pi in whole-root extracts were measured after 12 h, 24 h and 48 h of Pi deprivation. Mean ± standard deviation values are plotted.

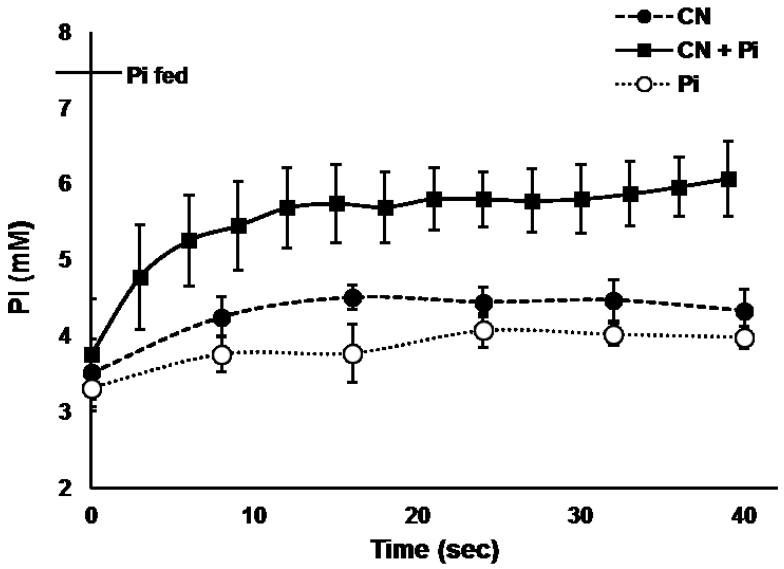

Figure 28. **Effect of cyanide on cytosolic Pi concentration in MZ cells.** 6-d old seedlings were deprived of Pi for 48 h. 0.5 mM Pi was then added to the seedlings and MZ epidermal cells were imaged to determine the time course of Pi replenishment in the cytosol. Square markers represent cytosolic Pi of plants resupplied with 0.5 mM Pi in the presence of 10 mM sodium cyanide. Circular and triangular markers represent cytosolic Pi in plants treated with 10 mM cyanide and 0.5 mM Pi, respectively. Data plotted represent mean ± standard deviation from 3-6 independent seedlings.

4.2.6 The zone-specific Pi distribution pattern correlates with cellular activities that are critical for root growth

I predicted that cytosolic Pi concentration in each developmental zone would reflect the net rates of intracellular Pi assimilation and recycling. Since the TZ had the highest cytosolic Pi concentration, I hypothesized that it would have the lowest rate of Pi assimilation. To test this idea I subjected plants to the metabolic inhibitor sodium cyanide, which inhibits ATP synthesis *via* mitochondrial oxidative phosphorylation [171]. The cells would still hydrolyze ATP to support metabolic activities; therefore,

cyanide should result in a net increase of free cytosolic Pi. Consequently, the relative increase in cytosolic Pi should correlate with the rate of Pi assimilation in each zone. I treated 6 d old seedlings with 10 mM sodium cyanide then imaged the roots within 3-5 min. Pi concentrations in all zones increased except the TZ (**Fig. 29A**). This result suggests that the TZ is metabolically less active, at least in terms of Pi assimilation, than the other zones.

A significant source of free cytosolic Pi is that liberated from anabolic processes. For example, incorporation of each nucleotide triphosphate during RNA synthesis releases pyrophosphate, which is then hydrolyzed to yield two molecules of Pi. Since the TZ has highest Pi concentration, I speculated that it has a high rate of Pi release from anabolic activities. To test this, I subjected seedlings for 12 h to alpha-amanitin, which blocks RNA polymerase II [232] and thus reduces Pi recycling from mRNA synthesis. Interestingly, the results revealed that alpha-amanitin reduced Pi concentrations in the MZ, EZ and DZ, but the TZ was unaffected (**Fig. 29B**). Contrary to my prediction, the result suggests that the TZ has less Pi recycling than cells in the adjacent zones; yet has the highest cytosolic Pi concentration.

I wanted to understand whether Pi accumulation in the TZ correlates with cellular activities leading to root growth and development. I therefore perturbed cell division and expansion with drugs and hormones then studied the consequences of these treatments on Pi distribution.

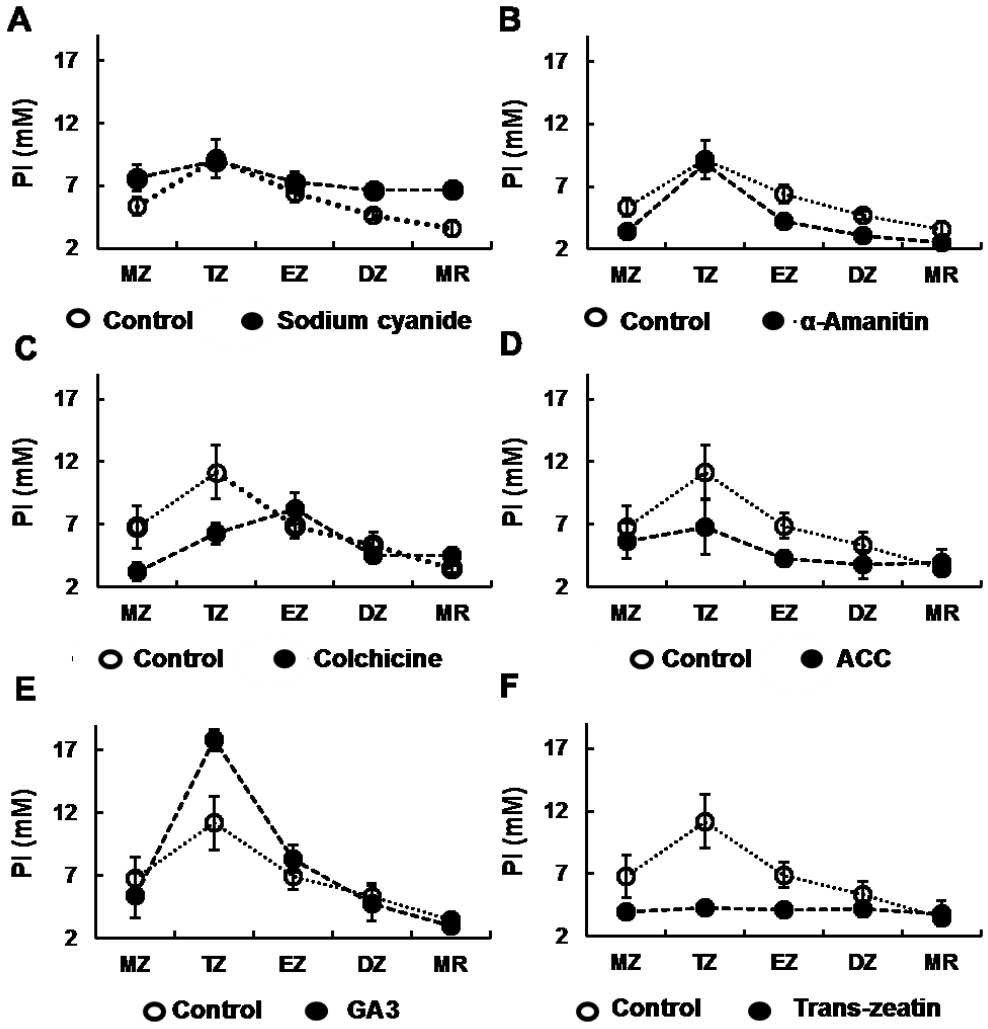

Figure 29. Influence of drugs and hormones on relative cytosolic Pi concentrations in root developmental zones. 6 d old Arabidopsis seedlings were treated with 10 mM sodium cyanide (1.5 min), 1 μg/ml alpha-amanitin (12 h), 0.1% colchicine (24 h), 10 μM ACC (24 h), 2 μM trans-zeatin (24 h) and 10 μM GA3 (24 h), and then root epidermal cells were imaged to measure cytosolic Pi concentrations in the five developmental zones. Plots represent mean ± standard deviation values from 6-8 individual seedlings.

Initially, I used colchicine and amino-cyclopropane (ACC) independently to inhibit cell division and cell elongation within the MZ and EZ respectively. Colchicine inhibits mitosis by blocking mitotic spindle formation [233]. Here, the colchicine

treatment decreased cytsolic Pi in the MZ and TZ; however, the EZ, DZ, and MR was unaffected (**Fig. 29C**). The decrease in cytosolic Pi concentration by colchicine can be explained as a downsteam effect of blocking mitosis because DNA synthesis releases Pi *via* a pyrophosphate intermediate. I treated plants with the ethylene precursor ACC to inhibit cell elongation in the EZ-DZ. Ethylene inhibits cell elongation by mediating polar auxin transport to the EZ-DZ [76,119]. After 24 h of ACC treatment free cytosolic Pi decreased in the EZ-DZ and TZ; however, the MZ and MR were unaffected (**Fig. 29D**). Inhibiting cell elongation decreased cytosolic Pi concentration because cell elongation involves synthesis of cellulose to make new cell walls, which liberates Pi by UDP-glucose pyrophosphorylase [234]. Interestingly, inhibiting cell division and elongation not only affected Pi levels within the respective root zones; it also affected the TZ which undergoes neither cell division nor elongation. This suggests that greater Pi accumulation in the TZ correlates with cellular activities related to root growth occuring in the adjacent zones.

To further explore this correlation, I used growth regulators that either inhibit or enhance root growth and asked whether it altered the Pi distribution pattern. First, I used trans zeatin, which inhibits both cell division and cell elongation simultaneously [108] (**Fig. 29F**). After 24 h of trans-zeatin treatment, Pi concentrations in the first four zones decreased; however, the greatest decrease occurred in the TZ. I then asked whether enhancing cell division and elongation would increase cytosolic Pi concentration in the TZ even further. Specifically, I treated seedlings with Gibberellin A3, which enhances cell division in the MZ and cell elongation in the EZ, separately in the presence (**Fig**

29E) and absence of Pi (**Fig. 30**) [97,99]. The GA3 treatment significantly increased cytosolic Pi concentration in the TZ; however, the MZ, EZ, DZ and MR were unchanged. Interestingly, cytosolic Pi concentration in the TZ was highest in GA3-treated roots (longer in length), and was lowest in trans zeatin-treated roots (shorter in length) (**Fig. 31**). These results confirmed that the level of Pi accumulation in the TZ correlates with cellular activities responsible for overall root growth.

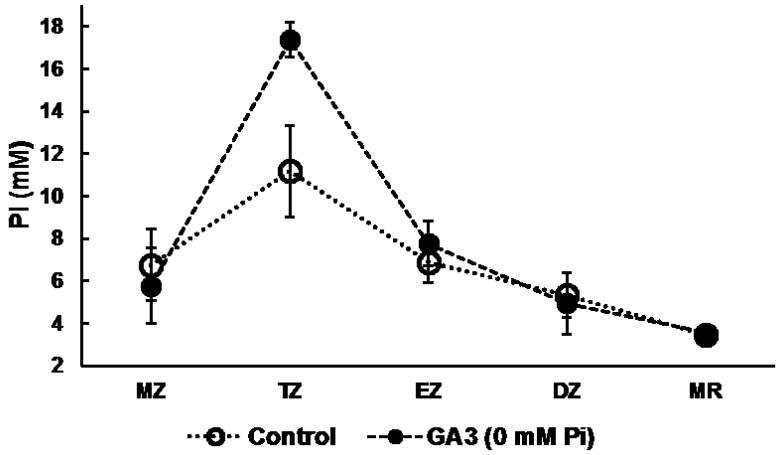

Figure 30. **GA3 enhances the root Pi pattern in the absence of external Pi.** Graph shows mean cytosolic Pi with standard deviation derived from root epidermal cells of 6 d old Arabidopsis seedlings (n= 3-5) treated with 10 μM GA 3 for 24 h in the absence of external Pi.

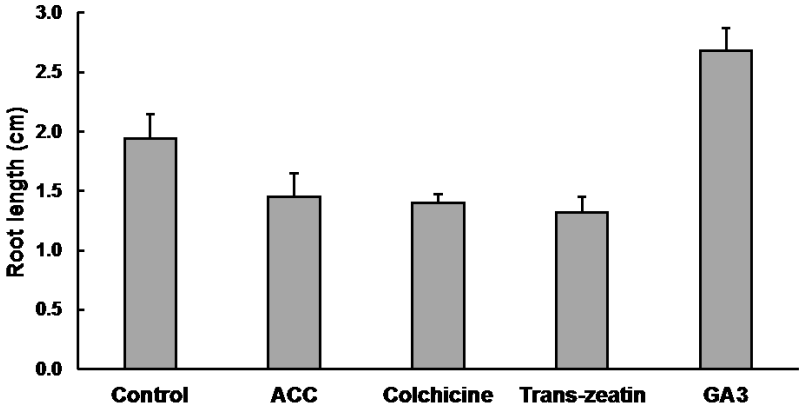

Figure 31. Effect of hormones and drugs on root length. 6 d old Arabidopsis seedlings were treated with 0.1% colchicine, 10 μM ACC, 2 μM trans-zeatin and 10 μM GA3 for 24 h and then root length was measured. Data reflect mean root length ± standard deviation.

4.3 Discussion

This study produced a high-resolution map of cytosolic Pi concentrations in the root. One might expect that the pattern of Pi accumulation in the root would correspond to the region of greatest Pi uptake activity. As described in literature, Pi uptake occurs primarily in the MZ within the root cap and in the DZ-MR region with highest number of root hairs. Additionally, transcript and proteome data have revealed PHT1 transporters accumulate in the root cap and root hairs [20,235,236]. Therefore, the highest cytosolic Pi concentrations would be expected in the MZ and DZ. However, my results showed that the TZ has the greatest cytosolic Pi concentration, despite lower Pi uptake activities than the MZ and DZ. Higher Pi concentrations in the TZ, even in the absence of external Pi, further supports the idea that cytosolic Pi accumulation in this zone is not a direct consequence of Pi uptake.

It is important to distinguish the accumulation patterns of free cytosolic Pi from total cellular phosphorus. ^{33}P measurements indicated that cellular phosphorus accumulates in the primary meristem of the root, or the MZ, which is also a zone of high Pi uptake [237]. However, my results demonstrated that the MZ has less cytosolic Pi than the TZ. I therefore predict that when Pi is acquired it is also rapidly incorporated into organic forms, such as ATP, nucleic acid, and phospholipids that are required to make new cells of the primary meristem. Indeed, Pi deprivation/replenishment studies conducted while blocking ATP synthesis indicated that newly acquired Pi is rapidly assimilated in the MZ (**Fig. 28**). When Pi-deprived roots were resupplied with Pi, cytosolic Pi concentration did not increase immediately. However, when the roots were treated with the ATP synthesis inhibitor sodium cyanide, cytosolic Pi concentration increased dramatically in the MZ within 5-15 s (**Fig. 28**). Thus imported Pi is rapidly assimilated, and consequently, free cytosolic Pi does not accumulate in the MZ.

The results of this study indicate that steady-state cytosolic Pi levels reflect a combination of Pi uptake, assimilation, metabolic recycling, and mobilization between the developmental zones. The TZ has the slowest rate of Pi assimilation into ATP as indicated by cyanide treatment. [57,62]. Additionally, the alpha-amanitin treatment revealed that the TZ also has the lowest rate of Pi liberation from RNA synthesis, which fails to correlate with the greater accumulation of Pi in the TZ. Interestingly, perturbing growth-related cellular activities in the flanking MZ and EZ influence Pi levels in the TZ. For example, GA mediated enhancement of cell division in the MZ and cell

elongation in the EZ, increases Pi in the TZ. Based on these observations, I speculate that Pi from the adjacent MZ and EZ mobilize into the TZ cells.

The idea of Pi mobilization from flanking zones into the TZ was further reinforced when Pi concentration increased in the TZ under GA3 treatment. GA3 increased root growth due to enhanced cell division in the MZ, and cell expansion in the EZ-DZ. Enhanced cell division and elongation requires numerous anabolic porcesses, including synthesis of DNA, RNA, and cellulose, which should liberate Pi in the MZ and EZ-DZ. However, free cytosolic Pi levels in the MZ and EZ-DZ were unaffected by GA3 treatment, possibly due to rapid utilization of released Pi for cell division and elongation. Nonetheless, cytosolic Pi concentrations increased significantly in the TZ after GA3 treatment. It is plausible that free cytosolic Pi liberated by GA3-mediated induction of cell division and elongation ultimately mobilized into the TZ from the flanking zones. Since the TZ had the slowest rate of Pi assimilation, mobilized Pi was not utilized rapidly and therefore accumulated in the TZ cytosol. Furthermore, GA3 treatment increased cytosolic Pi in the TZ in the absence of external Pi (**Fig. 30**), further indicating that Pi accumulation in these cells is a result of internal Pi recycling and mobilization rather than enhanced Pi uptake.

This study suggests that Pi accumulation in the TZ is a function of normal root growth and development. Drug and hormone treatments that decreased cytosolic Pi concentrations in the TZ also resulted in shortened root length (**Fig 31**). On the other hand, GA3 treatment simultaneously increased root length and cytosolic Pi concentration in the TZ. These results corroborate the importance of Pi accumulation in the TZ for root

growth. As pointed out by Baluska *et al.*, MZ cells cannot immediately enter the EZ because they lack the cellular machinery to begin rapid cell elongation. Therefore, cells at the distal end of the MZ enter the TZ to undergo preparations, such as cytoskeleton reorganization, and modifications of vacuoles and cell wall to begin rapid elongation. TZ cells ultimately enter the EZ and begin rapid elongation. The preparation of cells in the TZ is critical because these cells require the resources to synthesize macromolecules (*e.g.*, phospholipids and cellulose) needed to make new cell membranes and cell wall. Therefore, high cytosolic Pi concentrations in the TZ becomes crucial to fuel rapid cell elongation when the cells enter the EZ. I predict that the excess Pi serves as a reservoir to support EZ cells until they acquire root hairs for massive Pi uptake after entering the DZ. Therefore, the accumulation pattern of Pi in the root apex is important for overall growth of the root.

4.4 Material and methods

4.4.1 Plant growth

All experiments were performed using Arabidopsis plants expressing cytosolic cpFLIPPi sensor as described by Mukherjee *et al.* [151]. Seeds were germinated and grown in 96-well microplates in 230 µL of 0.5x MS medium [222] containing 0.25% (w/v) sucrose and 250 µM Pi in a growth chamber (60% relative humidity, 21°C, and 90 µmol/m^2/s light intensity for a 16 h photoperiod). Seedlings were grown for 6 days or until the roots were 1.5 cm long and then transferred to the indicated medium for further

treatments. For root Pi imaging of 3 week old plants, seedlings were grown for 3 weeks in 0.5x MS, 0.7% agar plates until the plants had 8-10 adult leaves and 10-12 cm long roots.

4.4.2 Live imaging of roots and derivation of cytosolic FRET/eCFP ratios

Seedlings were transferred from their growth plates to a coverslip and mounted in their respective growth medium. A small coverslip was placed on top of the root to keep it flat during imaging. Roots were imaged using an inverted Olympus IX81 microscope equipped with a Yokogawa CSU-X1 Spinning Disk confocal unit and an iXon3 897 EMCCD camera (Andor Technology, Concord, MA, USA). Plants were imaged using a 40 X (numerical aperture 1.3) oil immersion objective. All images were acquired using Metamorph software. The laser wavelength used for CFP excitation was 445 nm. The emission filter for eCFP was 483/32 nm and the emission filter for FRET was 542/27 nm. The laser wavelength used for direct excitation of cpVenus was 515 nm. The image acquisition parameters such as laser power, electron multiplier gain, exposure time, camera sensitivity were maintained at same settings for all experiments. Acquired fluorescent micrographs were analyzed using ImageJ software. Mean fluorescent intensity values were measured from images in the eCFP, FRET-cpVenus and direct cpVenus emission channels. Raw FRET intensities were converted to sensitized FRET values after correcting for donor spectral bleedthrough and acceptor cross excitation as described by Banerjee *et al.* [230] by using plants expressing the single fluorophores, eCFP and cpVenus. FRET ratios were calculated by dividing the mean sensitized FRET

intensity by mean eCFP emission intensity. The sensitized FRET/eCFP ratios were converted to milimolar Pi concentrations using the *in vivo* calibration.

4.4.3 Microinjection of Pi to generate an in vivo calibration of cpFLIPPi sensor

To create an *in vivo* calibration of the cpFLIPPi sensor, I injected Pi buffers into the cytosol of transition zone epidermal cells of the root and imaged the cells to determine FRET/eCFP ratios. The injection buffer was composed of 50 mM MOPS-KOH (pH 7.3), 75 mM K-gluconate, 0.5 mM $MgCl_2$, and K-phosphate (pH 7.3) to yield the desired Pi concentration. The concentrations of K-gluconate and K-phosphate were adjusted to maintain constant concentration of potassium (75 mM). I also injected 1 μM purified cpFLIPPi sensor protein to replace the cytosolic sensor displaced during injection. Purified mRuby2 protein was included in the injection buffer as a marker to demarcate the spread of the injected solution. An Arabidopsis seedling (6-7 days old) was laid on a coverslip and it was attached to the coverslip with tape across the root so that about 2 mm of the root tip remained exposed. The cotyledons and most of the root were covered by a wet filter paper to keep the seedling hydrated during the injection. Microinjection capillaries were filled with injection solution attached to hydraulic micromanipulators, which were connected to an Eppendorf Femtojet pump. 20-25 picoliters of Pi solution was injected into each cell, which is 4-5 times the volume of the cytosol (5 picoliter) of a typical transition zone cell. The volume of the cytosol was estimated from fluorescent micrographs of root TZ cells, considering the cell and the vacuole as cuboids. To calculate the volume of injected solution, the injection buffer was

injected into a puddle of halocarbon oil for the same amount of time used to inject a cell, and the volume of the puddle was calculated from the diameter of the spherical puddle. The pump was set at maximum pressure to deliver the solution and it was injected for 5-6 seconds. The Pi buffer, after completely filling the cytosolic space, moved to the adjacent cells via the plasmodesmata, which was seen as a change in FRET/eCFP ratio for the injected and adjoining cells (**Fig. 20**). About 6-8 independent cells were injected with each of eight Pi concentrations and the FRET/eCFP values of the injected cells were used to create an *in vivo* calibration of the cpFLIPPi sensor. This calibration was used to calculate Pi concentration from FRET/eCFP values.

4.4.4 Pi deprivation, Pi replenishment, and hormone and drug treatments

For Pi deprivation, 6 d old seedlings grown in 0.5x MS (250 μM Pi) were transferred to wells containing 230 μl of 0.5x MS without Pi. The plants were held in Pi deprivation for 48 h and imaged every 12 h. The growth medium was replaced every 24 h with fresh medium. For Pi replenishment, seedlings deprived of Pi for 48 h were transferred to 0.5x MS medium with 250 μM Pi and maintained for 60 h. The plants were imaged every 12 h and growth medium was replaced with fresh medium every 24 h. For the alpha- amanitin treatment, seedlings were held in 0.5x MS medium with 1 μg/ml alpha-amanitin and imaged after 12 h. For cyanide treatment, seedlings grown in 0.5x MS medium were transferred to a coverslip and mounted in 10 mM sodium cyanide. The seedlings were held in cyanide for 1-1.5 min prior to imaging. For colchicine, 5-amino-cyclo propane (ACC), trans-zeatin and gibberellin A3 (GA3)

treatments, the seedlings were maintained for 24 h in 0.5x MS medium containing 0.1% colchicine, 10 μM ACC, 2 μM trans-zeatin, or 10 μM GA3, respectively, then the roots were imaged. For all treatments, the plants were tested for cell viability by the nucleic acid stain Sytox Orange [238]. We treated plants expressing the control sensor, cpFLIPPi-Null, with the same drugs and conditions to monitor any potential non-specific changes in FRET/eCFP ratios. None of the treatments except colchicine showed a significant change in the FRET/eCFP ratio of the cpFLIPPi-Null. Colchicine treatment resulted in a minor increase (1.6% or less) in the FRET/eCFP ratio. The FRET/eCFP ratios of the cpFLIPPi sensor were therefore corrected by subtracting the percentage change in ratio due to non-specific factors (the percentage change was derived from the cpFLIPPi-Null ratios) [230]. The corrected ratios were used to determine Pi concentrations after the colchicine treatment.

4.4.5 Measurement of total organic-P and Pi from roots

Seedlings were grown in 0.5x MS medium with sufficient Pi (0.25 mM) for 6 d and then transferred to 0.5x MS medium containing no Pi to measure total organic-P and Pi of roots after 12 h, 24 h, and 48 h of Pi deprivation. The control group of plants was maintained in 0.25 mM Pi. Plants were pooled in groups of ten and 3-4 groups of seedlings were used for each treatment and time point. Roots were excised from the seedlings and used to measure total P and Pi by a phosphomolybdate colorimetric assay [137,239]. Organic-P was calculated by subtracting Pi from total P. Mean organic-P and Pi was normalized to the average length of the root for each group of seedlings.

CHAPTER V

THE ROLE OF PHOSPHATE TRANSPORTERS IN MODULATING CHLOROPLAST PHOSPHATE HOMEOSTASIS

5.1 Introduction

Inorganic phosphate (Pi) within the chloroplast influences photosynthesis and carbon partitioning. Pi is a substrate for ATP synthesis *via* photophosphorylation during the light reaction of photosynthesis. It also acts as a key regulator to determine the fate of assimilated carbon with respect to its utilization in stromal transitory starch synthesis, or cytosolic sucrose synthesis. The source of Pi in the chloroplast stroma is the cytosol; the chloroplast depends on Pi transporters present on its inner envelope membrane to modulate stromal Pi levels [30,123].

Triose phosphate translocator (TPT) is the first characterized member of the pPT family of Pi transporters. TPT imports cytosolic Pi in exchange for stromal triose phosphates that are generated as intermediates of the Calvin Benson cycle. In the cytosol, triose phosphates are used for sucrose synthesis, which liberates Pi for return to the stroma via TPT, while sucrose is distributed to sink tissues [127,128]. When the demand for sucrose diminishes, the rate of sucrose synthesis slows and thereby limits the amount of Pi available for import into the chloroplast. In this case, triose phosphates remain in the stroma and are directed toward the synthesis of transitory starch. Decreased concentration of stromal Pi favors this process because Pi is an allosteric inhibitor of ADP glucose pyrophosphorylase, which catalyzes the first committed step of

starch synthesis [129-131]. Studies have shown that a loss of TPT function leads to increased synthesis and turnover of starch in the stroma coupled with the export of maltose to effectively compensate for the defect in carbon export [132,133]. However, compensatory mechanisms for the *tpt* defect in Pi import are unknown, but the lack of a significant growth defect implicates the presence of other Pi import activities.

Two candidate Pi transporters, PHT2;1 and PHT4;4, localize to the chloroplast inner envelope membrane. Both transporters have twelve membrane-spanning domains; however, they do not share sequence similarity with each other or pPT transporters. Transport studies conducted in yeast showed that Pi transport catalyzed by PHT2;1 and PHT4;4 is sensitive to protonophores, suggesting the possibility of proton-coupled transport. In addition, the *pht2;1* mutant shows low Pi content, decreased biomass, and altered expression of Pi-starvation marker genes [135-137]. Miyaji *et al*. [240] conducted *in vitro* transport assays using proteoliposomes containing the PHT4;4 protein, and found that PHT4;4 catalyzed chloride-dependent Pi transport, but also catalyzed ascorbate transport when proteoliposome membrane potential was adjusted to be positive inside. The mechanism of ascorbate transport is unclear because the chloroplast has a negative inside membrane potential. Nevertheless, the *pht4;4* mutant displayed reduced ascorbate levels in leaves and impaired heat dissipation during photosynthesis. In this work, I have studied the physiological roles of both PHT4;4 and PHT2;1 with respect to Pi transport across the chloroplast inner envelope in live plants.

The optimization of a genetically encoded FRET-based biosensor for Pi (cpFLIPPi) has enabled live monitoring of Pi levels in subcellular compartments.

Mukherjee *et al*. [151] used the cpFLIPPi-5.3m sensor to report a stromal Pi accumulation defect in the *pht4;2* mutant, indicating that PHT4;2 mediates Pi export from root plastids. I optimized imaging methods for Pi sensors in chloroplasts, which included corrections for the effects of pigments [230]. In this section, I used the cpFLIPPi sensor to compare relative levels of Pi in the stromal of wild-type plants and mutants of *pht2;1*, *pht4;4* and *tpt.* My hypothesis was that altered accumulation of Pi in mutant backgrounds would reveal the direction of Pi transport by the affected transporter (import vs. export). The *tpt* mutant served as a control, and in some cases as a sensitized genetic background. I hypothesized that both PHT2;1 and PHT4;4 contribute to the fine tuning of stromal Pi levels, which would be reflected as altered patterns of stromal Pi accumulation in the *pht2;1* and *pht4;4* mutants.

5.2 Results

5.2.1 Pi import vs. export by PHT2;1 and PHT4;4

To detect potential chloroplast Pi accumulation defects in *pht2;1* and *pht4;4* mutants, I expressed a chloroplast-targeted cpFLIPPi sensor in wild-type and each of the mutants. I grew the transgenic plants for 3 weeks in a 16 h light/8 h dark photoperiod (100 μmol/m^2/s light intensity) then imaged mesophyll chloroplasts in the third rosette leaf of each plant. As expected, the *tpt* mutant yielded higher FRET/cpVenus ratios consistent with its Pi import defect. The *pht2;1* mutant also had significantly higher FRET/cpVenus ratios than wildtype indicating lower Pi concentrations, which suggests

that PHT2;1 also imports Pi into the chloroplast (**Fig. 32**). By contrast, no Pi accumulation defects were detected in epidermal chloroplasts of either *pht2;1* or *tpt.* However, it is currently unknown if these transporter genes are expressed in epidermal cells.

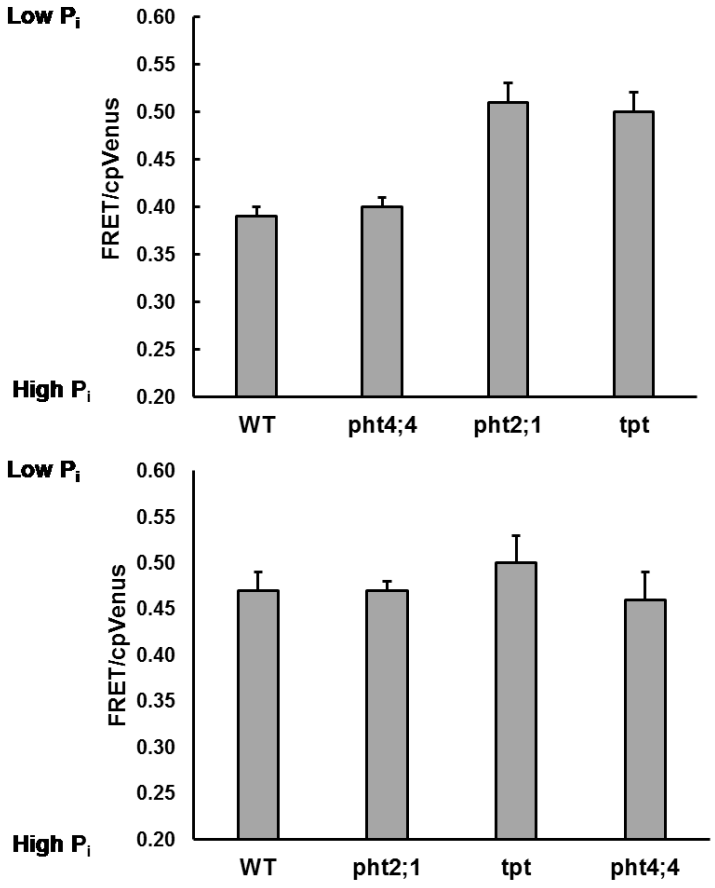

Figure 32. FRET/cpVenus ratios of chloroplast reveal directionality of Pi transport. FRET/eCFP ratios from (A) mesophyll and (B) epidermal chloroplasts of wild type, *pht2;1, pht4;4,* and *tpt* plants. Data represents mean ± standard deviation. N=8.

FRET/cpVenus ratios from mesophyll chloroplasts of wildtype and the *pht4;4* mutant were equivalent. This result suggests that PHT4;4 does not significantly contribute to chloroplast Pi transport. However, transport activity may fluctuate with the photoperiod. Therefore, in the next step I monitored stromal Pi levels of wild-type and mutant plants at the start, midpoint, and endpoint of the photoperiod.

5.2.2 The effect of photoperiod on chloroplast Pi transport

The rate of photosynthesis and carbon utilization fluctuates with progression of the day, and would therefore lead to altered rates of Pi assimilation and recycling within the chloroplast. I hypothesized that the rates of Pi transport across the chloroplast inner envelope would also vary throughout the photoperiod. Previous investigation of *pht4;4* carried out in the midpoint of the photoperiod failed to show any defect in stromal Pi accumulation. However, both *tpt* and *pht2;1* exhibited a defect in Pi import at the midpoint. Therefore, to reveal whether the rates of Pi import via PHT2;1 and TPT vary during the photoperiod and to address whether PHT4;4 mediates photoperiod-specific Pi transport, I compared stromal Pi levels of wild-type and mutant plants at the start, midpoint and endpoint of the photoperiod (**Fig. 33**). The results suggested that the magnitudes of Pi transport catalyzed by PHT2;1 and TPT were both greatest at the endpoint of the photoperiod. This result was consistent with previous reports demonstrating that transcription of these transporter genes is induced by light [137,241,242]. Additionally, the results suggests that PHT2;1 may have a greater contribution to Pi import at the endpoint of photoperiod than TPT.

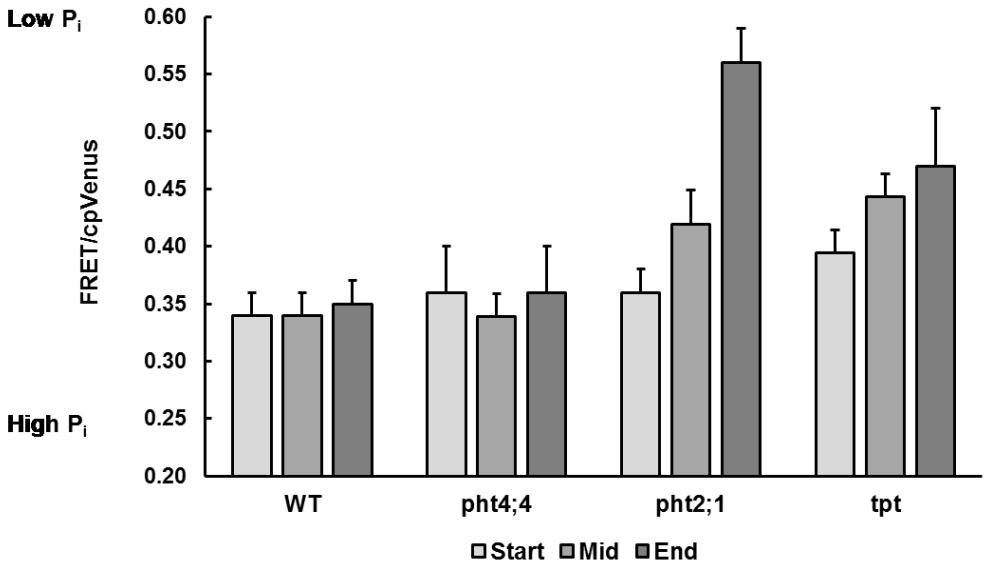

Figure 33. FRET/cpVenus ratios of chloroplast Pi transporter mutants at three time points in the photoperiod. FRET ratios were measured at the start, midpoint and endpoint of the photoperiod from wild-type, *pht2;1, pht4;4,* and *tpt* plants. Data represent mean ± standard deviation. N= 6

No Pi-accumulation defect was detected in the *pht4;4* mutant at any point in the photoperiod suggesting that PHT4;4 does not have a significant role in chloroplast Pi transport. However, Pi concentrations within *pht4;4* chloroplasts may not be within the detection range of the cpFLIPPi sensor. For example, if *pht4;4* has a Pi export defect and the resulting hyperaccumulation of Pi saturates the cpFLIPPi sensor then it would be difficult to detect a difference between *pht4;4* and wildtype. To address this possibility, I imaged chloroplasts of *pht4;4* plants in a sensitized genetic background that would reduce stromal Pi.

5.2.3 Pi transport by PHT2;1 and PHT4;4 in a sensitized genetic background

No Pi accumulation defects were detected in the *pht4;4* mutant. One possible explanation was that the cpFLIPPi sensor was saturated due to high Pi levels within the *pht4;4* chloroplasts. Alternatively, compensatory Pi transport by TPT or PHT2;1 may have minimized the effect of the *pht4;4* mutation. To address these two possibilities, I combined the *pht4;4* mutation separately with the *tpt* and *pht2;1* mutations (**Fig. 34**). However, no significant difference in FRET/cpVenus ratios measured in the single *tpt* and *pht2;1* mutants compared to the *pht4;4 tpt* and *pht4;4 pht2;1* double mutants were detected, eliminating the possibility of compensatory Pi transport by PHT2;1 and TPT. These results also negated the likelihood that a Pi export defect was masked due to saturation of the cpFLIPPi sensor by high stromal Pi concentrations because the *tpt* and *pht2;1* mutations both reduce stromal Pi concentration. That is, if *pht4;4* had a defect in Pi export then the FRET/cpVenus ratios of *pht4;4 tpt* or *pht4;4 pht2;1* double mutants would have been lower than the corresponding *tpt* and *pht2;1* single mutants. I therefore conclude that PHT4;4 does not transport Pi across the chloroplast inner envelope.

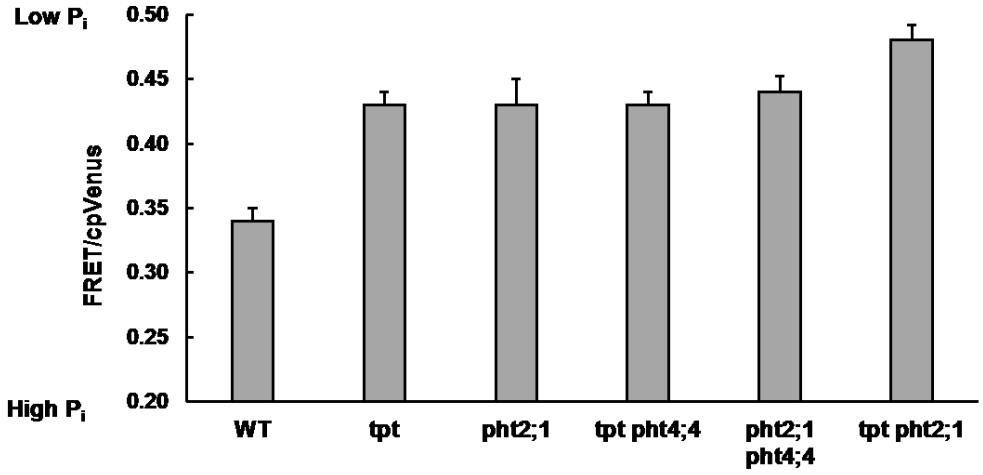

Figure 34. FRET/cpVenus ratios of wild type and combinations of chloroplast Pi transporter mutants. Data represent mean ± standard deviation. N=6.

PHT2;1 and TPT both catalyze Pi import. However, these activities are not completely redundant because FRET ratio measured in the *tpt pht2;1* double mutant was higher than in the *tpt,* and *pht2;1* single mutants (**Fig. 34**) indicating that TPT and PHT2;1 activities are additive. Additional studies are needed to fully understand the physiological roles of these transporters.

5.3 Discussion

Functional characterization of individual Pi transporters that modulate stromal Pi levels is challenging due to potential compensatory processes in the corresponding mutants. Comparative FRET-based analyses revealed that both *pht2;1* and *tpt* have reduced stromal Pi indicating that PHT2;1 and TPT import Pi into the chloroplast. However, the lack of any obvious growth defect for the *tpt pht2;1* double mutant suggests that compensatory Pi transport exists. Interestingly, a *pht4;4 tpt pht2;1* triple

mutant displays severe growth defects (Mukherjee *et al*., unpublished). This phenotype suggests that PHT4;4 compensates for the Pi import defects of *tpt* and *pht2;1* mutations. It would be informative to determine if *PHT4;4* transcript levels are elevated in the *tpt pht2;1* double mutant.

Contrary to my expectation, the *pht4;4* mutant failed to show any stromal Pi accumulation defect despite the fact that PHT4;4 mediates Pi transport in two different assay systems [135,240]. One possible explanation for this discrepancy could be that the sensitivity of the current FRET-based assay is inadequate to detect subtle differences in Pi concentration. Given the observed ascorbate transport activity of PHT4;4 [240], it is possible that PHT4;4 catalyzes Pi export from a wild-type chloroplast in exchange for cytosolic ascorbate. However, excess stromal Pi in the mutant may be funneled to other Pi-consuming biochemical processes. Further studies in which *pht4;4* is combined with ascorbate biosynthesis mutants (deficiency and over-production) may resolve whether PHT4;4 couples Pi and ascorbate transport across the chloroplast inner envelope membrane.

Direct monitoring of stromal Pi levels combined with studies on photosynthetic efficiency may divulge the mechanisms leading to efficient phosphate utilization. Previous studies suggested that reduced Pi concentration in the chloroplast can be limiting for photosynthesis, which would eventually limit biomass [203]. Similarly, the reduced biomass of the *pht2;1* mutant reported by Versaw and Harrison [137] may reflect reduced photosynthetic efficiency due to low stromal Pi concentration. My work comparing FRET data revealed that the *tpt pht2;1* double mutant displays even less

stromal Pi than the single *tpt* and *pht2;1* mutants. However, the *tpt pht2;1* double mutant does not suffer an exaggerated decrease in biomass compared to *pht2;1*. These results suggest that the *tpt pht2;1* double mutant may have similar photosynthetic efficiency compared to *pht2;1* despite having lower stromal Pi. Further studies comparing stromal Pi and photosynthetic efficiency using all combinations of *tpt, pht2;1* and *pht4;4* are needed to dissect the biochemical processes occurring within the chloroplast.

5.4 Materials and methods

5.4.1 Generating transgenic Arabidopsis plants

The plasmids cpFLIPPi-5.3m and cpFLIPPi-Null (described previously, [230]) were introduced into Arabidopsis plants by *Agrobacterium tumefaciens*-mediated floral dip transformation [221]. The sensors were targeted to the chloroplast by inserting a 237 bp fragment encoding the 79-amino acid RbcS chloroplast transit peptide [220] in frame at the 5' end of the sensor genes. Transgenic wild-type and chloroplast transporter mutant plants with the Pi sensor were selected on 0.5x MS agar plates with 10 μM phosphinothricin. All experiments were performed with the progeny of a representative T2 plant that maintained uniform fluorescence.

5.4.2 Plant growth and live imaging of chloroplast Pi

Transgenic plants were grown in soil for three weeks in a growth chamber (60% relative humidity, 21°C, and 90 μmol/m2/s light intensity for a 16 h photoperiod). The

third rosette leaf was detached and placed adaxial side down on a custom made imaging chamber (http:// microscopy.tamu.edu/lab-protocols/light-microscopy-protocols.html). The leaf was treated with perfluorodecalin [223] to eliminate air bubbles and covered with a glass brick for flattening. Mesophyll chloroplasts were imaged using an inverted Olympus IX81 microscope equipped with a Yokogawa CSU-X1 Spinning Disk confocal unit and an iXon3 897 EMCCD camera (Andor Technology, Concord, MA, USA). Plants were imaged using a 40x (numerical aperture 1.3) oil immersion objective. A 445 nm laser was used to excite eCFP. A 483/32 nm filter was used to detect eCFP emission, and a 542/27 nm filter was used to detect FRET-derived cpVenus emission (FRET emission) and emission from directly-excited cpVenus. A 515 nm laser was used for direct excitation of cpVenus. Images in each emission channel were processed and FRET ratios were calculated using a regression-based method as described in Chapter III. All experiments were repeated with plants expressing the cpFLIPPi-Null in all genetic backgrounds. The data from these experiments were used to correct for non-specific changes in FRET ratios due to genetic mutations following the same procedure described in chapter III [230].

CHAPTER VI

CONCLUSIONS AND FUTURE DIRECTIONS

Resolving the mechanisms underlying Pi utilization has been a long-standing goal. However, the inability to monitor *in vivo* Pi concentrations with high spatial resolution has limited progress in this field of research. The development of genetically encoded cpFLIPPi biosensors addressed this problem and provided a powerful tool for live Pi measurement. Nevertheless, the analysis, interpretation, and comparison of biosensor data have been challenging. One of the challenges is resolving non-specific responses due to changes in pH, viscosity, and other ions. Therefore, environmental factors and genetic mutations can affect sensor readout and increase the probability of data misinterpretation. Furthermore, FRET-based sensors can only report relative differences in ligand concentrations rather than absolute concentrations. The chemical environment inside a cell is too complex to replicate *in vitro*, which makes direct comparison of *in vivo* FRET data to an *in vitro* calibration inaccurate. These limitations have restricted efforts to quantify subcellular Pi concentrations in live cells.

My work focused on optimization of the cpFLIPPi biosensor and the development of methods to quantify Pi in live multicellular organisms. To achieve this goal I used approaches that circumvent or remediate the major limitations of FRET-based Pi monitoring. One of the key approaches was the distinction and quantification of Pi-specific from non-specific changes in FRET. Chapter II of this work demonstrated that the percent change in FRET due to non-specific effects is equivalent in the

cpFLIPPi sensor and the non-responsive control sensor cpFLIPPi-Null. Consequently, data derived from cpFLIPPi-Null can be used to correct for non-specific changes in FRET values. Another important aspect of my study was the implementation of a regression-based approach for combining and comparing FRET data of plant populations. Although one might expect that the ratio of FRET emission intensities to donor emission intensities should be proportional and self-correcting because the eCFP and cpVenus components are translationally fused, multiple factors can affect these fluorescence proteins unequally and thereby introduce large variation in the ratios. The regression-based approach minimizes variation and improves the ability to resolve small changes in ligand concentrations, especially in pigmented organs. Finally, I developed an *in vivo* calibration of the cpFLIPPi sensor that enabled quantification of absolute concentrations of Pi in the cytosol. Direct microinjection of Pi into the cytosol eliminated the optical discrepancies between cells and the *in vitro* assay system, thus enabling the conversion of *in vivo* FRET ratios to absolute concentrations. The combination of the described approaches towards optimization of live Pi measurement provides a blueprint for other FRET-based sensors. The limitations of the assay system addressed here are common to other studies using live measurement of analytes in multicellular organisms. Therefore, this study provides a guide for methodical refinement of FRET-based measurement and real-time quantification of analytes that can enable investigators to answer numerous long-standing questions.

The ability to monitor cytosolic Pi concentrations with high resolution led to one of the key findings of this study. That is, Pi distribution in the root is not uniform and

varies spatially in wild-type Arabidopsis. Specifically, the TZ in the root apex has the highest accumulation of Pi. This accumulation pattern is independent of external Pi and is instead governed by internal Pi assimilation and recycling. Importantly, I discovered that growth regulators (gibberellin, cytokinin, and ethylene) that affect cellular activities responsible for root growth (cell division and cell elongation) influence this pattern. However, these regulators are pleiotropic and cross interact with each other. Therefore, identifying a specific cellular activity responsible for generating the Pi distribution pattern is challenging. For example, I found that blocking cell division alone by colchicine was insufficient to perturb the Pi distribution pattern. Identifying all the individual activities causing this pattern may be problematic. Nevertheless, GA3 and trans zeatin treatments indicated that Pi distribution correlates with overall root growth (**Fig. 29-31**). This correlation provides a reasonable direction for future studies. For example, it would be interesting to examine Pi distribution in GA mutants that correlate with root growth, such as mutants of the GA repressor DELLA. Such studies may reveal important aspects of how this hormone functions, as well as the genetic basis of root growth. Ultimately, such studies may lead to the development of crops with improved yields.

The cellular activities governing net cytosolic Pi is not limited to Pi assimilation and recycling, but also includes exchange of Pi between cellular organelles. The vacuole constitutes most of the cell's volume and serves as the main reservoir for storing Pi [8]. Cells in the TZ displayed the highest cytosolic Pi concentration in the root apex, and these cells lack a developed central lytic vacuole [58]. Therefore, it is possible that high

cytosolic Pi concentrations in these cells are due to limited vacuolar stores. It would be interesting to monitor vacuolar Pi concentrations in the root developmental zones. The cpFLIPPi sensor used for cytosolic Pi measurements is not ideally suited to function in highly acidic environments such as the vacuolar lumen. Therefore, the existing sensor needs to be modified with pH resistant fluorophores and variants of the PiBP that have high FRET response in low pH. Simultaneous monitoring of vacuolar and cytosolic Pi would encompass almost the entire cellular Pi pool and thus provide a comprehensive picture of intracellular Pi dynamics.

The ability to monitor Pi within multiple cell compartments can be exploited to directly test the mode of action of numerous proteins and transporters that govern cellular and systemic Pi homeostasis. For example, PHT5;1 is reported to load Pi into the vacuole. Although *pht5;1* loss of function mutants do not have in any obvious growth defect [27], when Pi is resupplied to *pht5;1* mutants after a period of Pi deprivation, the plants show symptoms of Pi toxicity, possibly due to the inability to sequester excess Pi in the vacuole. It would be interesting to compare vacuolar and cytosolic Pi of *pht5;1* plants under Pi deprivation followed by Pi resupply. Thereafter, a comparative investigation of cytosolic and vacuolar Pi distribution in the root apex of *pht5;1*, wildtype, and a PHT5;1 over-expressing line will be informative to resolve any cell or developmental specificity.

In addition to resolving intracellular Pi homeostasis, subcellular Pi monitoring can also explain systemic Pi signaling processes. One of the major players that define systemic Pi homeostasis is the PHO1 protein. PHO1 is expressed in pericycle of the root

and it mediates Pi distribution to shoot tissues *via* xylem. A *pho1* loss of function mutation therefore impairs growth due to Pi deficiency in the shoot [243,244]. Interestingly, Rouached *et al*. [245] demonstrated that growth impairment of the *pho1* mutant is not a consequence of reduced shoot Pi; it is a secondary effect of genetic remodeling triggered by Pi stress. Consequently, an RNAi-mediated knock down of *PHO1* exhibits low shoot Pi without any growth defect. This observation has opened opportunities for resolving how plants maintain proper growth despite reduced internal Pi. Comparing subcellular Pi levels in the *pho1* mutant, RNAi knockdown, and wildtype may resolve the mechanism for uncoupling Pi deficiency from growth defect. This would greatly facilitate efforts to improve Pi use efficiency.

Since systemic Pi homeostasis is maintained by the interplay of other proteins and transporters in conjugation with PHO1 (*e.g.* PHO2, PHT1, PHR1), it is necessary to correlate and compare the roles played by the individual proteins. This study provides the tools and a guide for achieving this goal. For example, the root zone-specific Pi distribution pattern that correlates with root growth can be used as a reference to study the contributions of PHO1, PHO2, and PHT1 proteins toward balancing intracellular Pi and plant biomass. Furthermore, the ability to derive absolute Pi concentrations from FRET ratio data enables data sharing and comparison amongst research groups that focus on individual proteins, and creates a platform for a comprehensive study of systemic Pi homeostasis.

Pi transport across the chloroplast membrane plays a critical role in plant growth and development, since stromal Pi modulates photosynthesis and carbon allocation. My

work focused on the functional characterization of two Pi transporters, PHT2;1 and PHT4;4, the reside in the chloroplast inner envelope membrane. I hypothesized that both transporters contribute to fine-tuning of stromal Pi concentrations and I used ratiometric FRET analysis to determine the directionality of Pi transport by these transporters. My results showed that PHT2;1 imports Pi into the stroma and that PHT4;4 has no obvious contribution to chloroplast Pi transport. Additionally, results from the *pht2;1 tpt* double mutant suggest that the affected proteins import Pi into the chloroplast independently. Although ratiometric FRET revealed the directionality of Pi transport by PHT2;1, the biochemical mechanism of this transport activity remains unclear and requires further investigation.

FRET/eCFP ratio of the non-responsive control sensor cpFLIPPi-Null provides a potential clue for revealing the mechanism of Pi transport by PHT2;1. The *pht2;1* mutant expressing cpFLIPPi-Null shows significantly lower FRET/eCFP ratio (1.04 ± 0.04) than wildtype (1.37 ± 0.02). This decrease in FRET/eCFP ratio is not merely a secondary consequence of low stromal Pi because it does not occur in a *tpt* mutant or in a Pi-deprived wildtype. Therefore, the non-specific decrease in FRET may be a consequence of altered concentrations of the counter-ion used by PHT2;1 during Pi transport. This correlation of the *pht2;1* mutation to non-specific decrease in FRET provides a guide to test possible counter ions and therefore the biochemical mechanism of Pi transport by PHT2;1. For example, metabolites present in the chloroplast stroma could be tested in an *in vitro* FRET assay performed with purified cpFLIPPi-Null sensor protein. Thereafter, potential candidates selected from the *in vitro* assay could be tested with isolated

chloroplasts or proteoliposomes expressing the PHT2;1 protein and the cpFLIPPi-Null sensor. This approach could help resolve the physiological roles played by PHT2;1 and TPT in chloroplast Pi import.

Ratiometric FRET data failed to reveal any Pi accumulation defect in the *pht4;4* mutant chloroplast suggesting that PHT4;4 does not transport Pi into the chloroplast. However, *in vitro* transport assays involving heterologous systems have demonstrated that PHT4;4 transports both Pi and ascorbate. Miyaji *et al*. [240] described that PHT4;4 imports ascorbate into the chloroplast stroma, yet the biochemical mechanism of ascorbate transport remains unknown. Given this observation, it is plausible that PHT4;4 imports ascorbate from the cytosol in exchange for stromal Pi. Nevertheless, the *pht4;4* mutant fails to show a stromal Pi accumulation defect possibly due to the Pi concentration difference between wildtype and *pht4;4* being below the cpFLIPPi sensor's limit of detection. Artificially increasing ascorbate transport and investigating its effect on stromal Pi could test this possibility. If high concentrations of ascorbate are microinjected into the cytosol while subjecting the leaf to photooxidative stress, ascorbate transport across the chloroplast membrane should increase in a wild-type plant while be unaffected in a *pht4;4* mutant. Thus, it would be informative to compare chloroplast FRET ratios of wildtype and *pht4;4* mutants while microinjecting ascorbate. If PHT4;4 transports ascorbate in exchange for stromal Pi (antiport), increased ascorbate import should decrease stromal Pi. Failure to see a change in FRET ratio would confirm that PHT4;4 does not transport Pi, and mediates ascorbate transport by an alternate mechanism.

I have reported differences in stromal Pi levels as relative differences in FRET ratio instead of absolute Pi concentrations due to the lack of a suitable calibration. Since the chemical environments of cytosol and chloroplast stroma are expected to vary considerably, the Pi binding properties of the sensor may not be identical in these compartments. Hence, a single *in vivo* calibration of the sensor prepared in the cytosol cannot be used to convert stromal FRET ratios to Pi concentrations. Furthermore, a Pi calibration cannot be constructed by directly microinjecting Pi into the chloroplast due its small volume and to the lack of free Pi exchange across the chloroplast envelope. In case of the cytosol, the plasmodesmata allowed translocation of Pi from the injected cell to adjacent cells, thus achieving defined Pi concentrations in the injected cell. However, the restrictive boundary of the chloroplast envelope makes it impossible to emulate the absence of Pi inside the chloroplast. Therefore, obtaining a complete Pi calibration for the chloroplast stroma is not possible. Nonetheless, it may still be possible to estimate Pi concentrations inside a chloroplast if small volumes of Pi could be injected into a chloroplast in an epidermal peel from a leaf expressing the cpFLIPPi sensor. It would be interesting to inject a series of Pi concentrations then measure the change in FRET ratio of the injected chloroplast. The injected Pi concentration that matches the stromal Pi levels should fail to elicit a change in FRET. Although feasible, this approach would be slow, labor intensive, and require specialized microinjection capillaries ideally suited for chloroplasts.

REFERENCES

1. Kestenbaum B, Sampson JN, Rudser KD, Patterson DJ, Seliger SL, et al. (2005) Serum phosphate levels and mortality risk among people with chronic kidney disease. Journal of the American Society of Nephrology 16: 520-528.
2. Razzaque MS (2011) Phosphate toxicity: new insights into an old problem. Clinical science 120: 91-97.
3. Eddington H, Hoefield R, Sinha S, Chrysochou C, Lane B, et al. (2010) Serum phosphate and mortality in patients with chronic kidney disease. Clinical Journal of the American Society of Nephrology 5: 2251-2257.
4. Tonelli M, Sacks F, Pfeffer M, Gao Z, Curhan G (2005) Relation between serum phosphate level and cardiovascular event rate in people with coronary disease. Circulation 112: 2627-2633.
5. Foley RN, Collins AJ, Herzog CA, Ishani A, Kalra PA (2009) Serum phosphorus levels associate with coronary atherosclerosis in young adults. Journal of the American Society of Nephrology 20: 397-404.
6. Marschner H, Kirkby E, Cakmak I (1996) Effect of mineral nutritional status on shoot-root partitioning of photoassimilates and cycling of mineral nutrients. Journal of experimental botany 47: 1255-1263.
7. Schachtman DP, Reid RJ, Ayling SM (1998) Phosphorus uptake by plants: from soil to cell. Plant physiology 116: 447-453.
8. Bieleski R (1973) Phosphate pools, phosphate transport, and phosphate availability. Annual review of plant physiology 24: 225-252.

9. Holford I (1997) Soil phosphorus: its measurement, and its uptake by plants. Australian Journal of Soil Research 35: 227-240.

10. Ullrich-Eberius C, Novacky A, Van Bel A (1984) Phosphate uptake inLemna gibba G1: energetics and kinetics. Planta 161: 46-52.

11. Gross M (2010) Fears over phosphorus supplies. Current Biology 20: R386-R387.

12. Raghothama K (1999) Phosphate acquisition. Annual review of plant biology 50: 665-693.

13. Raghothama K, Karthikeyan A (2005) Phosphate acquisition. Root Physiology: from Gene to Function: Springer. pp. 37-49.

14. Rausch C, Bucher M (2002) Molecular mechanisms of phosphate transport in plants. Planta 216: 23-37.

15. Shin H, Shin HS, Dewbre GR, Harrison MJ (2004) Phosphate transport in Arabidopsis: Pht1; 1 and Pht1; 4 play a major role in phosphate acquisition from both low-and high-phosphate environments. The Plant Journal 39: 629-642.

16. Misson J, Thibaud M-C, Bechtold N, Raghothama K, Nussaume L (2004) Transcriptional regulation and functional properties of Arabidopsis Pht1; 4, a high affinity transporter contributing greatly to phosphate uptake in phosphate deprived plants. Plant molecular biology 55: 727-741.

17. Chiou TJ, Liu H, Harrison MJ (2001) The spatial expression patterns of a phosphate transporter (MtPT1) from Medicago truncatula indicate a role in phosphate transport at the root/soil interface. The Plant Journal 25: 281-293.

18. Furihata T, Suzuki M, Sakurai H (1992) Kinetic characterization of two phosphate uptake systems with different affinities in suspension-cultured Catharanthus roseus protoplasts. Plant and Cell Physiology 33: 1151-1157.

19. Nakanishi TM, Thibaud M-C (2014) Phosphate import in plants: focus on the PHT1 transporters. Evolution of transporters in plants: 235.

20. Mudge SR, Rae AL, Diatloff E, Smith FW (2002) Expression analysis suggests novel roles for members of the Pht1 family of phosphate transporters in Arabidopsis. The Plant Journal 31: 341-353.

21. Nussaume L, Kanno S, Javot H, Marin E, Nakanishi TM, et al. (2011) Phosphate Import in Plants: Focus on the PHT1 Transporters. Frontiers in Plant Science 2.

22. González E, Solano R, Rubio V, Leyva A, Paz-Ares J (2005) PHOSPHATE TRANSPORTER TRAFFIC FACILITATOR1 is a plant-specific SEC12-related protein that enables the endoplasmic reticulum exit of a high-affinity phosphate transporter in Arabidopsis. The Plant Cell 17: 3500-3512.

23. Mimura T (1999) Regulation of phosphate transport and homeostasis in plant cells. International Review of Cytology 191: 149-200.

24. Poirier Y, Bucher M (2002) Phosphate transport and homeostasis in Arabidopsis. The Arabidopsis Book: e0024.

25. Mitsukawa N, Okumura S, Shibata D (1997) High-affinity phosphate transporter genes of Arabidopsis thaliana. Plant Nutrition for Sustainable Food Production and Environment: Springer. pp. 187-190.

26. Okumura S, Mitsukawa N, Shirano Y, Shibata D (1998) Phosphate transporter gene family of Arabidopsis thaliana. DNA Research 5: 261-269.

27. Liu T-Y, Huang T-K, Yang S-Y, Hong Y-T, Huang S-M, et al. (2016) Identification of plant vacuolar transporters mediating phosphate storage. Nature communications 7.

28. Kiiskinen M, Korhonen M, Kangasjärvi J (1997) Isolation and characterization of cDNA for a plant mitochondrial phosphate translocator (Mpt1): ozone stress induces Mpt1 mRNA accumulation in birch (Betula pendula Roth). Plant molecular biology 35: 271-279.

29. Sharkey TD (1985) Photosynthesis in intact leaves of C3 plants: physics, physiology and rate limitations. The Botanical Review 51: 53-105.

30. Flügge U-I (1999) Phosphate translocators in plastids. Annual review of plant biology 50: 27-45.

31. Flugge U-l, Heldt HW (1991) Metabolite translocators of the chloroplast envelope. Annual review of plant biology 42: 129-144.

32. LEE RB, Ratcliffe R (1993) Subcellular distribution of inorganic phosphate, and levels of nucleoside triphosphate, in mature maize roots at low external phosphate concentrations: measurements with 31P-NMR. Journal of Experimental Botany 44: 587-598.

33. Del Pozo JC, Allona I, Rubio V, Leyva A, De La Peña A, et al. (1999) A type 5 acid phosphatase gene from Arabidopsis thaliana is induced by phosphate starvation

and by some other types of phosphate mobilising/oxidative stress conditions. The Plant Journal 19: 579-589.

34. Duff SM, Sarath G, Plaxton WC (1994) The role of acid phosphatases in plant phosphorus metabolism. Physiologia plantarum 90: 791-800.

35. Köck M, Theierl K, Stenzel I, Glund K (1998) Extracellular administration of phosphate-sequestering metabolites induces ribonucleases in cultured tomato cells. Planta 204: 404-407.

36. Trull MC, Deikman J (1998) An Arabidopsis mutant missing one acid phosphatase isoform. Planta 206: 544-550.

37. Richardson AE, Hadobas PA, Hayes JE (2001) Extracellular secretion of Aspergillus phytase from Arabidopsis roots enables plants to obtain phosphorus from phytate. The Plant Journal 25: 641-649.

38. Narang RA, Bruene A, Altmann T (2000) Analysis of phosphate acquisition efficiency in different Arabidopsis accessions. Plant Physiology 124: 1786-1799.

39. Duff SM, Moorhead GB, Lefebvre DD, Plaxton WC (1989) Phosphate starvation induciblebypasses' of adenylate and phosphate dependent glycolytic enzymes in Brassica nigra suspension cells. Plant Physiology 90: 1275-1278.

40. Theodorou ME, Plaxton WC (1993) Metabolic adaptations of plant respiration to nutritional phosphate deprivation. Plant physiology 101: 339-344.

41. Plaxton WC, Carswell MC (1999) Metabolic aspects of the phosphate starvation response in plants. Plant responses to environmental stresses: from phytohormones to genome reorganization Marcel Dekker, New York: 349-372.

42. Essigmann B, Güler S, Narang RA, Linke D, Benning C (1998) Phosphate availability affects the thylakoid lipid composition and the expression of SQD1, a gene required for sulfolipid biosynthesis in Arabidopsis thaliana. Proceedings of the National Academy of Sciences 95: 1950-1955.

43. Härtel H, Dörmann P, Benning C (2000) DGD1-independent biosynthesis of extraplastidic galactolipids after phosphate deprivation in Arabidopsis. Proceedings of the National Academy of Sciences 97: 10649-10654.

44. Rubio V, Linhares F, Solano R, Martín AC, Iglesias J, et al. (2001) A conserved MYB transcription factor involved in phosphate starvation signaling both in vascular plants and in unicellular algae. Genes & development 15: 2122-2133.

45. Pant BD, Buhtz A, Kehr J, Scheible WR (2008) MicroRNA399 is a long-distance signal for the regulation of plant phosphate homeostasis. The Plant Journal 53: 731-738.

46. Lin W-Y, Huang T-K, Leong SJ, Chiou T-J (2014) Long-distance call from phosphate: systemic regulation of phosphate starvation responses. Journal of experimental botany 65: 1817-1827.

47. Lopez-Arredondo DL, Leyva-González MA, González-Morales SI, López-Bucio J, Herrera-Estrella L (2014) Phosphate nutrition: improving low-phosphate tolerance in crops. Annual review of plant biology 65: 95-123.

48. Svistoonoff S, Creff A, Reymond M, Sigoillot-Claude C, Ricaud L, et al. (2007) Root tip contact with low-phosphate media reprograms plant root architecture. Nature genetics 39: 792-796.

49. Ticconi CA, Delatorre CA, Lahner B, Salt DE, Abel S (2004) Arabidopsis pdr2 reveals a phosphate-sensitive checkpoint in root development. The Plant Journal 37: 801-814.

50. Rouached H, Arpat AB, Poirier Y (2010) Regulation of phosphate starvation responses in plants: signaling players and cross-talks. Molecular Plant 3: 288-299.

51. Duan K, Yi K, Dang L, Huang H, Wu W, et al. (2008) Characterization of a sub-family of Arabidopsis genes with the SPX domain reveals their diverse functions in plant tolerance to phosphorus starvation. The Plant Journal 54: 965-975.

52. Puga MI, Mateos I, Charukesi R, Wang Z, Franco-Zorrilla JM, et al. (2014) SPX1 is a phosphate-dependent inhibitor of PHOSPHATE STARVATION RESPONSE 1 in Arabidopsis. Proceedings of the National Academy of Sciences 111: 14947-14952.

53. Gutjahr C, Paszkowski U (2014) Multiple control levels of root system remodeling in arbuscular mycorrhizal symbiosis. Induced plant responses to microbes and insects: 320.

54. Harrison MJ, Dewbre GR, Liu J (2002) A phosphate transporter from Medicago truncatula involved in the acquisition of phosphate released by arbuscular mycorrhizal fungi. The Plant Cell 14: 2413-2429.

55. Rausch C, Daram P, Brunner S, Jansa J, Laloi M, et al. (2001) A phosphate transporter expressed in arbuscule-containing cells in potato. Nature 414: 462-470.

56. Walder F, Niemann H, Natarajan M, Lehmann MF, Boller T, et al. (2012) Mycorrhizal networks: common goods of plants shared under unequal terms of trade. Plant physiology 159: 789-797.

57. Ishikawa H, Evans ML (1995) Specialized zones of development in roots. Plant Physiology 109: 725.

58. Baluška F, Barlow PW, Kubica Š (1994) Importance of the post-mitotic isodiametric growth (PIG) region for growth and development of roots. Plant and Soil 167: 31-41.

59. Doerner P, Joergensen J-E, You R, Steppuhn J, Lamb C (1996) Control of root growth and development by cyclin expression. Nature 380: 520-523.

60. Colón-Carmona A, You R, Haimovitch-Gal T, Doerner P (1999) Spatio-temporal analysis of mitotic activity with a labile cyclin–GUS fusion protein. The Plant Journal 20: 503-508.

61. Perilli S, Di Mambro R, Sabatini S (2012) Growth and development of the root apical meristem. Current opinion in plant biology 15: 17-23.

62. Baluška F, Volkmann D, Barlow PW (2001) A polarity crossroad in the transition growth zone of maize root apices: cytoskeletal and developmental implications. Journal of Plant Growth Regulation 20: 170-181.

63. Baluska F, Volkmann D, Barlow PW (1996) Specialized zones of development in roots: view from the cellular level. Plant Physiology 112: 3.

64. Joubes J, Chevalier C (2000) Endoreduplication in higher plants. The Plant Cell Cycle: Springer. pp. 191-201.

65. Ioio RD, Nakamura K, Moubayidin L, Perilli S, Taniguchi M, et al. (2008) A genetic framework for the control of cell division and differentiation in the root meristem. Science 322: 1380-1384.

66. Le J, Vandenbussche F, Van Der Straeten D, Verbelen JP (2004) Position and cell type-dependent microtubule reorientation characterizes the early response of the Arabidopsis root epidermis to ethylene. Physiologia Plantarum 121: 513-519.

67. Bichet A, Desnos T, Turner S, Grandjean O, Höfte H (2001) BOTERO1 is required for normal orientation of cortical microtubules and anisotropic cell expansion in Arabidopsis. The Plant Journal 25: 137-148.

68. Stadler R, Wright KM, Lauterbach C, Amon G, Gahrtz M, et al. (2005) Expression of GFP-fusions in Arabidopsis companion cells reveals non-specific protein trafficking into sieve elements and identifies a novel post-phloem domain in roots. The Plant Journal 41: 319-331.

69. Ludevid D, Höfte H, Himelblau E, Chrispeels MJ (1992) The expression pattern of the tonoplast intrinsic protein γ-TIP in Arabidopsis thaliana is correlated with cell enlargement. Plant Physiology 100: 1633-1639.

70. Vissenberg K, Martinez-Vilchez IM, Verbelen J-P, Miller JG, Fry SC (2000) In vivo colocalization of xyloglucan endotransglycosylase activity and its donor substrate in the elongation zone of Arabidopsis roots. The Plant Cell 12: 1229-1237.

71. Lee D-K, Ahn JH, Song S-K, Do Choi Y, Lee JS (2003) Expression of an expansin gene is correlated with root elongation in soybean. Plant Physiology 131: 985-997.

72. Schindelman G, Morikami A, Jung J, Baskin TI, Carpita NC, et al. (2001) COBRA encodes a putative GPI-anchored protein, which is polarly localized and necessary for oriented cell expansion in Arabidopsis. Genes & development 15: 1115-1127.

73. Willats WG, Knox JP (1996) A role for arabinogalactan-proteins in plant cell expansion: evidence from studies on the interaction of β-glucosyl Yariv reagent with seedlings of Arabidopsis thaliana. The Plant Journal 9: 919-925.

74. Van Hengel AJ, Roberts K (2002) Fucosylated arabinogalactan-proteins are required for full root cell elongation in Arabidopsis. The Plant Journal 32: 105-113.

75. Kerstens S, Verbelen J-P (2003) Cellulose orientation at the surface of the Arabidopsis seedling. Implications for the biomechanics in plant development. Journal of structural biology 144: 262-270.

76. De Cnodder T, Vissenberg K, Van Der Straeten D, Verbelen JP (2005) Regulation of cell length in the Arabidopsis thaliana root by the ethylene precursor 1-aminocyclopropane-1-carboxylic acid: a matter of apoplastic reactions. New Phytologist 168: 541-550.

77. Duckett CM, Oparka KJ, Prior DA, Dolan L, Roberts K (1994) Dye-coupling in the root epidermis of Arabidopsis is progressively reduced during development. Development 120: 3247-3255.

78. Dinkelaker B, Hengeler C, Marschner H (1995) Distribution and function of proteoid roots and other root clusters. Botanica Acta 108: 183-200.

79. Carswell C, Grant BR, Theodorou ME, Harris J, Niere JO, et al. (1996) The fungicide phosphonate disrupts the phosphate-starvation response in Brassica nigra seedlings. Plant Physiology 110: 105-110.

80. KIM HJ, Lynch JP, Brown KM (2008) Ethylene insensitivity impedes a subset of responses to phosphorus deficiency in tomato and petunia. Plant, cell & environment 31: 1744-1755.

81. Jin J, Tang C, Armstrong R, Sale P (2012) Phosphorus supply enhances the response of legumes to elevated CO2 (FACE) in a phosphorus-deficient vertisol. Plant and Soil 358: 91-104.

82. Bates T, Lynch J (1996) Stimulation of root hair elongation in Arabidopsis thaliana by low phosphorus availability. Plant, Cell & Environment 19: 529-538.

83. Williamson LC, Ribrioux SP, Fitter AH, Leyser HO (2001) Phosphate availability regulates root system architecture in Arabidopsis. Plant Physiology 126: 875-882.

84. Sánchez-Calderón L, López-Bucio J, Chacón-López A, Gutiérrez-Ortega A, Hernández-Abreu E, et al. (2006) Characterization of low phosphorus insensitive mutants reveals a crosstalk between low phosphorus-induced determinate root development and the activation of genes involved in the adaptation of Arabidopsis to phosphorus deficiency. Plant physiology 140: 879-889.

85. Sánchez-Calderón L, López-Bucio J, Chacón-López A, Cruz-Ramírez A, Nieto-Jacobo F, et al. (2005) Phosphate starvation induces a determinate developmental program in the roots of Arabidopsis thaliana. Plant and Cell Physiology 46: 174-184.

86. Lynch JP, Ho MD (2005) Rhizoeconomics: carbon costs of phosphorus acquisition. Plant and Soil 269: 45-56.

87. Zhu J, Kaeppler SM, Lynch JP (2005) Mapping of QTL controlling root hair length in maize (Zea mays L.) under phosphorus deficiency. Plant and Soil 270: 299-310.

88. Tyburski J, Dunajska-Ordak K, Skorupa M, Tretyn A (2012) Role of ascorbate in the regulation of the Arabidopsis thaliana root growth by phosphate availability. Journal of Botany 2012.

89. Nacry P, Canivenc G, Muller B, Azmi A, Van Onckelen H, et al. (2005) A role for auxin redistribution in the responses of the root system architecture to phosphate starvation in Arabidopsis. Plant Physiology 138: 2061-2074.

90. Leavitt RG (1904) Trichomes of the root in vascular cryptogams and angiosperms: Soc. of Natural History.

91. Schiefelbein JW (2000) Constructing a plant cell. The genetic control of root hair development. Plant Physiology 124: 1525-1531.

92. Zhang YJ, Lynch JP, Brown KM (2003) Ethylene and phosphorus availability have interacting yet distinct effects on root hair development. Journal of Experimental Botany 54: 2351-2361.

93. Ma Z, Bielenberg D, Brown K, Lynch J (2001) Regulation of root hair density by phosphorus availability in Arabidopsis thaliana. Plant, Cell & Environment 24: 459-467.

94. Foehse D, Jungk A (1983) Influence of phosphate and nitrate supply on root hair formation of rape, spinach and tomato plants. Plant and soil 74: 359-368.

95. Jain A, Poling MD, Karthikeyan AS, Blakeslee JJ, Peer WA, et al. (2007) Differential effects of sucrose and auxin on localized phosphate deficiency-induced modulation of different traits of root system architecture in Arabidopsis. Plant Physiology 144: 232-247.

96. Péret B, Clément M, Nussaume L, Desnos T (2011) Root developmental adaptation to phosphate starvation: better safe than sorry. Trends in plant science 16: 442-450.

97. Achard P, Gusti A, Cheminant S, Alioua M, Dhondt S, et al. (2009) Gibberellin signaling controls cell proliferation rate in Arabidopsis. Current biology 19: 1188-1193.

98. Mitchum MG, Yamaguchi S, Hanada A, Kuwahara A, Yoshioka Y, et al. (2006) Distinct and overlapping roles of two gibberellin 3-oxidases in Arabidopsis development. The Plant Journal 45: 804-818.

99. Shani E, Weinstain R, Zhang Y, Castillejo C, Kaiserli E, et al. (2013) Gibberellins accumulate in the elongating endodermal cells of Arabidopsis root. Proceedings of the National Academy of Sciences 110: 4834-4839.

100. Jiang C, Gao X, Liao L, Harberd NP, Fu X (2007) Phosphate starvation root architecture and anthocyanin accumulation responses are modulated by the gibberellin-DELLA signaling pathway in Arabidopsis. Plant physiology 145: 1460-1470.

101. Wu A, Gong L, Chen X, Wang J (2014) Interactions between nitric oxide, gibberellic acid, and phosphorus regulate primary root growth in Arabidopsis. Biologia plantarum 58: 335-340.

102. Devaiah BN, Madhuvanthi R, Karthikeyan AS, Raghothama KG (2009) Phosphate starvation responses and gibberellic acid biosynthesis are regulated by the MYB62 transcription factor in Arabidopsis. Molecular Plant 2: 43-58.

103. Roudier F, Fedorova E, Lebris M, Lecomte P, Györgyey J, et al. (2003) The Medicago species A2-type cyclin is auxin regulated and involved in meristem formation but dispensable for endoreduplication-associated developmental programs. Plant physiology 131: 1091-1103.

104. Růžička K, Ljung K, Vanneste S, Podhorská R, Beeckman T, et al. (2007) Ethylene regulates root growth through effects on auxin biosynthesis and transport-dependent auxin distribution. The Plant Cell 19: 2197-2212.

105. Wildwater M, Campilho A, Perez-Perez JM, Heidstra R, Blilou I, et al. (2005) The RETINOBLASTOMA-RELATED gene regulates stem cell maintenance in Arabidopsis roots. Cell 123: 1337-1349.

106. López-Bucio J, Hernandez-Abreu E, Sanchez-Calderon L, Nieto-Jacobo MF, Simpson J, et al. (2002) Phosphate availability alters architecture and causes

changes in hormone sensitivity in the Arabidopsis root system. Plant physiology 129: 244-256.

107. Riou-Khamlichi C, Huntley R, Jacqmard A, Murray JA (1999) Cytokinin activation of Arabidopsis cell division through a D-type cyclin. Science 283: 1541-1544.

108. Beemster GT, Baskin TI (2000) STUNTED PLANT 1 mediates effects of cytokinin, but not of auxin, on cell division and expansion in the root of Arabidopsis. Plant Physiology 124: 1718-1727.

109. Boudolf V, Lammens T, Boruc J, Van Leene J, Van Den Daele H, et al. (2009) CDKB1; 1 forms a functional complex with CYCA2; 3 to suppress endocycle onset. Plant Physiology 150: 1482-1493.

110. Vanstraelen M, Baloban M, Da Ines O, Cultrone A, Lammens T, et al. (2009) APC/CCCS52A complexes control meristem maintenance in the Arabidopsis root. Proceedings of the National Academy of Sciences 106: 11806-11811.

111. Bishopp A, Lehesranta S, Vatén A, Help H, El-Showk S, et al. (2011) Phloem-transported cytokinin regulates polar auxin transport and maintains vascular pattern in the root meristem. Current Biology 21: 927-932.

112. Mockaitis K, Estelle M (2008) Auxin receptors and plant development: a new signaling paradigm. Annual review of cell and developmental biology 24: 55-80.

113. Aloni R, Aloni E, Langhans M, Ullrich C (2006) Role of cytokinin and auxin in shaping root architecture: regulating vascular differentiation, lateral root initiation, root apical dominance and root gravitropism. Annals of botany 97: 883-893.

114. Martín AC, Del Pozo JC, Iglesias J, Rubio V, Solano R, et al. (2000) Influence of cytokinins on the expression of phosphate starvation responsive genes in Arabidopsis. The Plant Journal 24: 559-567.

115. Horgan J, Wareing P (1980) Cytokinins and the growth responses of seedlings of Betula pendula Roth. and Acer pseudoplatanus L. to nitrogen and phosphorus deficiency. Journal of Experimental Botany 31: 525-532.

116. Kuiper D, Schuit J, Kuiper PJ (1989) Effects of internal and external cytokinin concentrations on root growth and shoot to root ratio of Plantago major ssp pleiosperma at different nutrient conditions. Structural and Functional Aspects of Transport in Roots: Springer. pp. 183-188.

117. Franco-Zorrilla JM, Martin AC, Solano R, Rubio V, Leyva A, et al. (2002) Mutations at CRE1 impair cytokinin-induced repression of phosphate starvation responses in Arabidopsis. The Plant Journal 32: 353-360.

118. Ortega-Martínez O, Pernas M, Carol RJ, Dolan L (2007) Ethylene modulates stem cell division in the Arabidopsis thaliana root. Science 317: 507-510.

119. Swarup R, Perry P, Hagenbeek D, Van Der Straeten D, Beemster GT, et al. (2007) Ethylene upregulates auxin biosynthesis in Arabidopsis seedlings to enhance inhibition of root cell elongation. The Plant Cell 19: 2186-2196.

120. Borch K, Bouma T, Lynch J, Brown K (1999) Ethylene: a regulator of root architectural responses to soil phosphorus availability. Plant, Cell & Environment 22: 425-431.

121. Neuhaus H, Emes M (2000) Nonphotosynthetic metabolism in plastids. Annual review of plant biology 51: 111-140.

122. Lopez-Juez E, Pyke KA (2004) Plastids unleashed: their development and their integration in plant development. International Journal of Developmental Biology 49: 557-577.

123. Knappe S, Flügge U-I, Fischer K (2003) Analysis of the plastidic phosphate translocator gene family in Arabidopsis and identification of new phosphate translocator-homologous transporters, classified by their putative substrate-binding site. Plant Physiology 131: 1178-1190.

124. Fischer K, Kammerer B, Gutensohn M, Arbinger B, Weber A, et al. (1997) A new class of plastidic phosphate translocators: a putative link between primary and secondary metabolism by the phosphoenolpyruvate/phosphate antiporter. The Plant Cell 9: 453-462.

125. Kammerer B, Fischer K, Hilpert B, Schubert S, Gutensohn M, et al. (1998) Molecular characterization of a carbon transporter in plastids from heterotrophic tissues: the glucose 6-phosphate/phosphate antiporter. The Plant Cell 10: 105-117.

126. Eicks M, Maurino V, Knappe S, Flügge U-I, Fischer K (2002) The plastidic pentose phosphate translocator represents a link between the cytosolic and the plastidic pentose phosphate pathways in plants. Plant Physiology 128: 512-522.

127. SHEU-HWA CS, Lewis D, Walker D (1975) Stimulation of photosynthetic starch formation by sequestration of cytoplasmic orthophosphate. New phytologist 74: 383-392.

128. Walters RG, Ibrahim DG, Horton P, Kruger NJ (2004) A mutant of Arabidopsis lacking the triose-phosphate/phosphate translocator reveals metabolic regulation of starch breakdown in the light. Plant Physiology 135: 891-906.

129. Ballicora MA, Iglesias AA, Preiss J (2004) ADP-glucose pyrophosphorylase: a regulatory enzyme for plant starch synthesis. Photosynthesis Research 79: 1-24.

130. Nielsen TH, Krapp A, Röper-Schwarz U, Stitt M (1998) The sugar-mediated regulation of genes encoding the small subunit of Rubisco and the regulatory subunit of ADP glucose pyrophosphorylase is modified by phosphate and nitrogen. Plant, Cell & Environment 21: 443-454.

131. Preiss J (1982) Regulation of the biosynthesis and degradation of starch. Annual Review of Plant Physiology 33: 431-454.

132. Riesmeier JW, Flügge U, Schulz B, Heineke D, Heldt H-W, et al. (1993) Antisense repression of the chloroplast triose phosphate translocator affects carbon partitioning in transgenic potato plants. Proceedings of the National Academy of Sciences 90: 6160-6164.

133. Schneider A, Häusler RE, Kolukisaoglu Ü, Kunze R, Van Der Graaff E, et al. (2002) An Arabidopsis thaliana knock-out mutant of the chloroplast triose phosphate/phosphate translocator is severely compromised only when starch

synthesis, but not starch mobilisation is abolished. The Plant Journal 32: 685-699.

134. Pavón LR, Lundh F, Lundin B, Mishra A, Persson BL, et al. (2008) Arabidopsis ANTR1 Is a thylakoid Na+-dependent phosphate transporter functional characterization in escherichia coli. Journal of Biological Chemistry 283: 13520-13527.

135. Guo B, Jin Y, Wussler C, Blancaflor E, Motes C, et al. (2008) Functional analysis of the Arabidopsis PHT4 family of intracellular phosphate transporters. New Phytologist 177: 889-898.

136. Daram P, Brunner S, Rausch C, Steiner C, Amrhein N, et al. (1999) Pht2; 1 encodes a low-affinity phosphate transporter from Arabidopsis. The Plant Cell 11: 2153-2166.

137. Versaw WK, Harrison MJ (2002) A chloroplast phosphate transporter, PHT2; 1, influences allocation of phosphate within the plant and phosphate-starvation responses. The Plant Cell 14: 1751-1766.

138. Irigoyen S, Karlsson PM, Kuruvilla J, Spetea C, Versaw WK (2011) The sink-specific plastidic phosphate transporter PHT4; 2 influences starch accumulation and leaf size in Arabidopsis. Plant physiology 157: 1765-1777.

139. Shachar-Hill Y, Pfeffer PE (1996) Nuclear magnetic resonance in plant biology: JSTOR.

140. Vidal G, Gallis J-L, Dufour S, Canioni P (1997) NMR studies of inorganic phosphate compartmentation in the isolated rat liver during acidic perfusion. Archives of biochemistry and biophysics 337: 317-325.

141. Smart KE, Smith JAC, Kilburn MR, Martin BG, Hawes C, et al. (2010) High-resolution elemental localization in vacuolate plant cells by nanoscale secondary ion mass spectrometry. The Plant Journal 63: 870-879.

142. Moore KL, Chen Y, Meene AM, Hughes L, Liu W, et al. (2014) Combined NanoSIMS and synchrotron X-ray fluorescence reveal distinct cellular and subcellular distribution patterns of trace elements in rice tissues. New Phytologist 201: 104-115.

143. Kanno S, Yamawaki M, Ishibashi H, Kobayashi NI, Hirose A, et al. (2012) Development of real-time radioisotope imaging systems for plant nutrient uptake studies. Philosophical Transactions of the Royal Society of London B: Biological Sciences 367: 1501-1508.

144. Gjetting SK, Schulz A, Fuglsang AT (2013) Perspectives for using genetically encoded fluorescent biosensors in plants.

145. De Lorimier RM, Smith JJ, Dwyer MA, Looger LL, Sali KM, et al. (2002) Construction of a fluorescent biosensor family. Protein Science 11: 2655-2675.

146. Frommer WB, Davidson MW, Campbell RE (2009) Genetically encoded biosensors based on engineered fluorescent proteins. Chemical Society Reviews 38: 2833-2841.

147. Okumoto S (2014) Quantitative imaging approaches for small-molecule measurements using FRET sensors in plants. Plant Metabolism: Methods and Protocols: 55-64.

148. Allen GJ, Kwak JM, Chu SP, Llopis J, Tsien RY, et al. (1999) Cameleon calcium indicator reports cytoplasmic calcium dynamics in Arabidopsis guard cells. The Plant Journal 19: 735-747.

149. Deuschle K, Chaudhuri B, Okumoto S, Lager I, Lalonde S, et al. (2006) Rapid metabolism of glucose detected with FRET glucose nanosensors in epidermal cells and intact roots of Arabidopsis RNA-silencing mutants. The Plant Cell 18: 2314-2325.

150. Gu H, Lalonde S, Okumoto S, Looger LL, Scharff-Poulsen AM, et al. (2006) A novel analytical method for in vivo phosphate tracking. FEBS letters 580: 5885-5893.

151. Mukherjee P, Banerjee S, Wheeler A, Ratliff LA, Irigoyen S, et al. (2015) Live imaging of inorganic phosphate in plants with cellular and subcellular resolution. Plant physiology 167: 628-638.

152. Berndt T, Kumar R (2009) Novel mechanisms in the regulation of phosphorus homeostasis. Physiology (Bethesda) 24: 17-25.

153. Biber J, Hernando N, Forster I (2013) Phosphate transporters and their function. Annu Rev Physiol 75: 535-550.

154. Okumoto S, Jones A, Frommer WB (2012) Quantitative Imaging with Fluorescent Biosensors. Annual Review of Plant Biology 63: 663-706.

155. Miyawaki A, Llopis J, Heim R, McCaffery JM, Adams JA, et al. (1997) Fluorescent indicators for Ca2+based on green fluorescent proteins and calmodulin. Nature 388: 882-887.

156. Romoser VA, Hinkle PM, Persechini A (1997) Detection in living cells of Ca2+-dependent changes in the fluorescence emission of an indicator composed of two green fluorescent protein variants linked by a calmodulin-binding sequence A new class of fluorescent indicators. Journal of biological chemistry 272: 13270-13274.

157. Hum JM, Siegel AP, Pavalko FM, Day RN (2012) Monitoring biosensor activity in living cells with fluorescence lifetime imaging microscopy. International journal of molecular sciences 13: 14385-14400.

158. Miyawaki A (2011) Development of probes for cellular functions using fluorescent proteins and fluorescence resonance energy transfer. Annual review of biochemistry 80: 357-373.

159. Nagai T, Ibata K, Park ES, Kubota M, Mikoshiba K, et al. (2002) A variant of yellow fluorescent protein with fast and efficient maturation for cell-biological applications. Nature biotechnology 20: 87-90.

160. Nagai T, Yamada S, Tominaga T, Ichikawa M, Miyawaki A (2004) Expanded dynamic range of fluorescent indicators for Ca2+ by circularly permuted yellow fluorescent proteins. Proceedings of the National Academy of Sciences of the United States of America 101: 10554-10559.

161. Fukushige T, Goszczynski B, Yan J, McGhee JD (2005) Transcriptional control and patterning of the pho-1 gene, an essential acid phosphatase expressed in the C. elegans intestine. Developmental biology 279: 446-461.

162. Beh CT, Ferrari DC, Chung MA, McGhee JD (1991) An acid phosphatase as a biochemical marker for intestinal development in the nematode Caenorhabditis elegans. Developmental biology 147: 133-143.

163. Kormish JD, McGhee JD (2005) The C. elegans lethal gut-obstructed gob-1 gene is trehalose-6-phosphate phosphatase. Developmental biology 287: 35-47.

164. Legouis R, Gansmuller A, Sookhareea S, Bosher JM, Baillie DL, et al. (2000) LET-413 is a basolateral protein required for the assembly of adherens junctions in Caenorhabditis elegans. Nature cell biology 2: 415-422.

165. Roszik J, Lisboa D, Szöllősi J, Vereb G (2009) Evaluation of intensity-based ratiometric FRET in image cytometry—Approaches and a software solution. Cytometry Part A 75: 761-767.

166. Tadross MR, Park SA, Veeramani B, Yue DT (2009) Robust approaches to quantitative ratiometric FRET imaging of CFP/YFP fluorophores under confocal microscopy. Journal of microscopy 233: 192-204.

167. Wallrabe H, Periasamy A (2005) Imaging protein molecules using FRET and FLIM microscopy. Current opinion in biotechnology 16: 19-27.

168. Gordon GW, Berry G, Liang XH, Levine B, Herman B (1998) Quantitative fluorescence resonance energy transfer measurements using fluorescence microscopy. Biophysical journal 74: 2702-2713.

169. Karpova T, Baumann C, He L, Wu X, Grammer A, et al. (2003) Fluorescence resonance energy transfer from cyan to yellow fluorescent protein detected by acceptor photobleaching using confocal microscopy and a single laser. Journal of microscopy 209: 56-70.

170. Wadsworth WG, Riddle DL (1989) Developmental regulation of energy metabolism in Caenorhabditis elegans. Developmental biology 132: 167-173.

171. Van Heyningen WE (1935) The inhibition of respiration by cyanide. Biochemical Journal 29: 2036.

172. Vanfleteren JR, De Vreese A (1996) Rate of aerobic metabolism and superoxide production rate potential in the nematode Caenorhabditis elegans. Journal of Experimental Zoology 274: 93-100.

173. De Cuyper C, Vanfleteren J (1982) Oxygen consumption during development and aging of the nematode Caenorhabditis elegans. Comparative Biochemistry and Physiology Part A: Physiology 73: 283-289.

174. Zaborin A, Romanowski K, Gerdes S, Holbrook C, Lepine F, et al. (2009) Red death in Caenorhabditis elegans caused by Pseudomonas aeruginosa PAO1. Proceedings of the National Academy of Sciences 106: 6327-6332.

175. Babu P, Brenner S (1981) Spectrum of 32 P-induced mutants of Caenorbabditis elegans. Mutation Research/Fundamental and Molecular Mechanisms of Mutagenesis 82: 269-273.

176. Sulston J, Brenner S (1974) The DNA of Caenorhabditis elegans. Genetics 77: 95-104.

177. Lindsley JE, Rutter J (2004) Nutrient sensing and metabolic decisions. Comparative Biochemistry and Physiology Part B: Biochemistry and Molecular Biology 139: 543-559.

178. Finn PF, Dice JF (2006) Proteolytic and lipolytic responses to starvation. Nutrition 22: 830-844.

179. Lum JJ, DeBerardinis RJ, Thompson CB (2005) Autophagy in metazoans: cell survival in the land of plenty. Nature Reviews Molecular Cell Biology 6: 439-448.

180. Levine B, Kroemer G (2008) Autophagy in the pathogenesis of disease. Cell 132: 27-42.

181. ZAKRZEWSKA J, ŽIŽIĆ M, ŽIVIĆ M (2005) The effect of anoxia on PolyP content of Phycomyces blakesleeanus mycelium studied by 31P NMR spectroscopy. Annals of the New York Academy of Sciences 1048: 482-486.

182. Schnabel H, Schnabel R (1990) An organ-specific differentiation gene, pha-1, from Caenorhabditis elegans. Science 250: 686-688.

183. Hodgkin J, Horvitz HR, Brenner S (1979) Nondisjunction mutants of the nematode Caenorhabditis elegans. Genetics 91: 67-94.

184. Edwards SL, Charlie NK, Milfort MC, Brown BS, Gravlin CN, et al. (2008) A novel molecular solution for ultraviolet light detection in Caenorhabditis elegans. PLoS biology 6: e198.

185. Gettner SN, Kenyon C, Reichardt LF (1995) Characterization of beta pat-3 heterodimers, a family of essential integrin receptors in C. elegans. The Journal of Cell Biology 129: 1127-1141.

186. Fire A, Harrison SW, Dixon D (1990) A modular set of lacZ fusion vectors for studying gene expression in Caenorhabditis elegans. Gene 93: 189-198.

187. LeBoeuf B, Gruninger TR, Garcia LR (2007) Food deprivation attenuates seizures through CaMKII and EAG K+ channels. PLoS genetics 3.

188. Mello C, Fire A (1995) DNA transformation. Methods Cell Biol 48: 451-482.

189. Anderson P (1995) Mutagenesis. Methods Cell Biol 48: 31-58.

190. Kim E, Sun L, Gabel CV, Fang-Yen C (2013) Long-term imaging of Caenorhabditis elegans using nanoparticle-mediated immobilization. PloS one 8: e53419.

191. Altun ZF, Chen B, Wang ZW, Hall DH (2009) High resolution map of Caenorhabditis elegans gap junction proteins. Developmental Dynamics 238: 1936-1950.

192. Jones AM, Grossmann G, Danielson JA, Sosso D, Chen LQ, et al. (2013) In vivo biochemistry: applications for small molecule biosensors in plant biology. Curr Opin Plant Biol 16: 389-395.

193. Jones AM, Danielson JA, Manojkumar SN, Lanquar V, Grossmann G, et al. (2014) Abscisic acid dynamics in roots detected with genetically encoded FRET sensors. Elife 3: e01741.

194. Waadt R, Hitomi K, Nishimura N, Hitomi C, Adams SR, et al. (2014) FRET-based reporters for the direct visualization of abscisic acid concentration changes and distribution in Arabidopsis. Elife 3: e01739.

195. Krebs M, Held K, Binder A, Hashimoto K, Den Herder G, et al. (2012) FRET-based genetically encoded sensors allow high-resolution live cell imaging of Ca(2)(+) dynamics. Plant J 69: 181-192.

196. Chaudhuri B, Hormann F, Frommer WB (2011) Dynamic imaging of glucose flux impedance using FRET sensors in wild-type Arabidopsis plants. J Exp Bot 62: 2411-2417.

197. Rincon-Zachary M, Teaster ND, Sparks JA, Valster AH, Motes CM, et al. (2010) Fluorescence resonance energy transfer-sensitized emission of yellow cameleon 3.60 reveals root zone-specific calcium signatures in Arabidopsis in response to aluminum and other trivalent cations. Plant Physiol 152: 1442-1458.

198. Yang H, Bogner M, Stierhof YD, Ludewig U (2010) H-independent glutamine transport in plant root tips. PLoS One 5: e8917.

199. Muller SM, Galliardt H, Schneider J, Barisas BG, Seidel T (2013) Quantification of Forster resonance energy transfer by monitoring sensitized emission in living plant cells. Front Plant Sci 4: 413.

200. Xia Z, Liu Y (2001) Reliable and global measurement of fluorescence resonance energy transfer using fluorescence microscopes. Biophys J 81: 2395-2402.

201. Plaxton WC, Tran HT (2011) Metabolic adaptations of phosphate-starved plants. Plant Physiol 156: 1006-1015.

202. Vance CP, Uhde-Stone C, Allan DL (2003) Phosphorus acquisition and use: critical adaptations by plants for securing a nonrenewable resource. New Phytol 157: 423-447.

203. Walker DA, Sivak MN (1986) Photosynthesis and phosphate: a cellular affair? Trends Biochem Sci 11: 176-179.

204. Gout E, Bligny R, Douce R, Boisson AM, Rivasseau C (2011) Early response of plant cell to carbon deprivation: in vivo 31P-NMR spectroscopy shows a quasi-instantaneous disruption on cytosolic sugars, phosphorylated intermediates of energy metabolism, phosphate partitioning, and intracellular pHs. New Phytol 189: 135-147.

205. Pratt J, Boisson AM, Gout E, Bligny R, Douce R, et al. (2009) Phosphate (Pi) starvation effect on the cytosolic Pi concentration and Pi exchanges across the tonoplast in plant cells: an in vivo 31P-nuclear magnetic resonance study using methylphosphonate as a Pi analog. Plant Physiol 151: 1646-1657.

206. Rebeille F, Bligny R, Douce R (1984) Is the cytosolic Pi concentration a limiting factor for plant cell respiration? Plant Physiol 74: 355-359.

207. Sharkey TD, Vanderveer PJ (1989) Stromal phosphate concentration is low during feedback limited photosynthesis. Plant Physiol 91: 679-684.

208. van Rheenen J, Langeslag M, Jalink K (2004) Correcting confocal acquisition to optimize imaging of fluorescence resonance energy transfer by sensitized emission. Biophysical Journal 86: 2517-2529.

209. Brown CM (2007) Fluorescence microscopy-avoiding the pitfalls. Journal of cell science 120: 1703-1705.

210. Day RN, Davidson MW (2012) Fluorescent proteins for FRET microscopy: monitoring protein interactions in living cells. Bioessays 34: 341-350.

211. Shaner NC, Steinbach PA, Tsien RY (2005) A guide to choosing fluorescent proteins. Nat Methods 2: 905-909.

212. Deuschle K, Okumoto S, Fehr M, Looger LL, Kozhukh L, et al. (2005) Construction and optimization of a family of genetically encoded metabolite sensors by semirational protein engineering. Protein Sci 14: 2304-2314.

213. Keinath NF, Waadt R, Brugman R, Schroeder JI, Grossmann G, et al. (2015) Live Cell Imaging with R-GECO1 Sheds Light on flg22- and Chitin-Induced Transient [Ca(2+)]cyt Patterns in Arabidopsis. Mol Plant 8: 1188-1200.

214. Chiou TJ, Lin SI (2011) Signaling network in sensing phosphate availability in plants. Annu Rev Plant Biol 62: 185-206.

215. Zhang Z, Liao H, Lucas WJ (2014) Molecular mechanisms underlying phosphate sensing, signaling, and adaptation in plants. J Integr Plant Biol 56: 192-220.

216. Feige JN, Sage D, Wahli W, Desvergne B, Gelman L (2005) PixFRET, an ImageJ plug-in for FRET calculation that can accommodate variations in spectral bleed-throughs. Microsc Res Tech 68: 51-58.

217. Roszik J, Lisboa D, Szollosi J, Vereb G (2009) Evaluation of intensity-based ratiometric FRET in image cytometry--approaches and a software solution. Cytometry A 75: 761-767.

218. Lam AJ, St-Pierre F, Gong Y, Marshall JD, Cranfill PJ, et al. (2012) Improving FRET dynamic range with bright green and red fluorescent proteins. Nat Methods 9: 1005-1012.

219. Miyawaki A (2003) Visualization of the spatial and temporal dynamics of intracellular signaling. Dev Cell 4: 295-305.

220. Lee DW, Lee S, Lee G-j, Lee KH, Kim S, et al. (2006) Functional characterization of sequence motifs in the transit peptide of Arabidopsis small subunit of rubisco. Plant Physiology 140: 466-483.

221. Clough SJ, Bent AF (1998) Floral dip: a simplified method forAgrobacterium-mediated transformation ofArabidopsis thaliana. The plant journal 16: 735-743.

222. Murashige T, Skoog F (1962) A revised medium for rapid growth and bioassays with tobacco tissue cultures. Physiol Plant 15: 473-497.

223. Littlejohn GR, Gouveia JD, Edner C, Smirnoff N, Love J (2010) Perfluorodecalin enhances in vivo confocal microscopy resolution of Arabidopsis thaliana mesophyll. New Phytologist 186: 1018-1025.

224. Cordell D (2010) The Story of Phosphorus: Sustainability implications of global phosphorus scarcity for food security.

225. Baker A, Ceasar SA, Palmer AJ, Paterson JB, Qi W, et al. (2015) Replace, reuse, recycle: improving the sustainable use of phosphorus by plants. Journal of experimental botany 66: 3523-3540.

226. Vance CP, Uhde-Stone C, Allan DL (2003) Phosphorus acquisition and use: critical adaptations by plants for securing a nonrenewable resource. New phytologist 157: 423-447.

227. Härtel H, Benning C (2000) Can digalactosyldiacylglycerol substitute for phosphatidylcholine upon phosphate deprivation in leaves and roots of Arabidopsis? Biochemical Society Transactions 28: 729-732.

228. Yu B, Xu C, Benning C (2002) Arabidopsis disrupted in SQD2 encoding sulfolipid synthase is impaired in phosphate-limited growth. Proceedings of the National Academy of Sciences 99: 5732-5737.

229. Muchhal US, Pardo JM, Raghothama K (1996) Phosphate transporters from the higher plant Arabidopsis thaliana. Proceedings of the National Academy of Sciences 93: 10519-10523.

230. Banerjee S, Garcia LR, Versaw WK (2016) Quantitative Imaging of FRET-Based Biosensors for Cell-and Organelle-Specific Analyses in Plants. Microscopy and microanalysis: the official journal of Microscopy Society of America, Microbeam Analysis Society, Microscopical Society of Canada 22: 300-310.

231. Verbelen J-P, Cnodder TD, Le J, Vissenberg K, Baluška F (2006) The root apex of Arabidopsis thaliana consists of four distinct zones of growth activities: meristematic zone, transition zone, fast elongation zone and growth terminating zone. Plant signaling & behavior 1: 296-304.

232. Bottomley W, Spencer D, Wheeler A, Whitfeld P (1971) The effect of a range of RNA polymerase inhibitors on RNA synthesis in higher plant chloroplasts and nuclei. Archives of biochemistry and biophysics 143: 269-275.

233. Lai F, Thacker J, Li Y, Doerner P (2007) Cell division activity determines the magnitude of phosphate starvation responses in Arabidopsis. The Plant Journal 50: 545-556.

234. Delmer DP, Amor Y (1995) Cellulose biosynthesis. The Plant Cell 7: 987.

235. Brady SM, Orlando DA, Lee J-Y, Wang JY, Koch J, et al. (2007) A high-resolution root spatiotemporal map reveals dominant expression patterns. Science 318: 801-806.

236. Karthikeyan AS, Varadarajan DK, Mukatira UT, D'Urzo MP, Damsz B, et al. (2002) Regulated expression of Arabidopsis phosphate transporters. Plant Physiology 130: 221-233.

237. Kanno S, Arrighi J-F, Chiarenza S, Bayle V, Berthomé R, et al. (2016) A novel role for the root cap in phosphate uptake and homeostasis. eLife 5: e14577.

238. Truernit E, Haseloff J (2008) A simple way to identify non-viable cells within living plant tissue using confocal microscopy. Plant methods 4: 1.

239. Ames BN (1966) [10] Assay of inorganic phosphate, total phosphate and phosphatases. Methods in enzymology 8: 115-118.

240. Miyaji T, Kuromori T, Takeuchi Y, Yamaji N, Yokosho K, et al. (2015) AtPHT4; 4 is a chloroplast-localized ascorbate transporter in Arabidopsis. Nature communications 6.

241. Rausch C, Zimmermann P, Amrhein N, Bucher M (2004) Expression analysis suggests novel roles for the plastidic phosphate transporter Pht2; 1 in auto-and heterotrophic tissues in potato and Arabidopsis. The Plant Journal 39: 13-28.

242. Schulz B, Frommer W, Flügge U, Hummel S, Fischer K, et al. (1993) Expression of the triose phosphate translocator gene from potato is light dependent and restricted to green tissues. Molecular and General Genetics MGG 238: 357-361.

243. Poirier Y, Thoma S, Somerville C, Schiefelbein J (1991) Mutant of Arabidopsis deficient in xylem loading of phosphate. Plant physiology 97: 1087-1093.

244. Hamburger D, Rezzonico E, Petétot JM-C, Somerville C, Poirier Y (2002) Identification and characterization of the Arabidopsis PHO1 gene involved in phosphate loading to the xylem. The Plant Cell 14: 889-902.

245. Rouached H, Stefanovic A, Secco D, Bulak Arpat A, Gout E, et al. (2011) Uncoupling phosphate deficiency from its major effects on growth and transcriptome via PHO1 expression in Arabidopsis. The Plant Journal 65: 557-570.